Optical Characterization of Natural and Anthropogenic Aerosols Using ChAMBRe Experiments & Field Campaigns

Department of Physics, University of Genoa
PhD course in Physics and Nanoscience, XXXVIII cycle

Candidate: **Muhammad Irfan**

Supervisors:
Prof. **Paolo Prati** (University of Genoa)
Prof. **Dario Massabò** (University of Genoa)

Table of Contents

CHAPTER 1: Introduction

Atmospheric aerosols occupy solid or liquid particles suspended in the atmosphere, initiating from a wide range of natural and anthropogenic sources. Natural sources include dust, sea salt particles, volcanic emissions, and biogenic particles, whereas anthropogenic emissions come primarily from fossil fuel burning, industrial events, biomass burning, and vehicular traffic (Seinfeld and Pandis, 2016; Pöschl, 2005). These particles correspond to a complex and active component of the Earth's atmosphere and play a elementary role in atmospheric physics, climate processes, and air quality. Aerosols exhibit substantial variability in size distribution, morphology, chemical composition, and optical properties, which collectively determine their atmospheric lifetime, transport behavior, and environmental impacts (Andreae and Rosenfeld, 2008).

From a radiative perspective, atmospheric aerosols significantly influence the Earth's energy balance through their interactions with both incoming solar radiation and outgoing terrestrial radiation. These interactions occur primarily through scattering and absorption processes, which together determine the overall radiative forcing of the climate system. Aerosols therefore play an important role in modulating the Earth's radiation budget and remain one of the largest sources of uncertainty in current climate projections (Haywood and Boucher, 2000). Aerosol particles capable of efficiently absorbing radiation, such as black carbon, can contribute to atmospheric warming by converting absorbed solar energy into heat. In contrast, predominantly scattering particles such as sulfate aerosols tend to exert a cooling effect by reflecting incoming solar radiation back to space and increasing the planetary albedo (Bond et al., 2013; Seinfeld and Pandis, 2016).

Among atmospheric aerosols, particulate matter (PM) is commonly classified according to its aerodynamic diameter, which governs particle transport dynamics, atmospheric residence time, deposition processes in the human respiratory system, and interaction with radiation. Fine particulate matter with an aerodynamic diameter smaller than 2.5 μm ($PM_{2.5}$) is of particular concern because of its ability to remain suspended in the atmosphere for extended periods and to penetrate deeply into the respiratory tract. Due to their small size and large surface area, $PM_{2.5}$ particles often contain complex mixtures of

inorganic species, organic compounds, and carbonaceous components that significantly influence both their optical behavior and toxicological effects (Dockery et al., 1993; Zhang et al., 2007; Putaud et al., 2010; Lelieveld et al., 2015).

Understanding the physical, chemical, and optical properties of atmospheric aerosols, especially fine particulate matter is therefore essential for improving climate models, assessing air quality, and evaluating human exposure risks. In this context, comprehensive experimental investigations combining real-time and offline optical and chemical analyses provide valuable insights into the sources, transformation processes, and radiative impacts of atmospheric particulate matter.

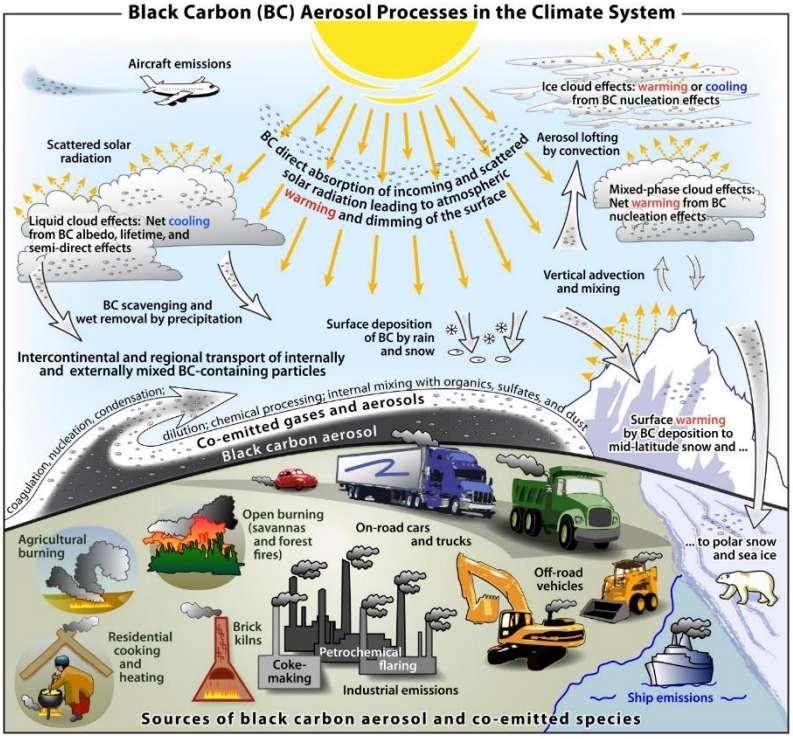

Figure 1.1: *Major processes affecting black carbon (BC) in the climate system, including emissions from combustion sources, atmospheric transport and mixing, interactions with clouds and radiation, and removal through wet and dry deposition. BC absorbs solar radiation, warms the atmosphere, influences cloud properties, and alters snow and ice albedo after deposition. Adapted from Bond et al. (2013).*

1.1: Particulate Matter Classification and Physical Definition

Atmospheric particulate matter (PM) is commonly classified according to particle size because particle diameter strongly influences atmospheric transport, optical behavior, deposition mechanisms, and human health impacts. Based on aerodynamic diameter, particulate matter is generally categorized into three major fractions: coarse particles ($PM_{10-2.5}$), fine particles ($PM_{2.5}$), and ultrafine particles ($PM_{0.1}$). These size classes correspond to particles with aerodynamic diameters between 2.5 and 10 μm, smaller than 2.5 μm, and smaller than 0.1 μm, respectively. Particle size plays a critical role in determining atmospheric residence time, long-range transport potential, and interactions with radiation and cloud microphysics (Zhang et al., 2015; Buseck and Adachi, 2018).

Atmospheric aerosol populations typically exhibit a multimodal size distribution, commonly divided into nucleation, accumulation, and coarse modes, each associated with distinct formation mechanisms and atmospheric processes. Ultrafine particles in the nucleation mode are formed primarily through gas-to-particle conversion processes such as homogeneous nucleation of low-volatile vapors. Particles in the accumulation mode arise from condensational growth and coagulation processes, while coarse particles are generated mainly through mechanical processes such as soil resuspension, sea spray production, and particle fragmentation (Kulmala et al., 2016; Bianchi et al., 2019**), as illustrated in Figure 1.2.**

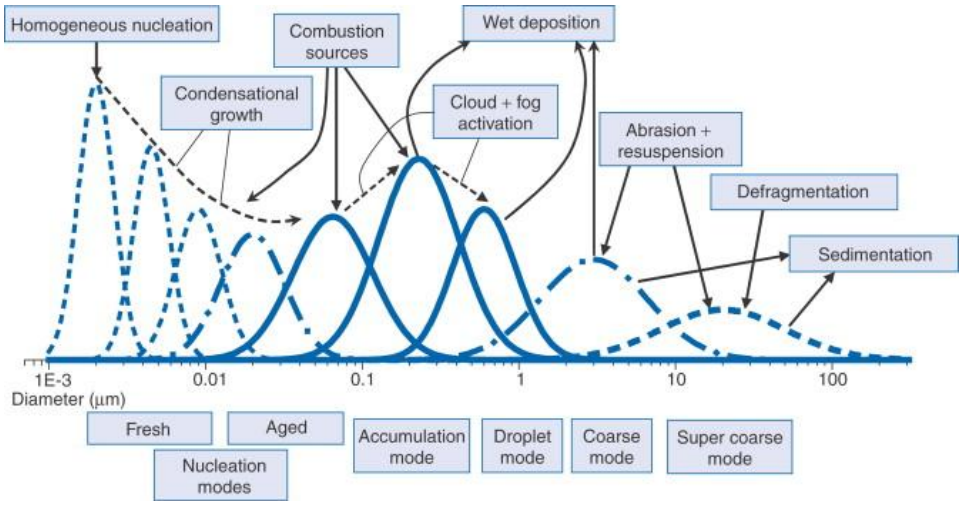

Figure 1.2: *Atmospheric aerosol size distribution and associated formation and removal processes. Adapted from Kulmala et al. (2016).*

The concept of aerodynamic diameter is fundamental for describing the motion and deposition of aerosol particles in the atmosphere. The aerodynamic diameter $d_a$is defined as the diameter of a unit-density spherical particle that has the same terminal settling velocity as the particle of interest. This parameter accounts for variations in particle density and shape, allowing comparison between particles with different physical characteristics. The aerodynamic diameter can be expressed as

$$d_a = d_p\sqrt{\frac{\rho_p \chi}{\rho_0}} \qquad (1.1)$$

where d_p is the physical particle diameter, $\rho_p$is the particle density, X is the dynamic shape factor describing deviations from spherical geometry, and $\rho_0 = 1\ \mathrm{g\ cm^{-3}}$ is the reference unit density.

This formulation is particularly relevant for atmospheric aerosols because many particles exhibit irregular morphologies and complex internal structures. For example, soot particles emitted from combustion sources typically form fractal aggregates composed of nanoscale carbon spherules, while aged atmospheric particles often consist of internally mixed components including inorganic salts, organic compounds, and carbonaceous

material. These structural characteristics strongly influence particle mobility, optical properties, and atmospheric processing (Adachi et al., 2020; Buseck and Adachi, 2018).

The motion of aerosol particles in the atmosphere is also governed by gravitational settling. In the Stokes regime, which applies to small particles at low Reynolds numbers, the terminal settling velocity $v_s$can be expressed as

$$v_s = \frac{\rho_p d_p^2 g C_c}{18\mu} \qquad (1.2)$$

where g is the gravitational acceleration, μ is the dynamic viscosity of air, and C_c is the Cunningham slip correction factor that accounts for non-continuum effects occurring when particle sizes approach the mean free path of air molecules.

Because of their small diameter, fine particles ($PM_{2.5}$) exhibit extremely low gravitational settling velocities and can remain suspended in the atmosphere for extended periods. Their atmospheric residence times typically range from several days to weeks, enabling long-range transport over regional and intercontinental scales (Bianchi et al., 2019; Zhang et al., 2015). During transport, particles undergo chemical aging processes such as heterogeneous reactions, condensation of secondary species, and coagulation, which modify their physical and chemical properties.

The sources and formation mechanisms of particulate matter vary significantly across different size fractions. Coarse particles ($PM_{10–2.5}$) are primarily generated through mechanical processes such as soil resuspension, wind-blown dust emissions, sea spray production, and abrasion from road surfaces or construction activities. In contrast, fine particles ($PM_{2.5}$) are largely produced by combustion processes and secondary atmospheric formation. Major anthropogenic sources include fossil fuel combustion, biomass burning, residential heating, and industrial emissions. Secondary $PM_{2.5}$ forms through atmospheric chemical reactions involving gaseous precursors such as sulfur dioxide (SO_2), nitrogen oxides (NO_x), ammonia (NH_3), and volatile organic compounds (VOCs), producing sulfate, nitrate, ammonium, and secondary organic aerosols (Shrivastava et al., 2017; Bianchi et al., 2019).

1.2: Chemical Composition of Atmospheric Aerosols

Atmospheric aerosol particles consist of complex mixtures of inorganic compounds, organic matter, carbonaceous species, trace metals, and biological material. Their chemical composition varies considerably depending on emission sources, atmospheric processing, geographical location, and meteorological conditions. Understanding aerosol chemical composition is essential for assessing particle toxicity, atmospheric reactivity, radiative properties, and their influence on climate and air quality (Seinfeld and Pandis, 2016; Pöschl, 2005).

The major components of atmospheric particulate matter include inorganic ions, organic aerosols, carbonaceous particles, mineral dust, sea salt, and trace metals. The relative abundance of these components differs significantly between urban, rural, marine, and desert environments, reflecting variations in both natural and anthropogenic emission sources. In addition, secondary formation processes modify aerosol composition through gas-to-particle conversion and heterogeneous chemical reactions in the atmosphere (Jimenez et al., 2009).

1.2.1: Inorganic Components

Inorganic species represent a significant fraction of atmospheric particulate matter, particularly within the fine particle range ($PM_{2.5}$). The dominant inorganic constituents typically include sulfate (SO_4^{2-}), nitrate (NO_3^-), and ammonium (NH_4^+), which are formed through secondary atmospheric reactions involving gaseous precursors such as sulfur dioxide (SO_2), nitrogen oxides (NO_x), and ammonia (NH_3). These reactions lead to the formation of secondary inorganic aerosols through oxidation processes occurring in both the gas phase and aqueous cloud droplets (Seinfeld and Pandis, 2016).

Sulfate aerosols are mainly produced through oxidation of sulfur dioxide emitted from fossil fuel combustion, volcanic activity, and marine dimethyl sulfide emissions. Nitrate aerosols originate primarily from oxidation of nitrogen oxides associated with traffic emissions and industrial combustion sources. Ammonium ions largely arise from agricultural activities such as livestock farming and fertilizer application, and they play

an important role in neutralizing acidic sulfate and nitrate particles in the atmosphere (Pöschl, 2005; Harrison, 2018).

In addition to secondary inorganic aerosols, mineral dust and sea salt contribute significantly to aerosol mass in many environments. Mineral dust particles originate from wind-driven resuspension of soil and desert surfaces and are composed mainly of silicates, oxides, and carbonates of elements such as aluminum, silicon, calcium, and iron. Sea salt aerosols, generated through bubble bursting and wave action at the ocean surface, consist primarily of sodium chloride along with other marine ions including magnesium, sulfate, and potassium (Seinfeld and Pandis, 2016).

1.2.2: Organic Aerosols

Organic aerosols (OA) constitute a large fraction of atmospheric particulate matter, particularly within the fine particle size range. They consist of thousands of organic compounds with varying volatility, polarity, and chemical functionality. Organic aerosols are generally classified into primary organic aerosols (POA) and secondary organic aerosols (SOA) depending on their formation mechanisms (Jimenez et al., 2009).

Primary organic aerosols are emitted directly from sources such as fossil fuel combustion, biomass burning, residential heating, and cooking activities. In contrast, secondary organic aerosols are produced through atmospheric oxidation of volatile organic compounds (VOCs) emitted from both anthropogenic and biogenic sources. These oxidation processes produce low-volatile compounds that condense onto existing particles or nucleate to form new particles (Hallquist et al., 2009).

Secondary organic aerosol formation involves complex chemical mechanisms driven by reactions with atmospheric oxidants such as hydroxyl radicals (OH), ozone (O_3), and nitrate radicals (NO_3). These reactions lead to the formation of highly oxygenated organic molecules that significantly influence particle hygroscopicity, cloud condensation nuclei activity, and atmospheric aging processes (Jimenez et al., 2009).

1.3: Carbonaceous Aerosols

Carbonaceous aerosols represent a major component of atmospheric particulate matter and are typically divided into organic carbon (OC) and elemental carbon (EC), often referred to as black carbon (BC). These components originate primarily from incomplete combustion processes including fossil fuel burning, biomass combustion, and residential heating (Bond et al., 2013).

Black carbon particles exhibit strong light-absorbing properties and play an important role in atmospheric radiative forcing. Their ability to absorb solar radiation contributes to atmospheric warming, while deposition of BC on snow and ice surfaces reduces surface albedo and accelerates melting processes (Bond et al., 2013).

Organic carbon encompasses a wide range of compounds with diverse chemical and optical properties. A fraction of organic aerosols, commonly referred to as brown carbon (BrC), exhibits wavelength-dependent light absorption in the ultraviolet and visible spectral regions. These optical characteristics can significantly influence aerosol radiative effects and atmospheric energy balance (Laskin et al., 2015). Because of their strong influence on aerosol optical behavior and climate interactions, carbonaceous aerosols have become a major focus of atmospheric research.

1.3.1: Carbonaceous Aerosols in $PM_{2.5}$

Carbonaceous aerosols constitute a substantial fraction of $PM_{2.5}$ mass in both urban and rural environments, often contributing between 20% and 60% of total fine particulate matter (Putaud et al., 2004; Andreae and Gelencsér, 2006). These aerosols originate primarily from incomplete combustion processes and from secondary organic aerosol formation through atmospheric oxidation.

Elemental carbon, often referred to as black carbon in an optical context, consists of refractory graphitic structures formed during high-temperature combustion and represents the dominant light-absorbing component of atmospheric particulate matter (Bond and Bergstrom, 2006; Petzold et al., 2013).

Freshly emitted BC particles typically exhibit fractal aggregate morphologies. Their mass follows a fractal scaling relationship (Sorensen, 2001):

$$M \propto R_g^{D_f} \qquad (1.3)$$

where R_g is the radius of gyration and D_f is the fractal dimension, typically ranging between 1.7 and 1.9. Atmospheric aging processes lead to internal mixing of BC with inorganic salts and organic compounds, altering particle morphology, hygroscopicity, and optical properties (Adachi et al., 2010; Liu et al., 2017).

A fraction of organic carbon, commonly referred to as brown carbon (BrC), absorbs strongly in the ultraviolet and short visible wavelengths and can contribute significantly to atmospheric light absorption, particularly in biomass-burning influenced environments (Kirchstetter et al., 2004; Laskin et al., 2015).

1.4: Optical Properties of Atmospheric Aerosols

The interaction of atmospheric aerosols with electromagnetic radiation plays a fundamental role in determining their climatic impact. Aerosols influence the Earth's radiative balance through scattering and absorption of solar and terrestrial radiation, processes that collectively define aerosol optical properties (IPCC, 2021).

The attenuation of radiation passing through an aerosol layer is described by the extinction coefficient:

$$\sigma_{ext} = \sigma_{sca} + \sigma_{abs} \qquad (1.4)$$

where $\sigma_{sca}$and σ_{abs}represent the scattering and absorption coefficients, respectively (Bohren and Huffman, 1983).

The relative contribution of scattering and absorption processes is described by the single scattering albedo (SSA):

$$SSA = \frac{\sigma_{sca}}{\sigma_{sca}+\sigma_{abs}} \qquad (1.5)$$

Aerosols with high SSA values mainly scatter radiation and tend to produce a cooling effect, whereas strongly absorbing aerosols such as black carbon exhibit lower SSA values and contribute to atmospheric warming (Bond et al., 2013).

The spectral dependence of aerosol absorption is commonly described by the absorption Ångström exponent (AAE):

$$\sigma_{abs}(\lambda) \propto \lambda^{-AAE} \qquad (1.6)$$

Black carbon typically exhibits AAE values close to unity, while brown carbon shows stronger wavelength dependence with larger AAE values (Moosmüller et al., 2011; Laskin et al., 2015).

Aerosol optical properties are also affected by atmospheric aging processes. Condensation of secondary species and internal mixing can enhance absorption through the lensing effect, where non-absorbing coatings surrounding absorbing cores increase the effective absorption of radiation (Bond et al., 2013).

Accurate measurement of aerosol optical properties is therefore essential for improving climate models and understanding aerosol–radiation interactions. These properties are commonly measured using instruments such as integrating nephelometers for scattering, aethalometers for absorption, photoacoustic spectrometers, and multi-wavelength absorption analyzers.

1.5: Health Effects of $PM_{2.5}$

Beyond their climatic implications, atmospheric aerosols also pose significant risks to human health and environmental quality. Exposure to particulate matter has been strongly associated with increased incidence of respiratory and cardiovascular diseases, reduced lung function, and premature mortality. Large epidemiological studies have demonstrated that long-term exposure to elevated aerosol concentrations, particularly in densely populated urban environments, contributes substantially to the global burden of disease (Dockery et al., 1993; Lelieveld et al., 2015; Cohen et al., 2017). Consequently, particulate matter has become a central focus of air-quality monitoring and environmental regulation worldwide.

Fine particulate matter ($PM_{2.5}$) is widely recognized as one of the most harmful air pollutants because of its ability to penetrate deeply into the human respiratory system. Particle depositions within the respiratory tract occur through several mechanisms including diffusion, sedimentation, and interception. The particle diffusion coefficient can be expressed as

$$D_p = \frac{k_B T C_c}{3\pi\mu d_p} \qquad (1.7)$$

where k_B is the Boltzmann constant, T is temperature, C_c is the Cunningham slip correction factor, μ is the dynamic viscosity of air, and d_p is the particle diameter. Due to enhanced diffusional deposition, fine and ultrafine particles can efficiently reach the alveolar region of the lungs, where gas exchange occurs, and may subsequently translocate into the bloodstream (Oberdörster et al., 2005; Nel et al., 2006).

Numerous epidemiological studies have linked both short-term and long-term exposure to $PM_{2.5}$ with increased mortality from cardiovascular and respiratory diseases, reduced lung development, and premature death (Burnett et al., 2014; Cohen et al., 2017). In addition to particle size effects, the chemical composition of aerosols also plays a critical role in determining toxicity. Carbonaceous particles and associated compounds, including polycyclic aromatic hydrocarbons and transition metals, can generate reactive oxygen species that induce oxidative stress, inflammation, and cellular damage in lung tissues (Kelly and Fussell, 2012; Schraufnagel et al., 2019).

Due to their small size, large surface-to-volume ratio, and complex chemical composition, fine particles represent one of the most climatically and toxicologically relevant fractions of atmospheric particulate matter. $PM_{2.5}$ strongly influences atmospheric radiative transfer through scattering and absorption of solar radiation and contributes to aerosol–cloud interactions. Moreover, their ability to penetrate deeply into the human respiratory system and reach the alveolar region makes them particularly harmful to human health, contributing to respiratory and cardiovascular diseases (Schraufnagel et al., 2019; Burnett et al., 2014). The deposition efficiency of inhaled particles strongly depends on particle size, with fine and ultrafine particles capable of penetrating deep into the alveolar region

of the lungs, where gas exchange occurs and systemic translocation may occur, as illustrated in Figure 1.3.

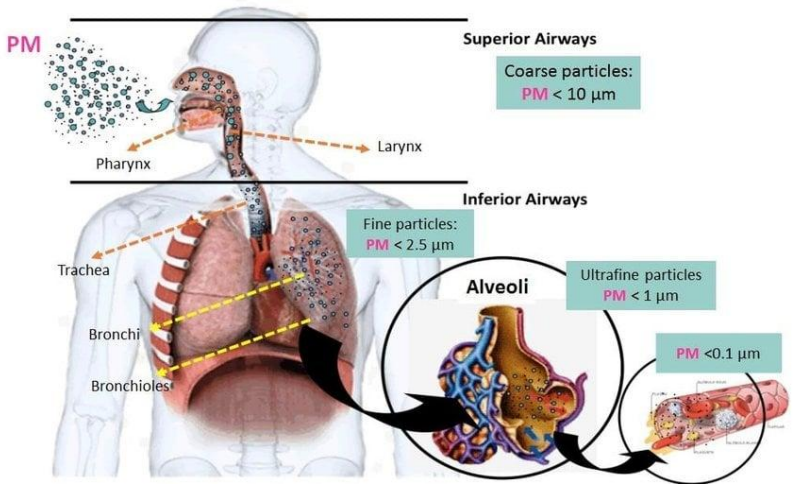

***Figure 1.3**: Size-dependent deposition of particulate matter in the human respiratory system. Adapted from Oberdörster et al. (2005).*

1.6: Measurement Techniques

Accurate characterization of atmospheric aerosols requires the integration of multiple experimental techniques capable of measuring both their optical properties and chemical composition. These complementary approaches provide essential information for understanding aerosol sources, atmospheric transformation processes, and their radiative impacts. In general, aerosol characterization combines real-time in-situ optical measurements with offline laboratory analyses performed on particles collected on filter substrates (Moosmüller et al., 2011; Petzold et al., 2013).

Real-time instruments allow continuous monitoring of aerosol optical properties with high temporal resolution, enabling investigation of short-term variations in atmospheric aerosol concentrations and optical behavior. One widely used instrument for measuring aerosol light absorption is the AE33 Aethalometer, which determines black carbon concentrations by measuring the attenuation of light transmitted through aerosol particles collected on a filter tape. The AE33 operates at multiple wavelengths from the ultraviolet to the near-infrared spectral range, enabling the determination of spectral absorption

properties and the estimation of contributions from different emission sources. The instrument employs a dual-spot measurement technique that compensates for filter loading effects, improving the accuracy and stability of absorption measurements (Drinovec et al., 2015).

Aerosol scattering properties are commonly measured using integrating nephelometers such as the Aurora 4000 Nephelometer, which determines the aerosol scattering coefficient by measuring the intensity of light scattered by particles over a defined angular range. Measurements at multiple wavelengths allow determination of the spectral dependence of scattering and provide useful information about aerosol size distribution and composition (Anderson and Ogren, 1998). Direct measurements of aerosol absorption can also be performed using photoacoustic spectroscopy, implemented in instruments such as the Photoacoustic Extinctiometers (PAXs). In this method, modulated laser radiation absorbed by aerosol particles produces periodic heating and pressure fluctuations that generate acoustic waves detected by sensitive microphones. The amplitude of the acoustic signal is proportional to the aerosol absorption coefficient, allowing accurate measurements of light absorption without interference from scattering processes (Arnott et al., 1999; Moosmüller et al., 2009).

In addition to real-time optical instruments, offline filter-based techniques are widely used to investigate aerosol optical properties with high spectral resolution. These techniques analyze particles collected on filters during sampling campaigns and allow detailed laboratory characterization of aerosol absorption properties. The Multi-Wavelength Absorption Analyzer (MWAA) measures aerosol light absorption at several discrete wavelengths using particles deposited on filter substrates. This method enables the determination of spectral absorption coefficients and the separation of contributions from black carbon and brown carbon components (Massabò et al., 2013). More recently, the Broadband Light Analyzer of Complex Aerosol (BLAnCA) has been introduced as an automated laboratory instrument for high-resolution spectral measurements of aerosol light absorption on filter samples. BLAnCA employs a broadband light source and a spectrometer to measure absorption across a continuous spectral range, typically from

approximately 375 to 1000 nm, enabling detailed investigation of the wavelength dependence of aerosol absorption and improved characterization of complex carbonaceous aerosol mixtures (Isolabella et al., 2025).

Complementary to optical measurements, chemical characterization of aerosol particles is commonly performed using analytical techniques applied to filter samples. The Sunset OC/EC Analyzer is widely used to determine organic carbon (OC) and elemental carbon (EC) concentrations in particulate matter. In this method, aerosol particles collected on quartz filters are subjected to controlled heating under different atmospheres in order to thermally separate organic and elemental carbon fractions. The evolved carbon species are oxidized to carbon dioxide and quantified using non-dispersive infrared detection (Birch and Cary, 1996; Cavalli et al., 2010). Continuous or semi-continuous measurements of carbonaceous aerosols can also be performed using instruments such as the TCA08 (Thermal Carbon Analyzer), which distinguishes carbon fractions based on their thermal stability and oxidation behavior.

The elemental composition of aerosol particles can be determined using Energy-Dispersive X-Ray Fluorescence (ED-XRF), a non-destructive analytical technique that identifies and quantifies elemental constituents by measuring characteristic X-ray emissions produced when atoms are excited by an incident X-ray beam. This method allows detection of a wide range of elements, including crustal components and trace metals, and is widely used in aerosol source apportionment studies and investigations of mineral dust contributions to particulate matter (Querol et al., 2007; Viana et al., 2008).

The integration of optical measurements with chemical and elemental analyses provides a comprehensive framework for investigating aerosol properties and their environmental impacts. Real-time instruments capture the temporal variability of aerosol optical behavior, while filter-based laboratory analyses provide detailed information on aerosol composition and emission sources. Combining these complementary approaches improves the interpretation of aerosol–radiation interactions and contributes to reducing uncertainties in climate modeling and air-quality assessments (Petzold et al., 2013).

Table 1.1: *Summary of Aerosol Optical and Chemical Measurement Techniques Used for Aerosol Characterization*

Instrument/ Technique	Measurement Type	Parameter Measured	Measurement Principle	Key Reference
AE33 Aethalometer	Real-time optical	Black carbon concentration, spectral absorption	Light attenuation through particles deposited on filter tape; dual-spot correction for filter loading	Drinovec et al., 2015
Aurora 4000 Nephelometer	Real-time optical	Aerosol scattering coefficient (σsca)	Measures light scattered by aerosol particles over a defined angular range	Anderson and Ogren, 1998
PAXs (Photoacoustic extinctiometers)	Real-time optical	Aerosol absorption coefficient (σabs)	Photoacoustic detection of pressure waves generated by absorbed modulated laser radiation	Arnott et al., 1999
MWAA (Multi-Wavelength Absorption Analyzer)	Offline optical	Multi-wavelength aerosol absorption	Optical analysis of particles deposited on filters at multiple wavelengths	Massabò et al., 2013
BLAnCA (Broadband Light Analyzer of Complex Aerosol)	Offline optical	Broadband spectral absorption (≈375–1000 nm)	Spectral absorption measurement using broadband light source and spectrometer on filter samples	Isolabella et al., 2025
Sunset OC/EC Analyzer	Chemical analysis	Organic carbon (OC) and elemental carbon (EC)	Thermal–optical analysis of carbon fractions collected on quartz filters	Cavalli et al., 2010
TCA08 Thermal Carbon Analyzer	Chemical analysis	Carbonaceous aerosol fractions	Thermal evolution and oxidation of carbon species	Petzold et al., 2013

ED-XRF (Energy-Dispersive X-Ray Fluorescence)	Elemental analysis	Elemental composition (metals, crustal elements)	Detection of characteristic X-ray emission induced by incident X-ray beam	Querol et al., 2007

Table 1.2: *Typical Optical Parameters of $PM_{2.5}$ and Their Physical Meaning*

Parameter	**Symbol**	**Typical Range / Value**	**Main Influencing Factors**	**Key References**
Scattering coefficient	σsca	50–500 Mm^{-1}	Particle size distribution, sulfate and nitrate content, relative humidity	Anderson & Ogren (1998); Zieger et al. (2013)
Absorption coefficient	σabs	5–100 Mm^{-1}	Black carbon concentration, mixing state, particle coating	Bond & Bergstrom (2006); Moosmüller et al. (2011)
Extinction coefficient	σext	60–600 Mm^{-1}	Combined effects of scattering and absorbing aerosol components	Horvath (1993); Bohren & Huffman (1983)
Single scattering albedo	SSA	0.85–0.98	Relative abundance of absorbing carbonaceous particles	Bond et al. (2013)
Absorption Ångström exponent	AAE	≈1 (BC); 2–6 (BrC)	Aerosol composition, biomass burning influence	Kirchstetter et al. (2004); Laskin et al. (2015)
Mass absorption coefficient	MAC	7–12 $m^2 g^{-1}$ (at 880 nm)	BC morphology, internal mixing, particle coatings	Bond & Bergstrom (2006); Zanatta et al. (2016)

1.7: Objectives and Scope of the Thesis

The primary objective of this thesis is to investigate the optical properties of carbonaceous aerosols in fine particulate matter ($PM_{2.5}$) and to improve the understanding of their contribution to atmospheric light absorption and radiative effects. Carbonaceous particles, including black carbon (BC), organic carbon (OC), and brown carbon (BrC),

play a major role in determining aerosol optical behavior and represent an important component of atmospheric particulate matter.

This research focuses on the characterization of aerosol optical properties and their relationship with aerosol chemical composition, particle size distribution, and atmospheric processing. Particular attention is given to the wavelength-dependent absorption properties of carbonaceous aerosols and to the processes that modify their optical characteristics during atmospheric aging.

To achieve these objectives, the study combines real-time optical measurements with offline laboratory analyses of aerosol samples collected on filter substrates. Aerosol light absorption is measured using a multi-wavelength AE33 Aethalometer, while aerosol scattering properties are determined using an integrating nephelometer. Additional spectral information on aerosol absorption is obtained through filter-based optical techniques, including the Multi-Wavelength Absorption Analyzer (MWAA) and the Broadband Light Analyzer of Complex Aerosol (BLAnCA), which enable detailed investigation of the wavelength dependence of aerosol absorption and the contributions of different carbonaceous components.

Chemical characterization of aerosol samples is performed using thermal–optical analysis with a Sunset OC/EC analyzer, allowing quantification of organic carbon and elemental carbon fractions. In addition, the elemental composition of particulate matter is determined using Energy-Dispersive X-Ray Fluorescence (ED-XRF), providing information on crustal elements and trace metals that can be used to investigate aerosol sources and atmospheric processes.

The experimental work of this thesis includes both controlled chamber experiments and field measurements. Chamber experiments are conducted in the Chamber for Aerosol Modelling and Bio-aerosol Research (ChAMBRe) to investigate aerosol optical properties and aging processes under well-defined conditions. These experiments allow controlled generation and transformation of aerosols, providing insight into the evolution of aerosol optical properties and mixing states.

In addition to laboratory studies, field campaigns are conducted to investigate aerosol optical and chemical properties under real atmospheric conditions. These measurements provide information on the variability of atmospheric aerosols, their chemical composition, and their optical behavior in ambient environments. The combination of controlled chamber experiments and field observations allows comparison between laboratory-generated aerosols and ambient atmospheric particles.

The main objectives of this thesis can be summarized as follows:

- To characterize the spectral absorption properties of atmospheric aerosols using real-time and filter-based optical techniques.
- To quantify the contributions of black carbon and brown carbon to aerosol light absorption.
- To investigate the relationship between aerosol chemical composition and optical properties through combined optical and chemical analyses.
- To study the evolution of aerosol optical properties under controlled conditions using the ChAMBRe atmospheric simulation chamber.
- To analyze the optical and chemical properties of aerosols collected during field campaigns and compare them with chamber-generated aerosols.
- To evaluate the performance and comparability of different aerosol optical measurement techniques, including AE33, MWAA, and BLAnCA.

The remainder of this thesis is organized as follows. **Chapter 2** describes the experimental setup and instrumentation. **Chapter 3** presents measurement methodologies used for aerosol optical and chemical characterization. **Chapter 4** discusses the results obtained from field campaigns and the results of chamber experiments performed in ChAMBRe. Finally, **Chapter 5** summarizes the main findings of this work and outlines future research perspectives.

CHAPTER 2: Experimental Setup and Instrumentation

This chapter presents the experimental infrastructure and instrumentation employed in this study for the comprehensive characterization of $PM_{2.5}$ optical and physico-chemical properties. The measurement strategy integrates controlled laboratory experiments conducted in the Atmospheric Simulation Chamber with field deployments at two distinct environments, enabling both process-level investigation and real-world validation. A combination of real-time optical instruments and filter-based analytical techniques was utilized to quantify aerosol absorption, scattering, and mass concentrations, as well as their chemical composition. Particular emphasis is placed on the configuration, operating principles, and measurement capabilities of each instrument, including absorption photometers, integrating nephelometers, and advanced broadband optical analyzers. The detailed description of the experimental setup provided in this chapter establishes the technical foundation necessary for understanding the methodologies, data processing approaches, and subsequent interpretation of results presented in the following chapters.

The instrumentation and experimental configurations described in this chapter form the basis for the methodologies presented in Chapter 3. While this chapter focuses on the setup and operating principles of the instruments, the following chapter details the sampling procedures, data processing, and analytical approaches used in this study.

2.1: ChAMBRe: Chamber for Aerosol Modeling and Bioaerosol Research

The Chamber for Aerosol Modeling and Bioaerosol Research (ChAMBRe) is an experimental facility designed for controlled studies of atmospheric aerosols and bioaerosols under well-defined environmental conditions. The facility is installed at the Genoa division of the Italian National Institute for Nuclear Physics (INFN) and is operated in collaboration with the Environmental Physics Laboratory of the Department of Physics at the University of Genoa. ChAMBRe is part of the European research infrastructure ACTRIS (Aerosol, Clouds and Trace Gases Research Infrastructure), which provides advanced experimental platforms for atmospheric research across Europe (ACTRIS, 2023). The chamber has been previously described in detail in several studies

investigating aerosol optical properties and atmospheric processes (Massabò et al., 2018; Danelli et al., 2021).

The chamber consists of a cylindrical stainless-steel reactor with an internal volume of approximately 2.2 m^3. Structurally, the reactor is composed of two domed cylindrical sections connected by a central ring. Multiple ISO-K flanges of different diameters are distributed across the chamber body to allow connection of sampling lines, analytical instruments, and aerosol generation systems. All ports can be sealed to ensure vacuum tightness. Between experiments, the chamber is evacuated using vacuum pumps until pressures on the order of 10^{-3}mbar is reached. This evacuation procedure removes residual gases and particles from previous experiments and prepares the system for the introduction of clean air.

After evacuation, particle-free air is introduced into the chamber through a purification line consisting of activated carbon filters, HEPA filters, and silica dryers. This filtration system removes gaseous contaminants, particulate matter, and moisture, ensuring that experiments start from well-controlled initial conditions. Environmental parameters inside the chamber, including temperature, relative humidity, and pressure, are continuously monitored through integrated sensors connected to the control system.

ChAMBRe is designed to allow controlled introduction of a wide range of atmospheric pollutants. Gaseous species such as carbon dioxide (CO_2), nitric oxide (NO), nitrogen dioxide (NO_2), nitrogen oxides (NOx), and ozone (O_3) can be injected directly into the chamber. Ozone can also be generated photochemically using ultraviolet irradiation. Aerosol particles can be introduced through several generation techniques, including combustion sources for soot production, nebulization of aqueous solutions for secondary aerosol formation, or dispersion of mineral dust. Additionally, biological particles such as bacteria or pollen can be injected through nebulization or aerosolization systems, enabling bioaerosol studies. The chamber atmosphere is homogenized using a mixing fan located at the bottom of the reactor, which ensures spatially uniform aerosol and gas concentrations during experiments.

The facility also enables the investigation of atmospheric aging processes. Multiple pollutants can be introduced simultaneously to simulate realistic atmospheric mixtures, and photochemical reactions can be triggered using a high-intensity lamp installed above the chamber that mimics solar radiation. This configuration allows investigation of chemical transformation processes such as oxidation, secondary aerosol formation, and aging of combustion-generated particles under controlled laboratory conditions.

A wide range of analytical instruments are connected to ChAMBRe to monitor both gas-phase and particulate properties in real time. Environmental parameters such as pressure, humidity, and temperature are continuously recorded. Gas concentrations are measured using gas analyzers (ENVEA, France) capable of detecting CO_2, NO, NO_2, NOx, and O_3. Aerosol size distributions are determined using a Scanning Mobility Particle Sizer (SMPS, model 3938, TSI Inc., USA) and an Optical Particle Sizer (OPS, model 3330, TSI Inc., USA), which together provide particle size measurements spanning the nanometer to micrometer range. Optical properties of aerosols are monitored using three photoacoustic extinctiometers (PAX, Droplet Measurement Technologies, USA), which measure aerosol absorption and scattering coefficients at wavelengths of 405 nm, 532 nm, and 870 nm. Bioaerosol characterization is performed using a Wideband Integrated Bioaerosol Sensor (WIBS-NEO, Droplet Measurement Technologies, USA), which allows simultaneous particle sizing and fluorescence-based detection of biological particles.

Most instruments connected to ChAMBRe perform online measurements by continuously extracting a controlled air flow from the chamber and analyzing the suspended aerosol in real time. In addition to these online measurements, particulate matter samples can be collected on filters for offline analysis by connecting aerosol samplers to dedicated flanged ports. This combination of real-time monitoring and filter-based sampling allows comprehensive characterization of aerosol physical, chemical, and optical properties.

The entire experimental system is controlled through a supervisory control and data acquisition (SCADA) platform developed using National Instruments LabVIEW. Sensors

and instruments communicate through an Ethernet network and are managed by a NI Compact-RIO data acquisition unit (NI cRIO-9064 controller). This system enables synchronized monitoring of environmental parameters, automated data logging, and remote control of experimental conditions, ensuring reliable operation and reproducibility of experiments.

Overall, ChAMBRe provides a versatile experimental platform for investigating atmospheric aerosol processes, including particle generation, chemical aging, optical property evolution, and interactions between biological and non-biological aerosols under controlled laboratory conditions.

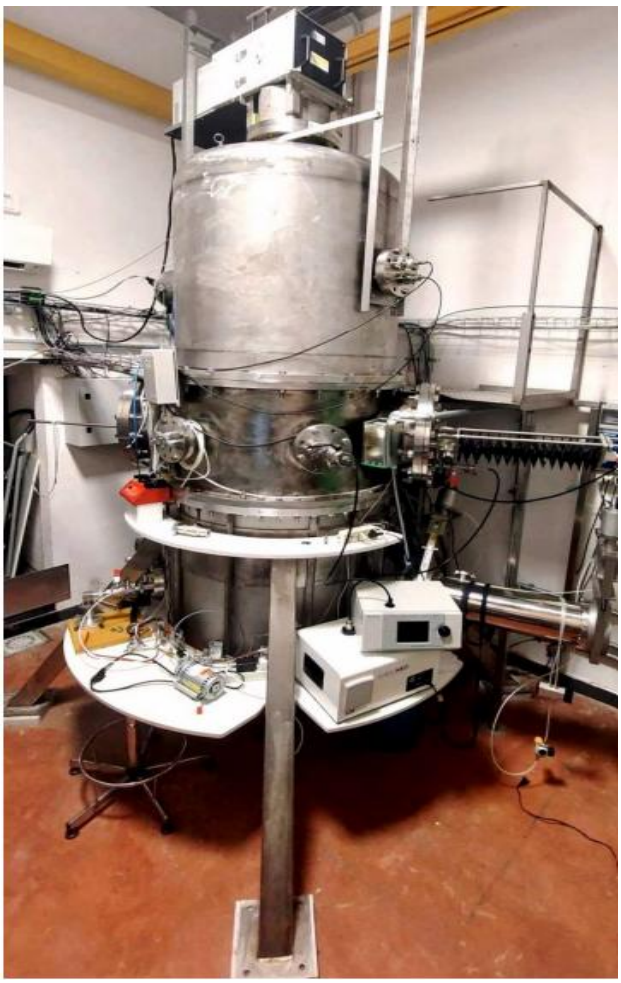

Figure 2.1: *ChAMBRe, the atmospheric simulation chamber.*

2.2: Dekati® eDiluter™ Pro Dilution System

The Dekati® eDiluter™ Pro is a two-stage ejector-based aerosol dilution and conditioning system designed to enable particle measurements under high concentration, high temperature, and high humidity conditions. The instrument is specifically developed for applications where direct sampling would overload optical or microphysical instruments or where thermodynamic stabilization of the aerosol is required prior to measurement. The system consists of two sequential ejector diluters with sheath air and an integrated temperature control unit that allows heating of the air dilution in the first stage up to 400 °C. This configuration enables controlled dilution of combustion aerosols and minimizes artefacts associated with condensation and rapid cooling.

The dilution process is based on entrainment of the aerosol sample by pressurized, particle-free dilution air. When dilution air is supplied (minimum 5 bar absolute), the ejectors generate a pressure drop that draws the aerosol sample into the mixing chamber. The sample is diluted in two consecutive stages, and the dilution factor of each stage is adjustable. The first-stage dilution factor can be selected as 5, 10, or 15, while the second-stage dilution factor is adjustable between 5 and 15, resulting in a total dilution factor ranging from 25 to 225. The overall dilution factor is expressed as

$$DF_{tot} = DF_1 \times DF_2 \qquad (2.1)$$

and the diluted aerosol concentration delivered to downstream instruments is therefore

$$C_{meas} = \frac{C_{raw}}{DF_{tot}} \qquad (2.2)$$

where C_{raw} represents the undiluted aerosol concentration and C_{meas} is the concentration at the measurement inlet.

The nominal sample inlet flow rate is approximately 4–10 LPM, depending on calibration parameters, while the diluted sample outlet flow is approximately 60 LPM. The outlet section includes a flow divider with three ports for connection to measurement

instruments. For correct ejector operation, at least one outlet port must remain open to ambient pressure, and the outlet of the first dilution stage must also remain open to ensure stable pressure conditions within the system.

The eDiluter™ Pro operates in three main modes: warmup, standby, and measurement. During warmup and standby, the system operates in a flush mode in which dilution air flows outward from the inlet. This outward flow prevents contamination and clogging of the ejector nozzles, particularly during high-temperature or soot-rich experiments. In measurement mode, the flush is disabled and the aerosol sample is actively drawn into the diluter for controlled two-stage dilution. This operational sequence (**figure 2.2**) is critical for ensuring reproducible dilution conditions and minimizing fouling during prolonged experimental campaigns.

In the present study, the eDiluter™ Pro was employed during controlled chamber experiments to dilute combustion-generated aerosols prior to optical and microphysical characterization. The two-stage ejector dilution combined with heated primary dilution air ensured stable thermodynamic conditioning and prevented instrument saturation during measurements with AE33, nephelometer, PAX, and particle sizing systems. The controlled dilution framework was therefore essential for maintaining linear instrument response and ensuring reproducibility of high-concentration combustion aerosol measurements.

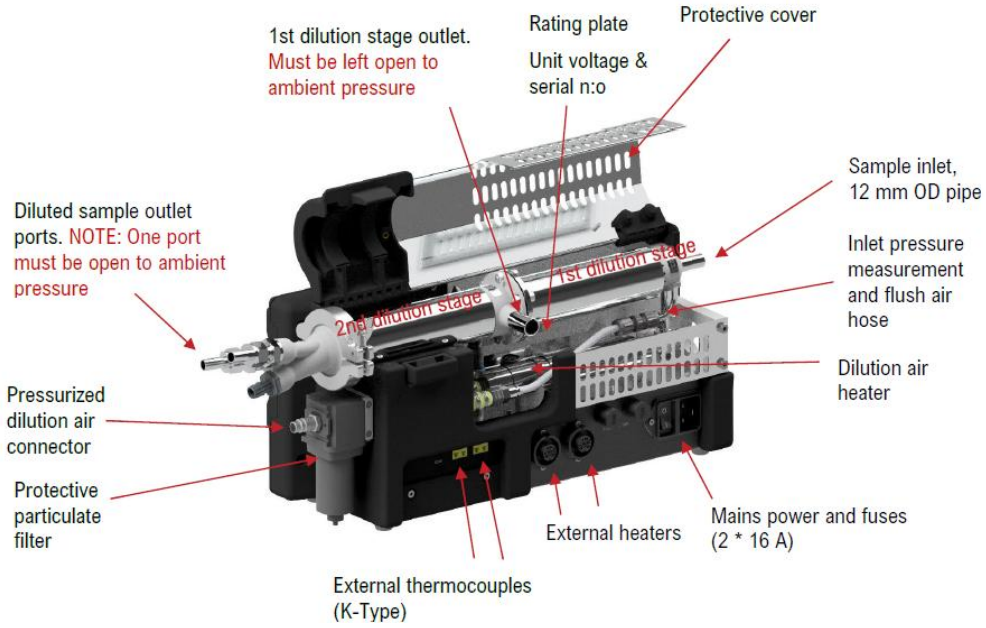

Figure 2.2: *Main components of the Dekati eDiluter Pro aerosol dilution system (Dekati Ltd., eDiluter Pro User Manual, Version 1.5).*

2.3: Soot Generator

Soot particles used in this work were generated using a combustion-based aerosol generator, namely the Mini Inverted Soot Generator (MISG, Argonaut Scientific Corp., Canada). Combustion-driven soot generators are widely employed in laboratory studies because they provide stable and reproducible particle emissions with controlled physicochemical properties comparable to atmospheric soot (Kazemimanesh et al., 2019). The MISG operates as an inverted-flame diffusion burner, a configuration in which fuel and oxidizer flow counter to the flexible motion of hot exhaust gases. This inverted geometry enhances flame stability by reducing flame-tip flickering and producing a steady co-flow diffusion flame (Stipe et al., 2005; Kirchstetter and Novakov, 2007), thereby ensuring consistent soot production.

The efficiency of the combustion process is controlled by adjusting the fuel-to-air ratio and is commonly expressed through the global equivalence ratio ϕ, defined as:

$$\phi = \frac{(F/A)_{actual}}{(F/A)_{stoichiometric}} \qquad (2.3)$$

where $(F/A)_{actual}$ is the actual fuel-to-air ratio and $(F/A)_{stoichiometric}$ is the stoichiometric ratio. When $\phi = 1$, combustion is stoichiometric; fuel-lean conditions correspond to $\phi < 1$, while fuel-rich conditions ($\phi > 1$) favor soot formation. Under complete combustion, the exhaust consists primarily of CO_2 and minor NO_x, whereas incomplete combustion produces soot and additional carbonaceous by-products (Kirchstetter and Novakov, 2007). Variations in the equivalence ratio directly affect particle concentration, morphology, primary particle size, and aggregate structure.

The MISG used in this study was operated with high-purity fuels such as propane used as a fuel and compressed air as oxidizer. Gas flow rates were regulated using two mass flow controllers (MFCs) controlled via a custom LabVIEW interface. The air flow was adjustable between 0 and 12 L min^{-1}, and the propane flow between 0 and 200 mL min^{-1}. For the experiments presented here, the air flow rate was set to 7 L min^{-1} and the propane flow to 75 mL min^{-1}. Under comparable operating conditions, previous characterization studies have reported soot particle number concentrations up to approximately 10^7 particles cm^{-3} and mobility diameters ranging from tens to several hundreds of nanometers (Kazemimanesh et al., 2019; Vernocchi et al., 2022).

A distinctive feature of the MISG design is that no external carrier gas is required. The inlet air stream is internally divided between combustion and dilution of the exhaust products, simplifying operation and improving reproducibility compared to systems requiring additional dilution gases (Kazemimanesh et al., 2019).

Soot generation experiments were conducted inside the atmospheric simulation chamber. Prior to aerosol injection, the burner was allowed to stabilize for approximately 45 minutes to ensure steady-state combustion. Combustion products were then injected into the chamber for periods ranging from 30 seconds to 2 minutes, depending on the target soot concentration. After injection, the chamber atmosphere was homogenized using the internal mixing fan for approximately 3 minutes to ensure spatial uniformity. A detailed

physicochemical characterization of MISG-generated soot in ChAMBRe under similar combustion conditions has been reported by Vernocchi et al. (2022).

Both fresh (non-aged) and aged so-called samples were produced. Aging experiments were performed by allowing the aerosol to evolve under controlled chamber conditions.

Aerosol sampling was performed on 47 mm quartz fiber filters (Pall TISSUQUARTZ, 2500QAO-UP) using a low-volume sampler without aerodynamic size cut. Under the selected combustion conditions, the fraction of particles larger than 10 µm is negligible, as demonstrated in previous chamber studies (Vernocchi et al., 2022). Sampling flow rates and durations were adjusted to obtain a wide range of filter loadings suitable for optical and chemical analyses.

Figure 2.3: *The Mini-Inverted Soot Generator (Argonaut Scientific).*

2.4: Diesel Generator

Diesel exhaust aerosols were produced using a Hyundai diesel electrical generator (model 65230) and introduced into the atmospheric simulation chamber using the same coupling concept adopted for MISG injections. The sampling and injection strategy for introducing combustion aerosols into ChAMBRe, including the use of dedicated connection lines and chamber mixing procedures, is described in detail by Vernocchi et al. (2022). The exhaust line connecting the generator to the chamber was assembled using sealed stainless-steel

fittings and vacuum flanges to minimize leakage and prevent uncontrolled dilution of the exhaust stream prior to injection.

The generator is powered by a 12 HP, four-stroke compression-ignition engine designed to operate with standard diesel fuel. In this work, the system was additionally modified to allow operation with hydrotreated vegetable oil (HVO) through a secondary fuel tank. HVO is a paraffinic renewable diesel fuel produced by hydrotreatment processes; its composition differs from conventional diesel in terms of aromatic and sulfur content, which can influence particulate emissions and soot formation in diesel combustion. Evidence for the use of HVO in diesel engines and its effect on emissions is documented in the heavy-duty engine literature (Kuronen et al., 2007). Between fuel changes, the engine was operated under stabilized conditions to reduce the likelihood of residual fuel mixing in the delivery system, so that the produced aerosol could be attributed consistently to the selected fuel.

The generator class is consistent with the European regulatory framework for non-road mobile machinery engines. In particular, the relevant emission limits are defined under Regulation (EU) 2016/1628 (“Stage V”), which sets requirements for gaseous and particulate pollutant emissions, including particle number limits for several engine categories. This regulatory context is important because after-treatment systems required to meet modern standards can influence both the magnitude and the composition of emitted particulate matter.

Diesel exhaust injection into ChAMBRe was performed for short time intervals (typically a few seconds) to avoid excessive chamber concentrations and to maintain operation within the dynamic range of the real-time instruments. After injection, the chamber air was mixed to improve spatial uniformity prior to subsequent sampling and optical measurements, following the same general approach used in previous ChAMBRe combustion aerosol studies.

Figure 2.4: *Portable Hyundai diesel generator used for Diesel and HVO particles during ChAMBRe experiments.*

2.5: Aerosol samplers

Aerosol sampling represents a fundamental step in particulate matter analysis, as it ensures that a representative mass of particles is collected for subsequent gravimetric, chemical, and optical characterization. The primary objective is to obtain sufficient deposited material on a filter substrate while maintaining a predefined aerodynamic size cut, typically PM_{10} or $PM_{2.5}$. A low-volume aerosol sampler generally consists of a regulated pump, a size-selective inlet (often an impactor), and a filter holder positioned directly below the inlet. The pump operates under feedback control to maintain constant volumetric flow despite increasing filter loading. Sequential samplers additionally incorporate an automatic filter exchange mechanism, enabling unattended operation over extended sampling periods.

During this PhD work, both sequential and single-filter sampling systems were employed for outdoor field campaigns and chamber experiments. Outdoor sampling was performed using Skypost low-volume sequential samplers (TCR-Tecora, Italy) and Giano BC1 sequential samplers (DadoLab). The Giano sampler belongs to the PMx sequential sampler family (Giano & Gemini models), based on a multi-purpose core (MPC) that manages single- or dual-channel sampling and allows either outdoor cabinet installation or 19” rack configuration. The outdoor version weighs approximately 35 kg (excluding the sampling head) and is designed with forced internal air recirculation to maintain filters close to ambient temperature during operation.

The sequential samplers were operated at a nominal flow rate of 38.3 L min^{-1} for outdoor campaigns, corresponding to the European low-volume reference standard for $PM_{2.5}$ and PM_{10} sampling. Flowrate is digitally controlled through an orifice meter with an accuracy better than ±1%, ensuring stable and traceable volume measurements. The sampling pump, positioned downstream of the filter, has a nominal capacity up to 70 L min^{-1} and is designed for maintenance-free operation exceeding 12,000 hours. The pneumatic circuit includes a straight, insulated aluminum inlet tube engineered to minimize kinetic, thermal, chemical, and electrostatic particle losses. Size-selective sampling was achieved using interchangeable EN-LVS heads with PM_{10} or $PM_{2.5}$ impactor stages operating at 2.3 m^3 h^{-1} (38.3 L min^{-1}).

The Giano system can accommodate up to 21 blank/exposed filters, enabling unattended sampling for extended periods depending on the selected time schedule. After sampling, exposed filters are transferred to a storage tank. To comply with EN12341 requirements and reduce losses of semi-volatile compounds, an integrated conditioning system maintains the filter storage temperature below 23–25°C under high ambient temperature conditions. All relevant parameters, including flowrate, sampled volume, temperature, pressure, and relative humidity, are logged by the MPC unit and can be exported via USB or remote communication interfaces.

Following collection, filters were conditioned for 48 hours at controlled laboratory conditions (20 °C and 50% relative humidity) prior to gravimetric and chemical analysis to ensure mass stability. The combination of standardized flow control, aerodynamic size selection, temperature-conditioned storage, and digital data logging provided reliable and traceable $PM_{2.5}$ and PM_{10} samples for subsequent analytical procedures conducted in this thesis.

Figure 2.5: *Aerosol sampling and conditioning unit used for filter-based measurements.*

2.6: Particle Size Distribution

The particle number concentration and size distribution within the chamber were continuously monitored using two instruments: a Scanning Mobility Particle Sizer (SMPS, TSI Inc., Shoreview, MN, USA, Model 3938) and an Optical Particle Sizer (OPS, TSI Inc., Shoreview, MN, USA, Model 3330). The SMPS measures particles with diameters below 1 µm, which constitute the main size range investigated in this thesis. The OPS complements these measurements by covering larger particle sizes. The combined use of both instruments allows a detailed characterization of aerosol size distributions inside the chamber.

2.6.1: Scanning Mobility Particle Sizer (SMPS)

Particle size distributions in the submicron range were measured using a Scanning Mobility Particle Sizer (SMPS) system (TSI Inc., USA). The SMPS is a widely used

instrument for characterizing aerosol particles based on their electrical mobility diameter, allowing high-resolution measurements of particle size distributions typically in the range from a few nanometers up to several hundred nanometers (Wang and Flagan, 1990; Kulkarni et al., 2011). The system used in this work consisted of an electrostatic classifier with a Differential Mobility Analyzer (DMA) coupled with a Condensation Particle Counter (CPC).

The measurement principle (figure 2.6) is based on the electrical mobility of charged particles in an electric field. The sampled aerosol first passes through a neutralizer that establishes a predictable charge distribution on the particles. The aerosol then enters the Differential Mobility Analyzer, where particles are separated according to their electrical mobility by applying a controlled electric field between two cylindrical electrodes. Only particles with a specific electrical mobility exit the classifier at a given voltage. By continuously scanning the applied voltage, the DMA selects particles of different mobility diameters sequentially (Wang and Flagan, 1990).

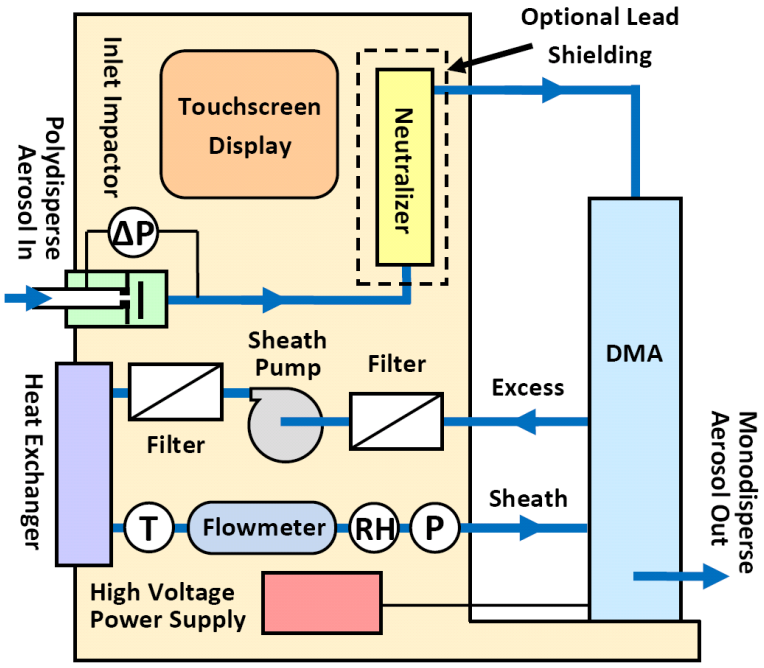

Figure 2.6: *Working principle of the Differential Mobility Analyzer (DMA) used for aerosol size selection and mobility-based particle classification.*

The classified particles are subsequently detected by a Condensation Particle Counter (CPC). Inside the CPC, particles act as condensation nuclei for a working fluid, typically butanol. Vapor condenses on the particles, growing them into droplets large enough to be detected optically. Each droplet is counted individually by a photodetector, allowing accurate determination of particle number concentration (TSI, 2013a). By combining the electrical mobility classification from the DMA with particle counting from the CPC, the SMPS reconstructs the aerosol number size distribution as a function of particle mobility diameter.

In this PhD work, the SMPS system was connected to the atmospheric simulation chamber to characterize the size distribution of laboratory-generated aerosols. The instrument was used during experiments involving synthetic soot generation and aerosol aging processes. The SMPS provided detailed information on particle number concentration and size evolution in the nanometer range, which is essential for understanding aerosol formation processes and the microphysical properties of soot particles generated inside the chamber. These measurements were also important for interpreting optical properties measured by instruments such as AE33, PAXs, MWAA and BLAnCA, since aerosol optical behavior strongly depends on particle size distribution.

2.6.2: Optical Particle Sizer (OPS)

Particle size distributions in the micrometer range were measured using an Optical Particle Sizer (OPS, Model 3330, TSI Inc., USA). The OPS determines aerosol particle size distributions using single-particle optical scattering, providing real-time measurements of particle number concentration and size distribution typically in the range 0.3–10 μm (TSI, 2011).

The operating principle of the OPS (figure 2.7) is based on the scattering of light by individual particles passing through a focused laser beam. Aerosol particles are drawn into the instrument through an inlet and transported into an optical detection chamber by a controlled airflow. As each particle passes through the laser beam, it scatters light that

is detected by a photodetector. The intensity of the scattered light pulse is proportional to the optical diameter of the particle, allowing the instrument to classify particles into predefined size bins (Kulkarni et al., 2011).

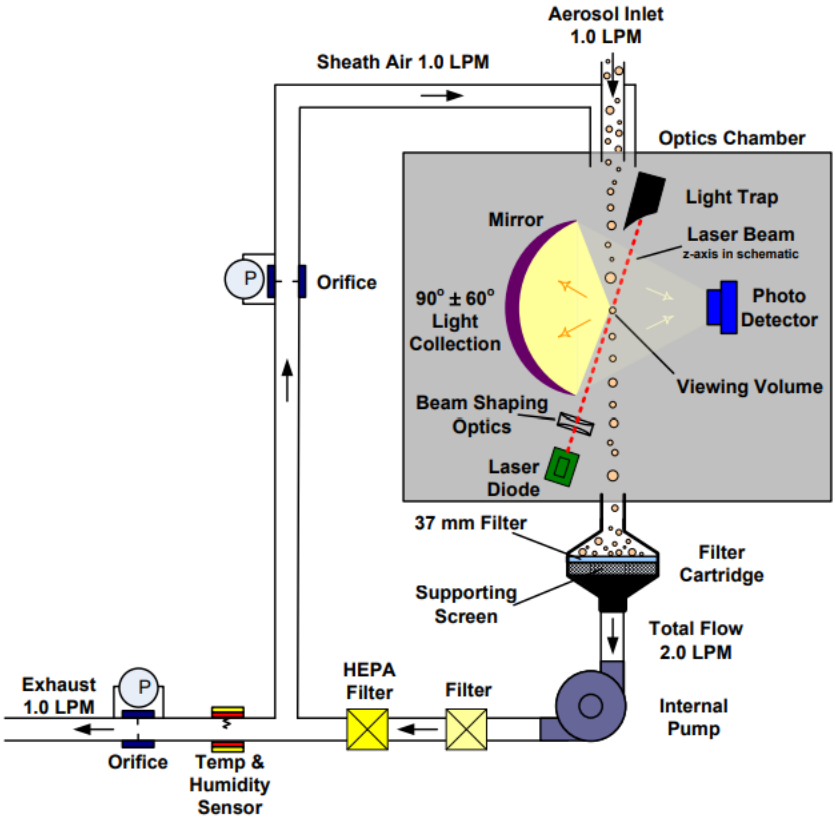

Figure 2.7: *Schematic diagram of the Optical Particle Sizer measurement principle.*

To ensure accurate measurement, the OPS uses a controlled aerosol flow and sheath airflow system that focuses particles into the sensing region so that they pass individually through the laser beam. The instrument then records the number of detected particles in each size channel and reconstructs the particle size distribution in real time. The OPS can also provide estimates of particle mass concentration based on assumptions about particle density and refractive index (TSI, 2011).

During the chamber experiments, the OPS was connected to the sampling ports of the chamber to monitor particle size evolution during soot generation experiments and aerosol aging processes. These measurements were particularly important for identifying

particle growth, coagulation processes, and the formation of larger aggregates. The size distribution data obtained from the OPS complemented the SMPS measurements and provided valuable information for interpreting aerosol optical measurements performed

2.7: Optical Properties of Aerosols

The optical properties of aerosols were investigated through both controlled chamber experiments and field campaigns conducted in Genova, Italy, and Lahore, Pakistan. The aim was to quantify aerosol–radiation interactions and to evaluate the contribution of carbonaceous components to atmospheric light absorption and scattering under laboratory and real-world conditions.

Real-time measurements of aerosol optical properties were performed using an Aethalometer and a Nephelometer, which continuously provided absorption (σ_abs) and scattering (σ_sca) coefficients, respectively. These high time-resolution observations allowed the characterization of aerosol optical evolution during chamber experiments as well as temporal variability in ambient environments.

In addition, offline optical analyses were conducted on particles collected on quartz and Teflon filters. The wavelength-dependent absorption properties were determined using the Multi-Wavelength Absorption Analyzer (MWAA) and the Broadband Light Absorption Analyzer of Complex Aerosols (BLAnCA). The integration of online and filter-based techniques enabled a comprehensive assessment of key intensive optical parameters, including single scattering albedo (SSA), absorption and scattering Ångström exponents, and mass absorption cross section (MAC).

This combined approach strengthens the comparison between chamber-generated aerosols and ambient particles, improving the understanding of emission sources, aging mechanisms, and their radiative implications in different atmospheric contexts.

2.7.1: Multi-Wavelength Absorbance Analyzer (MWAA)

The Multi-Wavelength Absorbance Analyzer (MWAA) is an optical instrument developed at the Environmental Physics Laboratory of the Department of Physics, University of Genoa, for the non-destructive analysis of particulate matter collected on

filters (Massabò et al., 2013; Massabò et al., 2015). The instrument was designed to determine the spectral light absorption of aerosol deposits and is particularly suited for the study of carbonaceous particulate matter sampled on fibrous filtering substrates such as quartz fiber filters. In contrast to real-time instruments, the MWAA is an offline technique, since it operates on particles previously collected on a filter support.

The instrument measures absorption at five wavelengths, namely 375, 405, 532, 635, and 870 nm, covering the spectral range from the near-ultraviolet to the near-infrared (Massabò et al., 2015). The illumination system consists of five low-power laser diodes, which are sequentially activated during the analysis. The laser sources are mounted on a remotely controlled chassis that ensures automatic alignment and repeatable beam positioning. The filter samples are mounted on an aluminum sample wheel capable of accommodating up to 16 filters. The wheel is rotated by a stepper motor to position each sample in front of the incident beam. In addition, the wheel assembly is mounted on a two-axis translation stage, which allows the filter surface to be scanned with millimetric steps in order to account for possible inhomogeneity of the particle deposit over the sampled area.

When the laser beam interacts with the filter, part of the radiation is transmitted, while another part is absorbed by the deposited aerosol. The optical signal is measured by three photodiodes. One detector is placed in the forward direction at 0° with respect to the incident beam to measure transmitted radiation, whereas two detectors are positioned in the backward hemisphere at 125° and 165° to detect backscattered light. The photodiodes have spectral sensitivity over the approximate range 200–1100 nm, allowing efficient detection of all five laser wavelengths. The current output generated by each photodiode is converted into voltage, amplified, and acquired through a multifunction data acquisition device. The full sequence of laser switching, sample positioning, signal acquisition, and analysis is managed through a dedicated LabVIEW control software.

The optical quantity directly determined from the comparison between blank and loaded filters is the absorbance, defined as

$$ABS(\lambda) = \ln\left(\frac{I_{\text{blank}}(\lambda)}{I_{\text{sample}}(\lambda)}\right) \qquad (2.4)$$

where $I_{\text{blank}}(\lambda)$ and $I_{\text{sample}}(\lambda)$ are the transmitted intensities measured at wavelength λ for the blank filter and the particle-loaded filter, respectively. After applying the radiative transfer correction scheme for transmission and backscattering, the corrected absorbance is converted into the aerosol **absorption coefficient** through

$$b_{\text{abs}}(\lambda) = \frac{ABS(\lambda)\,A}{V} \qquad (2.5)$$

where $\boldsymbol{A}$ is the effective sampled filter area and $\boldsymbol{V}$ is the volume of air passed through the filter during sampling. In this way, the MWAA provides the spectral absorption coefficient at the five operating wavelengths.

The wavelength dependence of absorption is commonly described through the Ångström Absorption Exponent (AAE), assuming a power-law relationship between absorption coefficient and wavelength (Ångström, 1964):

$$b_{\text{abs}}(\lambda) = K\,\lambda^{-AAE} \qquad (2.6)$$

or, equivalently, between two wavelengths $\lambda_1$and λ_2,

$$AAE = -\frac{\ln[b_{\text{abs}}(\lambda_1)/b_{\text{abs}}(\lambda_2)]}{\ln(\lambda_1/\lambda_2)} \qquad (2.7)$$

The AAE is widely used as an indicator of aerosol composition. Values close to 1 are generally associated with black carbon from fossil-fuel combustion, whereas larger values indicate stronger spectral dependence and may suggest contributions from brown carbon or biomass-burning aerosol (Bond and Bergstrom, 2006; Kirchstetter et al., 2004; Schnaiter et al., 2005).

In this PhD work, the MWAA was mainly used for the analysis of aerosol samples collected on quartz fiber filters, with the principal aim of supporting and validating the

absorption measurements obtained with BLAnCA. Each filter was scanned over a 6 mm grid centered on the geometrical centre of the deposit in order to reduce the effect of local inhomogeneities. Every sample was analysed at all five available wavelengths. In each 16-position wheel, the first position was occupied by a blank reference filter. When a batch contained more than fifteen samples, the same blank was reloaded in the first position of each new wheel, so as to minimize uncertainties related to small changes in measurement conditions, such as laser intensity fluctuations or instrumental drift during long acquisition sequences. This procedure improved the stability of the absorbance retrieval and ensured better consistency between different analytical runs.

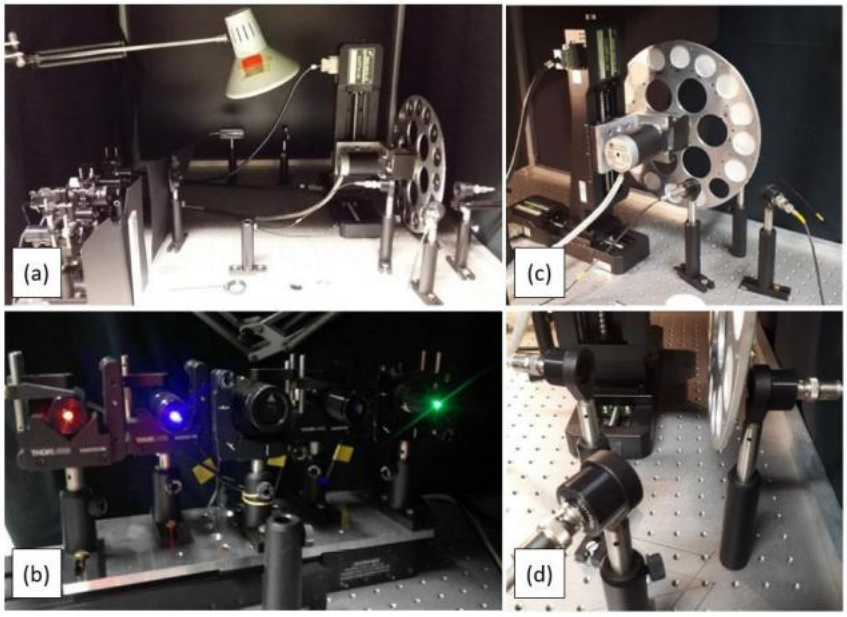

Figure 2.8: *Multi-Wavelength Absorption Analyzer (MWAA) system showing (a) overall experimental setup, (b) laser diode sources, (c) rotating sample wheel, and (d) photodiode detection system.*

2.7.2: Broadband Light Analyzer of Complex Aerosol (BLAnCA)

The Broadband Light Analyzer of Complex Aerosol (BLAnCA) is a laboratory instrument developed at the University of Genoa and INFN for the offline determination of the spectral light absorption coefficient of aerosol particles collected on filters

(Isolabella et al., 2025). The instrument was designed to overcome limitations of previous multi-wavelength absorption photometers, particularly the restricted spectral resolution and the dependence on simplified scattering assumptions (Massabò et al., 2013; Petzold and Schönlinner, 2004). BLAnCA performs high-resolution spectral measurements over a continuous wavelength range between 375 and 1000 nm, with a spectral resolution of 5 nm, thus providing 125 independent wavelength channels. This extended spectral capability enables the investigation of fine structures in the absorption spectrum that are not accessible with conventional instruments operating at a limited number of discrete wavelengths (Isolabella et al., 2025).

The optical system is assembled on a stabilized optical bench to ensure mechanical and optical alignment stability (Figure: 2.9). Illumination is provided by a broadband tungsten–halogen lamp (Mighty Light Plus, Spectrolight Inc.), characterized by a quasi-black-body emission spectrum with a maximum intensity around 680 nm. The emitted radiation is collimated onto the filter sample using either a standard light guide coupled to a system of 2cm convex lenses, producing a beam diameter of approximately 2cm, or an alternative fiber-coupled configuration yielding a reduced beam diameter of approximately 0.6cm for samples deposited on smaller areas. Although the spectrometer nominal range extends from 200 to 1100 nm, the effective operational range of the instrument is 375–1000 nm, where the signal-to-noise ratio remains sufficiently high for reliable analysis.

Transmitted and scattered radiation from the filter sample is collected through a UV–VIS–NIR optical fiber and directed to a CMOS spectrometer (AvaSpec ULS2048CL, Avantes BV) with a spectral resolution of 5nm. A defining feature of BLAnCA is the implementation of a motorized rotating detection arm positioned at a distance of 6cm from the sample. The arm rotates in the horizontal plane with a minimum angular step of 0.1°, enabling the high-resolution measurement of the angular scattering profile. This configuration allows direct integration of scattered radiation over the forward and backward hemispheres, in contrast to instruments such as MAAP or MWAA, which rely

on measurements at fixed scattering angles (Petzold and Schönlinner, 2004; Massabò et al., 2013).

The determination of aerosol absorbance is based on the radiative transfer formalism introduced by Hänel (1987, 1994) and subsequently refined by Petzold and Schönlinner (2004). The measured absorbance is defined as

$$ABS = (1 - \omega)\tau \qquad (2.8)$$

where $\boldsymbol{\omega}$ is the single-scattering albedo and $\boldsymbol{\tau}$ is the optical thickness of the aerosol–filter layer. The absorbance is obtained by solving the radiative budget equations using the experimentally determined forward and backward scattering intensities (Hänel, 1987, 1994; Petzold and Schönlinner, 2004).

Measurements are performed on both particle-loaded filters and blank reference filters in order to correct for the optical contribution of the filter matrix. The aerosol absorption coefficient b_{abs}(Mm^{-1}) is then derived from the absorbance according to

$$b_{abs} = ABS \cdot \frac{A}{V} \qquad (2.9)$$

where $\boldsymbol{A}$ is the effective aerosol deposition area on the filter and $\boldsymbol{V}$ is the total sampled air volume (Isolabella et al., 2025). This approach ensures that multiple scattering effects within the filter matrix are explicitly accounted for in the retrieval procedure.

In summary, BLAnCA represents a significant advancement in offline aerosol optical characterization, combining high spectral resolution, direct hemispherical scattering integration, and robust radiative transfer modeling. Its capability to resolve spectral curvature and absorption features provides enhanced potential for aerosol source apportionment and for the investigation of the radiative properties of carbonaceous and mineral aerosols.

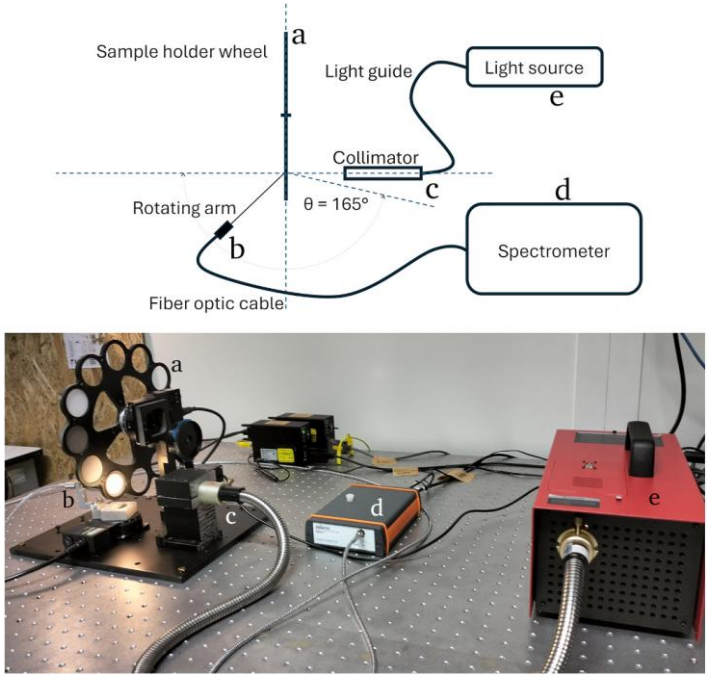

Figure 2.9. *Schematic diagram of the Broadband Light Analyzer of Complex Aerosol (BLAnCA). setup showing the broadband tungsten–halogen light source, collimation (adapted from Isolabella et al., 2025).*

2.8: Aethalometer AE33

The Aethalometer AE33 is a real-time optical instrument designed for continuous measurement of aerosol light absorption and the determination of equivalent black carbon (eBC) concentrations. The instrument is based on the filter attenuation principle originally introduced by Hansen et al. (1984), in which the attenuation of light transmitted through a particle-loaded filter is used to quantify light-absorbing aerosol components. In this method, aerosol particles are continuously collected on a quartz fiber filter tape while the transmitted light intensity is monitored to determine the increase in optical attenuation.

The optical attenuation (ATN) is defined as:

$$ATN = 100 \cdot \ln\left(\frac{I_0}{I}\right) \qquad (2.10)$$

where $\boldsymbol{I_0}$ represents the transmitted light intensity through a clean filter spot and $\boldsymbol{I}$ is the transmitted intensity after particle deposition (Hansen et al., 1984). As particles accumulate on the filter, attenuation increases proportionally to the absorbing material deposited. However, filter-based techniques are subject to artefacts related to multiple scattering within the filter matrix and loading effects caused by increasing particle accumulation (Weingartner et al., 2003).

The AE33 represents a significant improvement over previous Aethalometer models through the implementation of a dual-spot loading compensation algorithm (Drinovec et al., 2015). In this configuration, aerosol is simultaneously deposited onto two filter spots operating at different flow rates. By comparing the attenuation rates of the two spots, the instrument dynamically determines and corrects for the filter loading effect in real time. This approach substantially reduces non-linear response behavior and improves the accuracy and stability of the absorption coefficient derived.

The AE33 measures attenuation at seven wavelengths (typically 370, 470, 520, 590, 660, 880, and 950 nm), covering the near-UV to near-IR spectral region. The multi-wavelength capability allows the calculation of the spectral absorption coefficient and the absorption Ångström exponent (AAE), defined as:

$$AAE = -\frac{\ln(b_{abs}(\lambda_1)/b_{abs}(\lambda_2))}{\ln(\lambda_1/\lambda_2)} \qquad (2.11)$$

which is commonly used for source apportionment studies (Sandradewi et al., 2008). Absorption that is nearly wavelength independent (AAE ≈ 1) is typically associated with fossil-fuel black carbon, whereas enhanced absorption at shorter wavelengths (AAE > 2) indicates contributions from brown carbon or biomass burning emissions (Bond and Bergstrom, 2006; Sandradewi et al., 2008).

The absorption coefficient measured by the AE33 is converted into equivalent black carbon concentration (eBC) through the application of a mass absorption cross-section (MAC). At 880 nm, which is generally considered a reference wavelength for black carbon, a commonly adopted MAC value is 7.77 $m^2\ g^{-1}$ (Bond and Bergstrom, 2006). The term “equivalent black carbon” is recommended to emphasize that the derived

concentration is based on optical absorption rather than direct chemical quantification (Petzold et al., 2013).

Despite the improvements introduced by the dual-spot correction scheme, the AE33 remains an attenuation-based instrument and does not directly measure scattered radiation. Consequently, residual uncertainties related to multiple scattering and filter matrix interactions may persist, and intercomparison with reference techniques such as photoacoustic instruments or multi-angle absorption photometers is often recommended (Weingartner et al., 2003; Petzold et al., 2013). Nevertheless, the AE33 provides robust, high-time-resolution measurements of aerosol absorption and eBC concentration and is widely used in both chamber studies and field campaigns.

Figure 2.10: *AE33 Aethalometer used for real-time measurement of aerosol light absorption and black carbon concentration.*

In the present work, the AE33 was employed for continuous monitoring of aerosol light absorption during chamber experiments and field measurements. Its high temporal resolution complements the high spectral resolution offline measurements performed with MWAA and BLAnCA, enabling a comprehensive characterization of the optical properties of carbonaceous aerosols.

2.9: Integrating Nephelometer (Aurora 4000)

The integrating nephelometer is a real-time optical instrument designed to measure the aerosol light scattering coefficient. In the present study, aerosol scattering measurements

were performed using the Aurora 4000 integrating nephelometer (Ecotech Pty Ltd., Australia). The instrument determines total and hemispherical scattering coefficients at three wavelengths (typically 450, 525, and 635 nm), allowing evaluation of the spectral dependence of scattering and inference of particle size characteristics.

The operating principle of the integrating nephelometer is based on the angular integration of light scattered by aerosol particles suspended in an illuminated sampling chamber (Heintzenberg and Charlson, 1996). The fundamental quantity measured is the volume scattering coefficient, σ_{sca}(Mm^{-1}), defined as:

$$\sigma_{sca} = \int_{4\pi} \frac{d\sigma}{d\Omega}\, d\Omega \qquad (2.12)$$

where $\frac{d\sigma}{d\Omega}$ represents the differential scattering cross-section per unit solid angle. In practice, complete 4π integration is not achievable; therefore, the Aurora 4000 integrates scattered radiation over a limited angular range (approximately 10°–170°), excluding the extreme forward and backward directions.

This limited angular detection leads to the so-called truncation error, which causes underestimation of total scattering, particularly for coarse-mode particles exhibiting strong forward scattering (Anderson and Ogren, 1998). To correct for this effect, truncation correction factors based on Mie theory calculations or measured size distributions are typically applied (Anderson and Ogren, 1998). In this study, truncation corrections were implemented following established methodologies to ensure consistency with extinction calculations and intercomparison with absorption measurements.

The Aurora 4000 employs high-intensity LED light sources and photomultiplier detectors positioned within an integrating cavity. In addition to total scattering, the instrument provides backscattering measurements, enabling the determination of the backscattering fraction. The availability of three wavelengths permits calculation of the scattering Ångström exponent (SAE):

$$SAE = -\frac{\ln(\sigma_{sca}(\lambda_1)/\sigma_{sca}(\lambda_2))}{\ln(\lambda_1/\lambda_2)} \quad (2.13)$$

which is commonly used as an indicator of particle size distribution, with larger values generally corresponding to fine-mode dominance (Heintzenberg and Charlson, 1996).

Calibration of the nephelometer was performed using particle-free air for zero determination and high-purity carbon dioxide (CO_2) for span calibration, following the manufacturer's recommendations (Ecotech, Aurora 4000 User Manual). CO_2 is used due to its well-characterized Rayleigh scattering coefficient, providing traceable and reproducible calibration of the instrument's optical response (Müller et al., 2011). Periodic zero checks were conducted during both chamber and field measurements to ensure baseline stability and minimize drift.

The instrument operated at a controlled flow rate of 5 LPM during field campaigns. Data were recorded at one-second resolution and averaged to appropriate temporal intervals for analysis. Since aerosol scattering is strongly influenced by relative humidity due to hygroscopic growth, ambient temperature and relative humidity were monitored during measurements. Hygroscopic enhancement of scattering at elevated humidity is a well-known effect and can significantly increase σ_{sca} under humid conditions (Heintzenberg and Charlson, 1996). Where necessary, humidity effects were considered in data interpretation.

The scattering coefficient measured by the nephelometer was combined with the absorption coefficient obtained from the AE33 Aethalometer or CASS system to derive the extinction coefficient:

$$\sigma_{ext} = \sigma_{abs} + \sigma_{sca} \quad (2.14)$$

and the single scattering albedo (SSA):

$$SSA = \frac{\sigma_{sca}}{\sigma_{ext}} \quad (2.15)$$

The SSA represents a key intensive optical parameter governing aerosol radiative forcing. Lower SSA values indicate absorption-dominated aerosol typical of traffic-influenced

environments, whereas higher SSA values are characteristic of aged or secondary aerosol-rich conditions.

Figure 2.11: *Ecotech Aurora 4000 integrating nephelometer used for real-time measurement of aerosol scattering properties.*

In the present study, the Aurora 4000 nephelometer provided continuous scattering measurements during both controlled chamber experiments and ambient field campaigns. The integration of nephelometer-derived scattering with Aethalometer-derived absorption enabled a comprehensive assessment of aerosol extinction, spectral behavior, and radiative properties

2.10: Total Carbon Analyzer, Model TCA08

The Magee Scientific Total Carbon Analyzer (TCA08) is an automated online instrument for the determination of total carbon (TC) in atmospheric particulate matter. The instrument combines filter-based particle collection with rapid thermal oxidation and nondispersive infrared (NDIR) detection of the produced carbon dioxide (CO_2). Continuous measurements of total carbon are particularly relevant for carbonaceous aerosol studies, as carbon constitutes a significant fraction of $PM_{2.5}$ mass and contributes to both air quality and radiative effects (Petzold et al., 2013).

During operation, aerosol particles are collected on pre-fired quartz fiber filters at a controlled flow rate of 16.7 LPM. Quartz filters are widely used in carbon analysis due

to their thermal stability and low background carbon content (Chow et al., 2007). The TCA08 employs two identical sampling and analysis channels that operate alternately: while one channel collects particles for the next sampling interval, the second channel performs thermal analysis of the previously collected sample. This dual-channel configuration allows uninterrupted continuous monitoring.

After completion of the sampling period, the loaded filter is rapidly heated in an oxidizing environment, converting all carbonaceous material to CO_2. The resulting CO_2 pulse is measured by an NDIR detector, and the total carbon mass collected on the filter is determined by integrating the excess CO_2 signal above baseline. The total carbon concentration is calculated as

$$TC = \frac{m_C}{V} \qquad (2.16)$$

where m_C is the carbon mass evolved during combustion and V is the air volume is sampled.

Unlike thermal–optical protocols such as the IMPROVE or NIOSH methods, which distinguish organic carbon (OC) and elemental carbon (EC) through stepwise heating and optical correction (Chow et al., 2007), the TCA08 provides a bulk measurement of total carbon without fractionation. The advantage of this approach lies in operational simplicity and suitability for high-time-resolution monitoring, while OC and EC separation must be performed indirectly if required.

Quartz filter sampling is known to be affected by positive artefacts caused by adsorption of gas-phase organic compounds (Turpin et al., 2000). To reduce this effect, the TCA08 incorporates an upstream activated carbon denuder, which removes volatile organic vapors before particle collection. This configuration improves selectivity toward particulate-phase carbon.

When operated in parallel with optical absorption measurements (e.g., AE33 Aethalometer), total carbon data can be combined with black carbon measurements to estimate organic carbon through a mass balance approach. In such applications, the total

carbon measurement provides a robust indicator of bulk carbon loading, while optical measurements characterize the light-absorbing fraction.

Figure 2.12: *TCA08 thermal carbon analyzer for real-time determination of carbonaceous aerosol components based on thermal evolution and oxidation.*

In the present study, the TCA08 was used for continuous measurement of total carbon during chamber experiments and field campaigns. The instrument provided time-resolved TC data that was analyzed together with absorption and scattering measurements to investigate the relationship between carbon mass concentration and aerosol optical properties.

2.11: Thermal–Optical Analysis Using the Sunset OC/EC Analyzer

The quantification of organic carbon (OC) and elemental carbon (EC) in particulate matter samples was performed using a Sunset Laboratory thermal–optical carbon analyzer (Sunset Laboratory Inc., USA). This instrument determines the concentration of carbonaceous fractions collected on quartz fiber filters through the thermal–optical transmittance (TOT) technique, which is widely used in atmospheric aerosol research (Birch and Cary, 1996; Chow et al., 1993; Huntzicker et al., 1982). Quartz fiber filters are employed because they can withstand the high temperatures required during thermal analysis without structural degradation.

In thermal–optical analysis, a small punch (typically 1 cm^2) is extracted from the sampled filter and placed inside a quartz oven, where it undergoes a controlled sequence of heating

steps. The analysis consists of two main phases characterized by different atmospheric conditions and temperature profiles. During the first phase, known as the inert phase, the sample is heated in a pure helium atmosphere. Under these conditions, organic carbon compounds volatilize and evolve from the filter as the temperature increases. The temperature is raised stepwise according to a predefined thermal protocol. An example of the resulting thermogram is shown in **Figure 2.13**, where region *a* corresponds to the inert heating stage.

In thermal–optical analysis, a small punch (typically 1 cm^2) is extracted from the sampled filter and placed inside a quartz oven, where it undergoes a controlled sequence of heating steps. The analysis consists of two main phases characterized by different atmospheric conditions and temperature profiles. During the first phase, known as the inert phase, the sample is heated in a pure helium atmosphere. Under these conditions, organic carbon compounds volatilize and evolve from the filter as the temperature increases. The temperature is raised stepwise according to a predefined thermal protocol. An example of the resulting thermogram is shown in **Figure 2.13**, where region *a* corresponds to the inert heating stage.

After completion of the inert phase, the oven is cooled and an oxidizing mixture containing helium and oxygen is introduced into the combustion chamber. This marks the beginning of the second heating stage, referred to as the oxidizing phase (region *b* in the thermogram), during which elemental carbon present in the sample is combusted. The analytical procedure and gas conversion process are described in the following section.

The evolved gases are transported by the carrier gas through an oxidizing catalyst where carbon-containing compounds are converted to CO_2 at high temperature (approximately 870 °C). The CO_2 is then reduced to methane (CH_4) in a methanation operating at about 500 °C in a hydrogen atmosphere. The methane is finally detected by a flame ionization detector (FID), which measures the concentration of carbon released from the filter. In the FID, methane molecules are ionized in a hydrogen flame, producing charged fragments whose electrical current is proportional to the carbon mass evolved during the analysis (Birch and Cary, 1996).

A known challenge of thermal–optical carbon analysis is the formation of pyrolytic carbon during the inert heating phase. Some organic compounds can undergo thermal decomposition and form a refractory carbonaceous material known as pyrolytic carbon (often denoted as PyC or PYRC). This carbonized material behaves similarly to elemental carbon and can oxidize during the second heating phase. If not properly corrected, this process may lead to an overestimation of EC and a corresponding underestimation of OC (Chow et al., 2007).

To correct for this artifact, the instrument incorporates an optical monitoring system consisting of a laser diode operating at a wavelength of 635 nm. The laser beam continuously passes through the filter during the analysis, and the transmitted light intensity is monitored. Because elemental and pyrolytic carbon absorbs visible light whereas organic carbon does not, changes in laser transmittance provide information on the formation and removal of light-absorbing carbon. During the inert phase, pyrolysis causes the filter to darken and the laser transmittance decreases. During the oxidizing phase, the combustion of pyrolytic and elemental carbon progressively restores the filter transparency and the transmitted signal increases.

The point at which the laser transmittance returns to its initial value is defined as the split point. At this moment, the amount of pyrolytic carbon that formed during the inert phase is assumed to have been completely removed. Carbon evolved before this split point is therefore assigned to the organic carbon fraction, while carbon evolved afterward is attributed to elemental carbon.

Different thermal protocols can be applied in thermal–optical analysis depending on the measurement objective and regional standardization. These protocols differ mainly in the temperature set points and residence times used during each heating step. Among the most commonly adopted protocols are NIOSH, IMPROVE, and EUSAAR-2 (Cavalli et al., 2010; Chow et al., 1993; Peterson and Richards, 2002). In this work, analyses were performed using the NIOSH protocol, which reaches a maximum temperature of approximately 940 °C during the oxidizing phase. This higher temperature ensures complete oxidation of refractory carbonaceous material, thereby minimizing the risk of

incomplete EC combustion that may occur with lower-temperature protocols such as EUSAAR-2.

Prior to each measurement session, a clean oven check was performed to verify the background signal of the instrument. This procedure consists of running a complete thermal cycle using a blank quartz filter punch to ensure that the baseline CO_2 signal is negligible and that no residual contamination is present in the combustion chamber. This step is essential to guarantee accurate quantification of carbonaceous fractions.

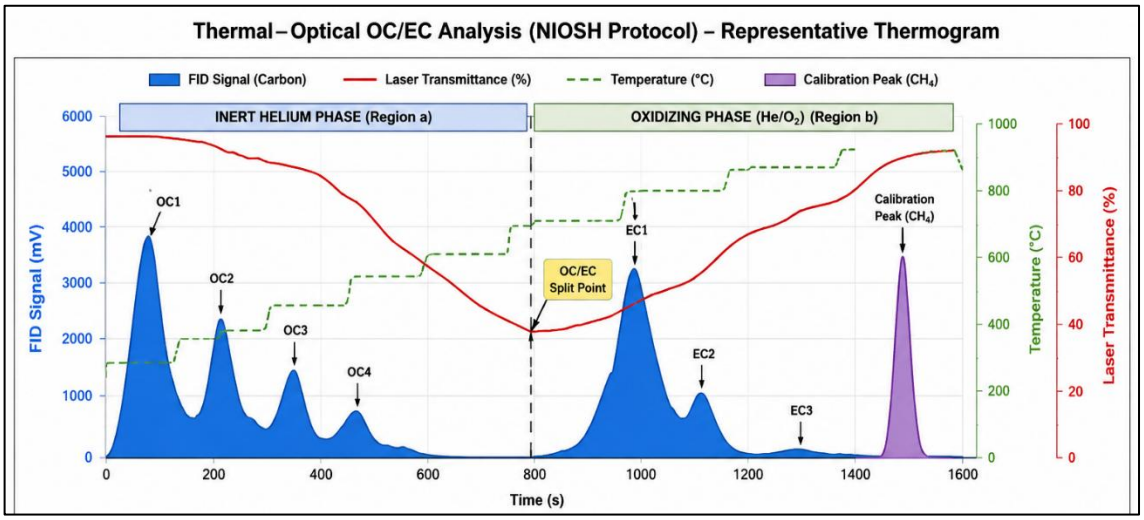

Figure 2.13: *Representative thermogram from thermal–optical OC/EC analysis using the NIOSH protocol in transmittance mode.*

The instrumentation and experimental configurations described in this chapter form the basis for the methodologies presented in Chapter 3. While this chapter focuses on the setup and operating principles of the instruments, the following chapter details the sampling procedures, data processing, and analytical approaches used in this study.

CHAPTER 3: Materials And Methods

3.1 Overview of the Experimental Approach

This study was designed to investigate the optical and chemical properties of $PM_{2.5}$ under both controlled laboratory conditions and real atmospheric environments. The integration of chamber experiments with field campaigns allows separation of instrumental effects from source-driven variability and provides a comprehensive framework for interpreting aerosol optical behavior.

The methodological strategy follows a hierarchical approach. First, the performance of the aerosol dilution system was evaluated under control conditions using synthetic aerosols. This validation phase ensured that particle concentration and size distributions were accurately preserved after dilution. Second, controlled combustion experiments were conducted inside the Atmospheric Simulation Chamber (ChAMBRe) to investigate fuel-dependent aerosol optical properties under stable environmental conditions. Finally, ambient $PM_{2.5}$ sampling was performed at two independent field locations, where real-time optical measurements were coupled with filter-based chemical analysis.

All measurements were conducted using calibrated flow systems, synchronized time resolution, and standardized data processing procedures to ensure internal consistency between experimental environments.

3.2: Experimental Setup at ChAMBRe:

The following figure 3.1 illustrates the experimental arrangement used for the real-time analysis of aerosols at ChAMBRe. A variety of instruments, including an aethalometer, total carbon analyzer, photo acoustic extinction meter, diluter, optical particle sizer, scanning mobility particle sizer, OC/EC analyzer, mass flow controllers, and pumps for mixing, exhaust, and vacuum within the chamber, are interconnected via a multiport Ethernet hub and other interfaces. Furthermore, environmental factors like temperature, humidity, and pressure are constantly monitored and regulated inside the chamber. The whole setup is controlled using a custom NI LabVIEW programming interface.

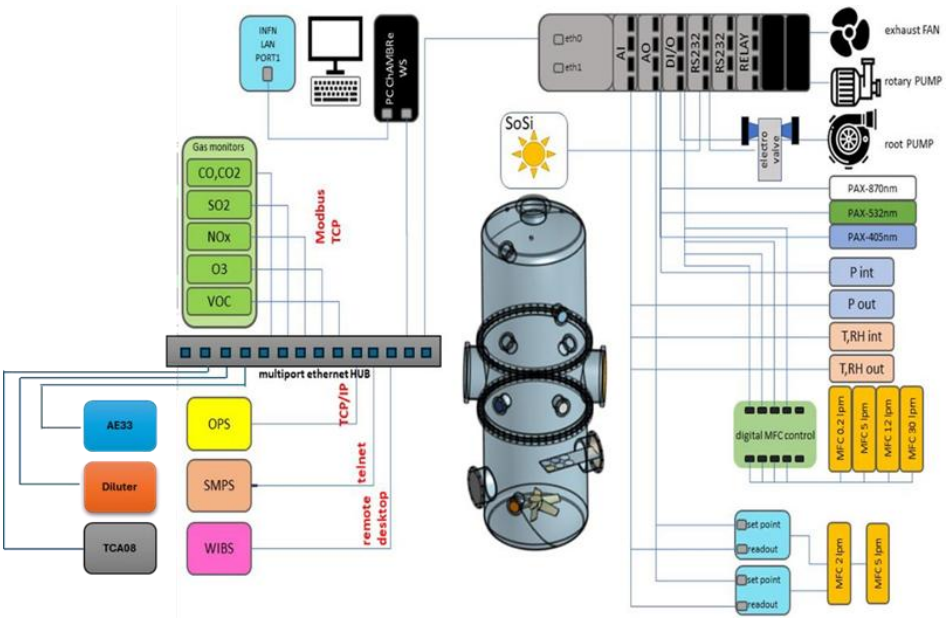

Figure 3.1: *Experimental Setup for Real time Characterization of Aerosols at ChAMBRe*

The chamber experiments were divided into two phases:

(i) validation of the dilution system and

(ii) controlled combustion optical characterization.

3.2.1 Phase I – Validation of the eDiluter Pro System

To evaluate the performance of the eDiluter Pro system, synthetic aerosols with well-defined physical properties were generated and introduced into ChAMBRe. The aerosol generation system, schematically illustrated in Figure 3.1, consisted of an ethylene-fed mini-inverter soot generator connected to calibrated mass flow controllers (MFCs). The MFCs regulated both fuel and carrier gas flow, ensuring stable aerosol production.

In addition to combustion-generated soot, non-absorbing and hygroscopic particles were produced, including polystyrene latex (PSL) spheres, sodium chloride (NaCl), and ammonium sulfate ($(NH_4)_2SO_4$). These materials were selected to represent a range of particle morphologies, refractive indices, and hygroscopic properties. The diversity of aerosol types allowed evaluation of dilution performance across different particle classes.

After generation, aerosols were injected into the chamber and allowed them to mix until a spatially homogeneous concentration was achieved. This stabilization period minimized concentration gradients and ensured representative sampling.

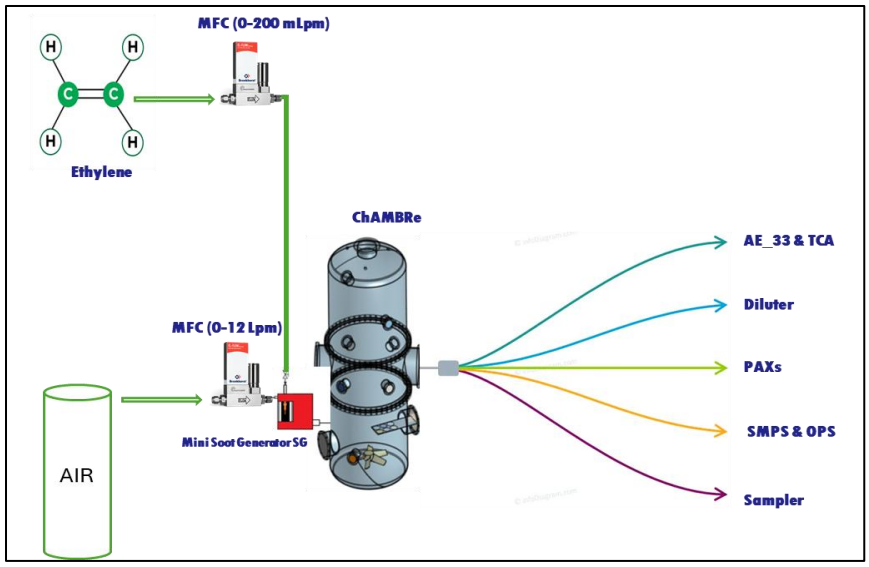

Figure 3.2: *Schematic of synthetic aerosol generation system in ChAMBRe, showing ethylene supply, mass flow controllers, mini-inverter soot generator, and instrument connections.*

3.2.2 Dilution Procedure and Calculation of Theoretical Concentration

The eDiluter Pro was operated at predefined dilution factors (DF = 25, 50, 100, 150). The theoretical concentration after dilution is defined as:

$$C_{expected} = \frac{C_0}{DF} \qquad (3.1)$$

where C_0represents the initial chamber concentration prior to dilution.

The purpose of this phase was to verify whether the measured concentration after dilution followed a linear and proportional relationship with the theoretical expectation. Particular attention was given to potential particle losses due to diffusion, inertial deposition, or sampling inefficiencies, especially at lower dilution factors.

3.2.3 Particle Size Distribution Analysis

Particle size distributions were measured using a Scanning Mobility Particle Sizer (SMPS, 1–450 nm) and an Optical Particle Sizer (OPS, 0.3–10 μm). These complementary instruments allowed full characterization of submicron and coarse-mode particles.

The total number concentration was calculated as:

$$N = \sum_i n_i \qquad (3.2)$$

where n_i denotes the particle number concentration in each size bin.

Regression analysis between measured and expected concentrations:

$$C_{measured} = m \cdot C_{expected} \qquad (3.3)$$

was used to quantify dilution accuracy. High coefficients of determination (R^2) indicated linear system response. Deviations of slope from unity reflected systematic particle losses.

Additionally, normalized particle size distributions:

$$PSD_{norm} = \frac{n_i}{\sum n_i} \qquad (3.4)$$

were evaluated to determine whether dilution altered the shape of the size distribution. The preservation of PSD shape confirmed that dilution primarily affected concentration magnitude rather than particle size characteristics.

3.3.1: Phase II – Controlled Combustion Optical Experiments

The second phase focused on investigating the optical properties of aerosols generated from controlled combustion sources. The experimental configuration is illustrated in Figure 3.3.

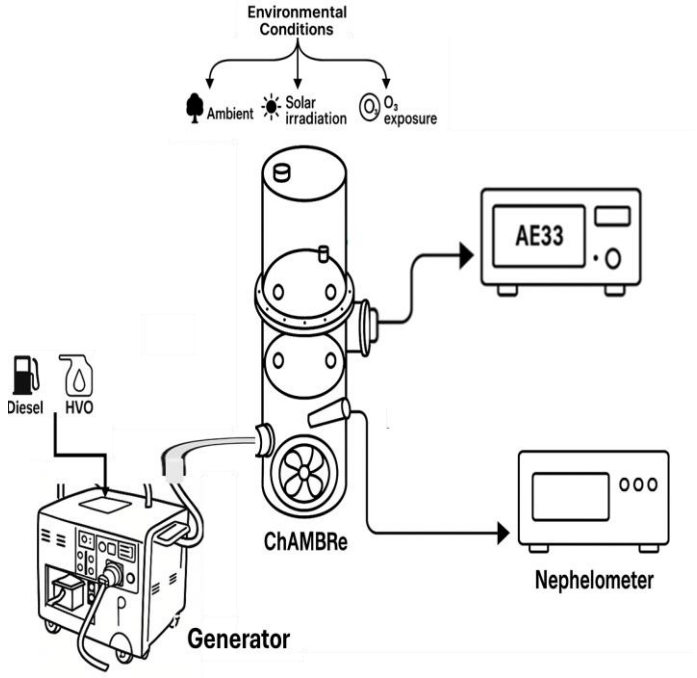

***Figure 3.3**: Schematic representation of controlled combustion experiments in ChAMBRe, including fuel combustion source, environmental control, and real-time optical measurement configuration.*

3.3.2 Combustion Sources and Experimental Configuration

Two fuel types were examined: conventional diesel and hydrotreated vegetable oil (HVO). Combustion-generated aerosols were injected into ChAMBRe under controlled flow and mixing conditions.

This controlled setup allowed investigation of intrinsic optical differences between fuels while minimizing variability from external environmental factors.

3.3.3 Environmental Regulation and Stabilization

ChAMBRe allows control of temperature and relative humidity, and when required, simulation of solar irradiation and oxidative exposure (e.g., ozone). Prior to optical measurements, sufficient stabilization time was allowed to ensure uniform mixing and steady-state aerosol concentration.

This controlled environment ensures that observed variations in optical properties are attributable to fuel type rather than meteorological fluctuations.

3.3.4 Real-Time Optical Measurements

Aerosol absorption and Scattering were measured using the Aethalometer and Nephelometer, which operate on the principle of light attenuation through a particle-loaded filter:

$$ATN = 100\ln\left(\frac{I_0}{I}\right) \tag{3.5}$$

The absorption coefficient is derived as:

$$\sigma_{abs} = \frac{A}{Q\Delta t} \cdot \frac{\Delta ATN}{C} \tag{3.6}$$

where A is the filter spot area, Q the flow rate, and C the multiple scattering correction factor.

3.3.5 Derived Optical Parameters

Simultaneous absorption and scattering measurements allowed calculation of extinction:

$$\sigma_{ext} = \sigma_{abs} + \sigma_{sca} \tag{3.7}$$

Single Scattering Albedo:

$$SSA = \frac{\sigma_{sca}}{\sigma_{ext}} \tag{3.8}$$

Absorption Ångström Exponent:

$$AAE = -\frac{\ln\left(\sigma_{abs}(\lambda_1)/\sigma_{abs}(\lambda_2)\right)}{\ln\left(\lambda_1/\lambda_2\right)} \tag{3.9}$$

These parameters provide insight into the radiative behavior and spectral dependence of combustion-generated aerosols.

3.4 Field Campaign – Site 1: Lahore, Pakistan

Ambient $PM_{2.5}$ sampling at the first field site was conducted at the rooftop of the Institute of Energy and Environmental Engineering (IEE), University of the Punjab, Lahore, Pakistan (31.4953° N, 74.2950° E). The sampling platform is located approximately 10 meters above ground level, reducing the influence of direct resuspension while remaining representative of the urban atmospheric boundary layer. The site is situated within a densely populated urban environment characterized by multiple emission sources, including major highway networks, residential neighborhoods, commercial markets, and nearby healthcare facilities. The surrounding infrastructure generates a complex mixture of vehicular emissions, small-scale industrial activity, biomass combustion, and secondary aerosol formation processes. Owing to this mixed urban influence, the site can be considered representative of urban air quality in Lahore.

$PM_{2.5}$ sampling was performed using a Sharp Cut Cyclone (SCC) inlet (MetOne Instruments, USA) operating at a calibrated flow rate of 16.67 LPM. The sharp-cut cyclone ensures aerodynamic separation with a nominal 50% cut-off diameter of 2.5 µm. The aerodynamic diameter $d_a$governing particle separation is defined as $d_a = d_p\sqrt{\frac{\rho_p \chi}{\rho_0}}$, where $d_p$is the physical diameter, $\rho_p$the particle density, $\chi$the dynamic shape factor, and $\rho_0 = 1\ \mathrm{g\ cm^{-3}}$. Maintaining the nominal flow rate is critical to preserve the cut-off efficiency and ensure consistent $PM_{2.5}$ size selection. The flow rate was continuously monitored during sampling, and manual verification was conducted periodically to confirm stability.

The target sampling duration was 24 hours; however, the effective sampling period was set to 23 hours to accommodate operational procedures such as cleaning and drying of the cyclone and filter holders, leak checks, and installation and removal of filters. The total sampled air volume was calculated as $V = Q \times t$, corresponding to approximately 23 m^3 for a 23-hour sampling period at 16.67 LPM. This sampling volume ensured adequate particulate mass loading for subsequent gravimetric and Optical/Chemical analysis while minimizing the risk of filter overloading under high pollution episodes.

$PM_{2.5}$ was collected on pre-conditioned quartz fiber filters. To ensure accurate gravimetric determination of particulate mass, filters were conditioned for at least 48 h under controlled laboratory conditions (20 ± 1 °C and 50 ± 5% RH) before weighing. Pre-sampling and post-sampling filter masses were determined using a Sartorius MC5 microbalance. After sample collection, filters were reconditioned under identical environmental conditions prior to final weighing. $PM_{2.5}$ mass concentration was calculated as: as $C_{PM_{2.5}} = (m_{post} - m_{pre})/V$, where m_{pre} and m_{post} represent the pre- and post-sampling filter masses, respectively. Field blanks were included to account for handling artefacts and background contamination.

3.5 Field Campaign – Site 2: Multedo, Genoa (Italy)

Ambient $PM_{2.5}$ measurements at the second field site were conducted in the Multedo district of Genoa, Italy, at a roadside monitoring location directly exposed to vehicular traffic emissions and influenced by nearby port activities. The sampling station is situated at near-ground level along a roadway in a coastal urban environment. The site is characterized by a combination of emission sources including light-duty and heavy-duty vehicular traffic, maritime shipping activities associated with the Port of Genoa, urban residential emissions, and localized industrial contributions. The experimental setup (Figure: 3.3) along roadside positioning at ARPAL monitoring station allow us for characterization of near-source combustion aerosols prior to extensive atmospheric dilution and aging, making the site particularly suitable for investigating absorption-dominated $PM_{2.5}$ and traffic-influenced optical properties.

Figure 3.4: *Experimental setup at the Multedo site (Genoa).*

$PM_{2.5}$ sampling was performed using independent sharp-cut cyclone inlets connected to three parallel measurement systems: a CASS instrument for absorption measurements operating at 5 LPM, an integrating nephelometer for scattering measurements also operating at 5 LPM, and a sequential filter sampler operating at 38.3 LPM for gravimetric and chemical analysis. The use of independent inlets ensured that flow conditions were not shared among instruments, thereby minimizing cross-interference and preserving aerodynamic cut-off characteristics. The $PM_{2.5}$ size selection was achieved through cyclonic separation with a nominal 50% cut-off diameter of 2.5 μm. Flow rates were calibrated prior to deployment and verified periodically to ensure consistency of the size-selective separation.

Real-time optical measurements were conducted simultaneously to quantify aerosol absorption and scattering properties under identical ambient conditions. The absorption coefficient (σ_{abs}) was derived from attenuation measurements obtained by the CASS system, which quantifies light attenuation across a particle-loaded filter. The absorption coefficient was calculated using standard attenuation-based formulations incorporating spot area, sampling flow rate, time resolution, and multiple-scattering correction factors. The integrating nephelometer measured the total scattering coefficient (σ_{sca}) by

integrating scattered light intensity over a defined angular range, with truncation corrections applied to compensate for incomplete angular detection. The parallel measurement configuration enabled direct calculation of the extinction coefficient ($\sigma_{ext} = \sigma_{abs} + \sigma_{sca}$) and the single scattering albedo ($SSA = \sigma_{sca}/\sigma_{ext}$), thereby allowing assessment of the relative contribution of absorption versus scattering in a traffic-influenced environment. Given the roadside setting, elevated absorption coefficients and comparatively lower SSA values were expected due to the strong influence of freshly emitted black carbon from vehicular sources.

Filter-based $PM_{2.5}$ sampling was performed using a sequential sampler operating at 38.3 LPM with a nominal sampling duration of approximately 24 hours per filter. The effective sampling duration was selected to balance operational requirements with daily averaging consistency. The total sampled air volume was determined as $V = Q \times t$, corresponding to approximately 55 m^3 for a 24-hour sampling period. Quartz filters were conditioned before and after sampling under controlled laboratory temperature and relative humidity to minimize hygroscopic artefacts prior to gravimetric determination. $PM_{2.5}$ mass concentration was calculated as $C_{PM_{2.5}} = (m_{post} - m_{pre})/V$, where m_{pre} and m_{post} represent pre- and post-sampling filter masses, respectively. Field blanks were included to be correct for handling and transport-related contamination.

Meteorological parameters, including ambient temperature and relative humidity, were recorded throughout the sampling period. The roadside location is subject to rapid fluctuations in boundary layer conditions, traffic-induced turbulence, and coastal wind influences, all of which may impact aerosol dispersion, hygroscopic growth, and optical properties. The availability of concurrent meteorological data supports interpretation of observed temporal variability in absorption, scattering, and derived intensive optical parameters.

Quality assurance procedures included pre- and post-deployment flow calibration, routine leak checks, instrument zero verification, and standardized filter handling protocols.

CHAPTER 4: Results and Discussion

4.1 Overview of Experimental Conditions

This chapter presents the results obtained from complementary field and laboratory investigations aimed at characterizing aerosol optical and chemical properties under different environmental conditions. The analyses integrate real-time measurements with offline filter-based observations to explore the relationships between aerosol composition, light absorption, and scattering behavior.

The results are derived from three experimental datasets:

(i) continuous atmospheric observations at the Multedo site in Genoa (Italy);

(ii) a field campaign conducted in Lahore (Pakistan); and

(iii) controlled laboratory experiments performed in the ChAMBRe facility.

These datasets provide complementary perspectives on aerosol behavior, ranging from real-world atmospheric observations to controlled investigations of specific aerosol processes.

Field measurements at the Multedo site were performed in a coastal urban environment influenced by traffic emissions, industrial activities, and marine aerosol contributions. Continuous measurements of aerosol optical properties were conducted using an AE33 Aethalometer and an Aurora 4000 integrating nephelometer, while filter samples were collected for subsequent offline analyses.

The Lahore campaign was conducted in a highly polluted urban environment characterized by elevated particulate matter concentrations and diverse anthropogenic emission sources. The campaign provides an exploratory comparison between two urban environments exhibiting different emission regimes and atmospheric conditions.

Controlled experiments in the ChAMBRe facility were designed to investigate aerosol optical properties under well-defined and reproducible conditions. Synthetic aerosols, including polystyrene latex (PSL) particles, sodium chloride (NaCl), ammonium sulfate

($(NH_4)_2SO_4$), and soot, were employed to evaluate instrument performance and to examine aerosol behavior under controlled conditions.

The following datasets are used throughout this chapter:

• aerosol absorption coefficients and equivalent black carbon concentrations derived from AE33 measurements;

• aerosol scattering coefficients obtained from nephelometer observations;

• spectral absorption properties determined using MWAA and BLAnCA analyses;

• carbonaceous aerosol fractions (OC and EC) derived from TCA08 and Sunset OC/EC analyses.

Together, these datasets provide a comprehensive basis for investigating the optical and chemical characteristics of atmospheric aerosols and their interrelationships.

4.2: Validation Study for eDiluter Pro at ChAMBRe:

The performance of the Dekati eDiluter Pro was evaluated under controlled laboratory conditions at ChAMBRe prior to its application in aerosol characterization experiments. The objective was to assess the accuracy of the dilution system over a range of dilution factors (DF = 25–225) by comparing experimentally measured particle concentrations and size distributions with theoretical values.

Validation experiments were conducted using polystyrene latex (PSL), sodium chloride (NaCl), ammonium sulfate ($(NH_4)_2SO_4$), and soot particles, representing aerosols with different physical and chemical properties. A schematic overview of the validation procedure is shown in Figure 4.1. The results presented in the following sections provide a quantitative assessment of dilution-system performance.

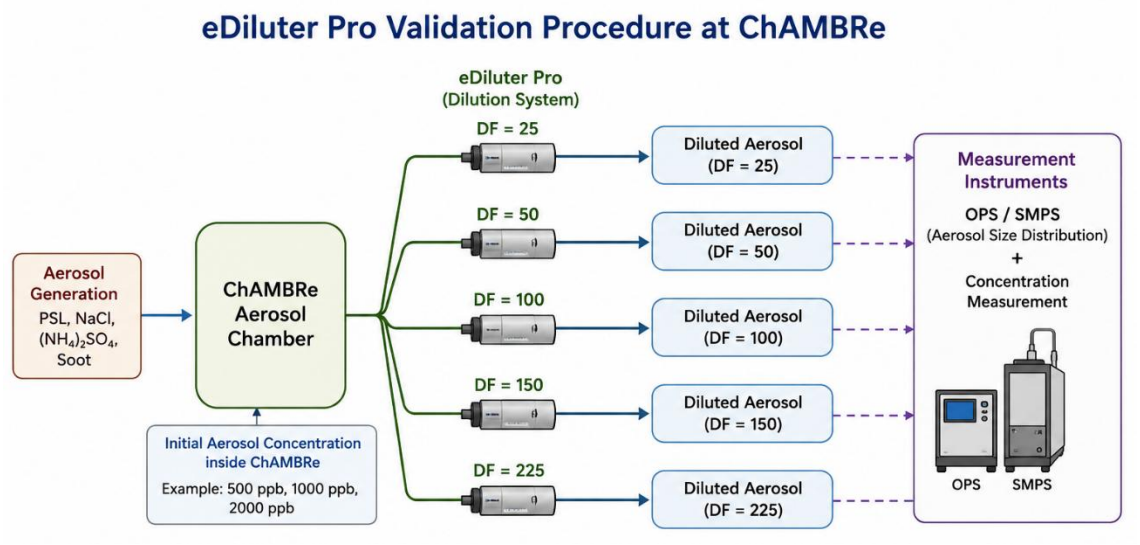

Figure 4.1. *Schematic of the eDiluter Pro validation procedure at ChAMBRe.*

4.2.1: Effect of Dilution Factors on PSD and Concentration of PSL Particles by Using OPS

Graph (a1 – a4):

Figure 4.2 (a1–a4) compares the expected and experimentally measured particle size distributions (PSDs) of PSL particles obtained using the OPS at dilution factors of 25, 50, 100, and 150. The comparison was performed to evaluate the ability of the eDiluter Pro system to preserve particle concentration and size distribution after dilution. Agreement between the expected and measured PSDs was used as an indicator of dilution-system performance.

Graph (a-1):

DF = 150 (Figure 4.2a1). The OPS measurements reproduced the overall shape of the PSL particle size distribution; however, the measured concentrations were consistently lower than the expected values across the dominant size ranges. The largest discrepancies were observed near the principal PSD peaks, where concentration underestimation became more pronounced. This behavior suggests particle losses associated with the high dilution factor, resulting in reduced concentration recovery while largely preserving the

general PSD profile. The results indicate that DF = 150 introduces significant underestimation of particle concentrations and therefore represents the least accurate dilution condition among those investigated.

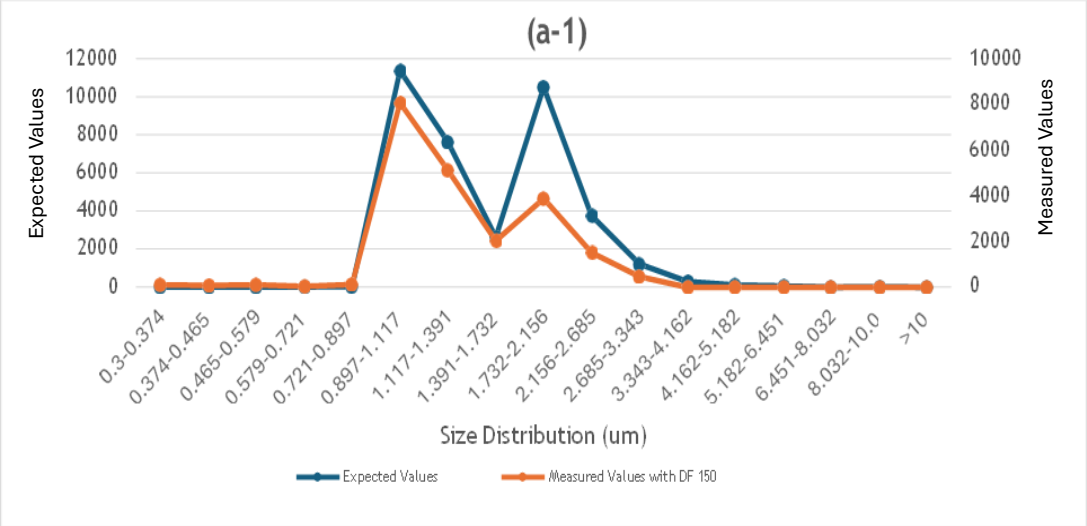

Figure 4.2: *Effect of DF 150 on PSD of PSL Particles by OPS*

Graph (a-2):

DF = 100 (Figure 4.3a2). The measured PSD generally reproduced the main features of the expected distribution, although concentration differences were observed across several size bins. The largest discrepancies occurred near the dominant PSD maxima, where measured concentrations remained lower than the corresponding expected values. Nevertheless, the agreement between expected and measured distributions was improved compared with DF = 150, indicating reduced dilution-related particle losses. The overall PSD shape was preserved, suggesting that DF = 100 provides more reliable concentration recovery while maintaining the characteristic size distribution of PSL particles.

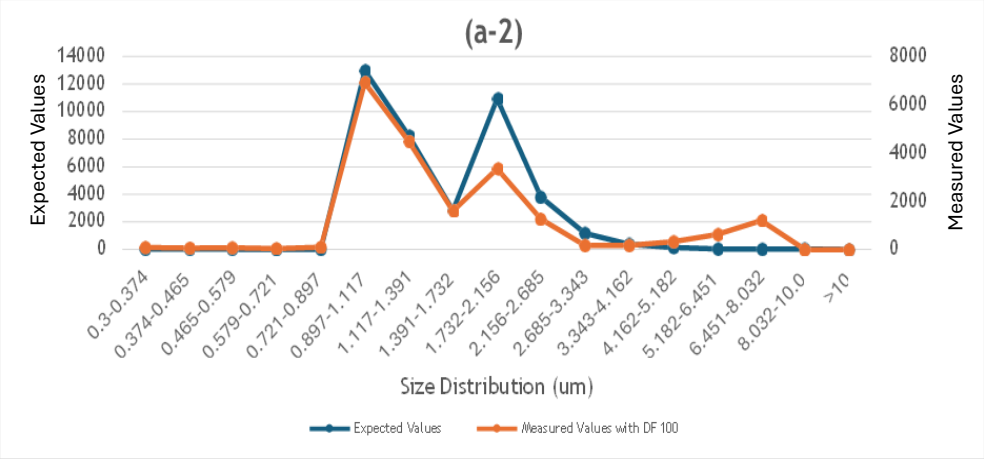

Figure 4.3: *Effect of DF 100 on PSD of PSL Particles by OPS*

Graph (a-3):

DF = 50 (Figure 4.4a3). The measured PSD closely reproduced the main features of the expected distribution, including the two dominant concentration modes. Although differences remained in the magnitude of the concentration peaks, the overall distribution pattern was well preserved across the investigated size range. The improved correspondence between expected and measured concentrations indicates that dilution-related artefacts were substantially reduced at DF = 50, allowing reliable characterization of PSL particle size distributions by the OPS.

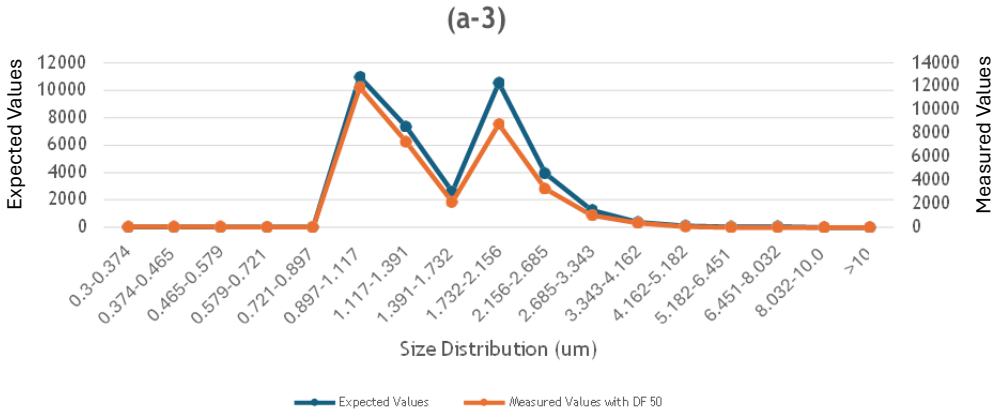

Figure 4.4: *Effect of DF 50 on PSD of PSL Particles by OPS*

Graph (a-4):

DF = 25 (Figure 4.5a4). Among the investigated dilution factors, DF = 25 exhibited the closest agreement between the expected and measured PSL particle size distributions. The principal features of the PSD were well reproduced across the investigated size range, indicating effective preservation of particle-size information during dilution. Although discrepancies remained in selected size bins, particularly around the second concentration maximum, the overall correspondence between the expected and measured distributions was superior to that observed at higher dilution factors. These results suggest that DF = 25 provided the most reliable representation of the original PSL aerosol distribution under the experimental conditions employed.

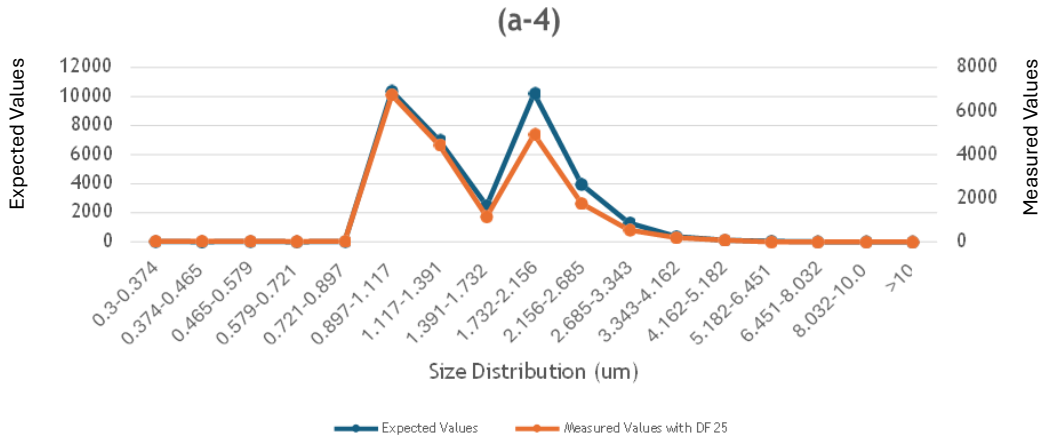

Figure 4.5: *Effect of DF 25 on PSD of PSL Particles by OPS*

Graph (b):

Figure 4.6 summarizes the relationship between expected and measured PSL particle concentrations obtained at different dilution factors. As expected, particle concentrations decreased with increasing dilution factor. Measured concentration remained consistently lower than the corresponding expected values, indicating the presence of dilution-related particle losses across all operating conditions. Although the absolute difference between expected and measured concentrations decreased at higher dilution factors, the relative agreement did not show a clear monotonic improvement. Therefore, dilution performance

should be evaluated based on concentration recovery rather than absolute concentration differences alone. Overall, the results indicate that the eDiluter Pro preserved the general concentration trend across the investigated dilution range, while maintaining acceptable agreement between expected and measured values.

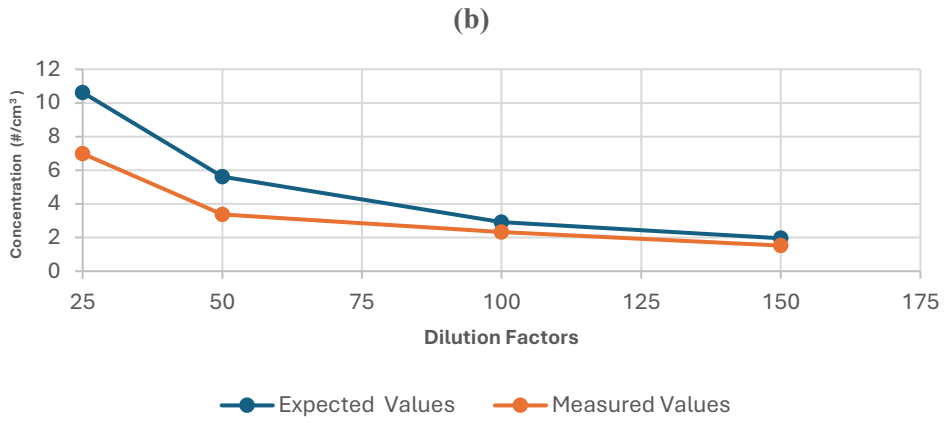

Figure 4.6: *Comparison of expected and measured PSL particle concentrations obtained using OPS at different dilution factors (DF = 25–150).*

Graph (c):

Figure 4.7 presents the correlation between expected and measured PSL particle concentrations obtained using OPS for all investigated dilution factors. A strong linear relationship was observed between the two datasets (R^2 = 0.9952), indicating that the dilution system preserved the overall concentration trend across the investigated range. The regression slope of 0.6565 shows that measured concentrations were systematically lower than the corresponding expected values, reflecting an average concentration recovery of approximately 66%. While some variability was observed among individual dilution factors, no clear monotonic dependence of recovery on dilution factor was evident from the correlation analysis. Overall, the results demonstrate a consistent and reproducible response of the dilution system, despite the presence of systematic concentration underestimation.

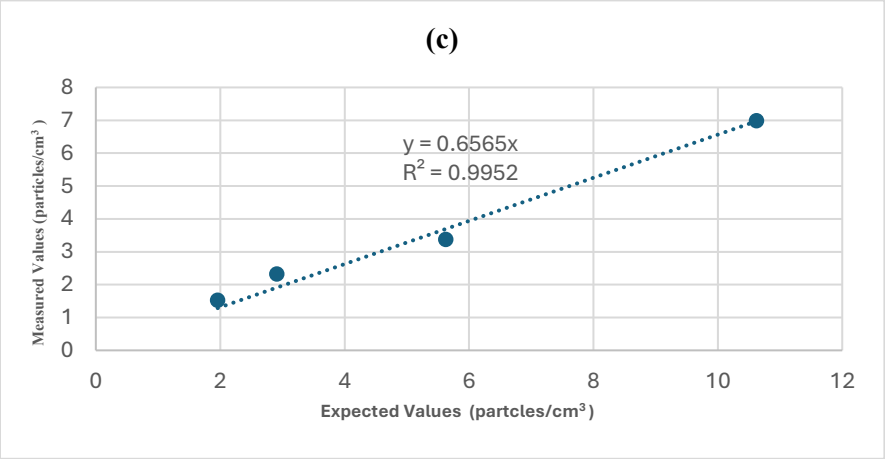

Figure 4.7: *Correlation Between Expected and Measured Values of PSL Particles by OPS*

4.2.2: Effect of Dilution Factors on PSD and Concentration of NaCl Particles by Using OPS

Figure 4.8 (a1–a4) compares the expected and measured particle size distributions (PSDs) of NaCl particles obtained using OPS at dilution factors of 25, 50, 100, and 150. NaCl particles were selected as a representative hygroscopic aerosol to evaluate the ability of the eDiluter Pro to preserve particle concentration and size-distribution characteristics after dilution. The agreement between expected and measured PSDs was used to assess dilution performance and identify potential concentration losses associated with different dilution factors.

Graph (a-1):

DF = 150 (Figure 4.8a1). The measured PSD generally followed the decreasing trend observed in the expected NaCl distribution, indicating that the overall particle-size pattern was preserved after dilution. However, noticeable differences remained in the dominant concentration bins, where measured concentrations were consistently lower than the expected values. These deviations suggest the presence of dilution-related particle losses, although the characteristic shape of the NaCl PSD remained largely unchanged.

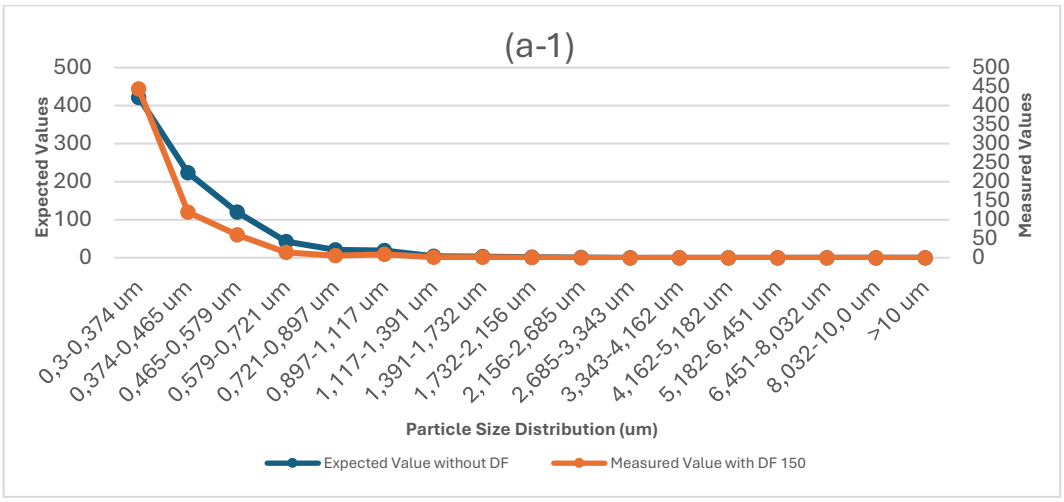

Figure 4.8: *Effect of Dilution Factor (150) on PSD of NaCl Particles by OPS*

Graph (a-2):

DF = 100 (Figure 4.9a2). The measured PSD reproduced the overall decreasing trend of the expected NaCl distribution, although lower concentrations were observed across most size bins. The largest deviations occurred within the dominant particle-size fractions, indicating the presence of dilution-related losses. Nevertheless, the general shape of the PSD remained preserved, suggesting that the dilution process did not substantially alter the size-distribution characteristics of NaCl particles. A quantitative comparison of dilution performance is presented in the subsequent concentration and correlation analyses.

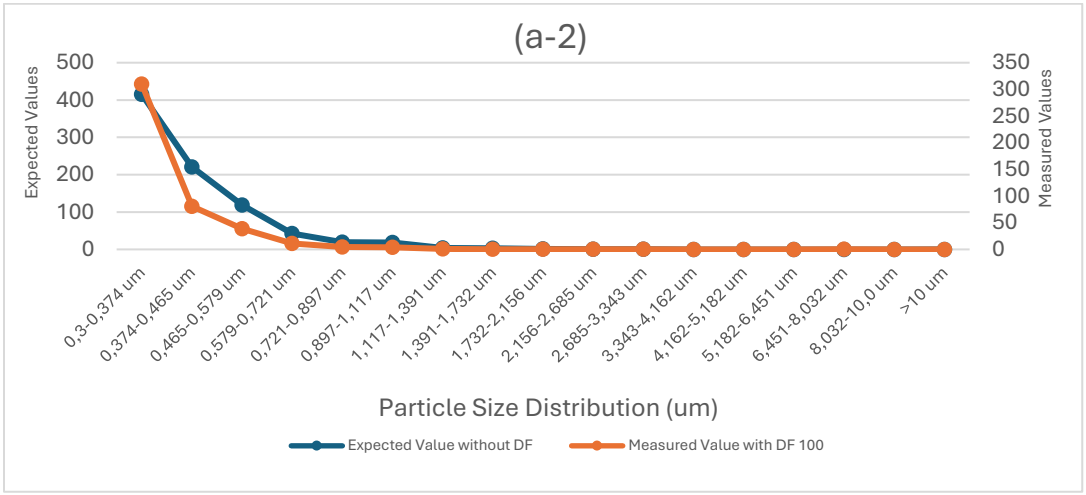

Figure 4.9: *Effect of Dilution Factor (100) on PSD of NaCl Particles by OPS*

Graph (a-3):

DF = 50 (Figure 4.10a3). The measured NaCl PSD continued to reproduce the overall decreasing trend of the expected distribution, although concentration differences became more pronounced across the dominant particle-size fractions. The deviation between expected and measured values was greater than that observed at DF = 100, indicating reduced concentration recovery under this dilution condition. Despite these differences, the characteristic PSD shape remained preserved, suggesting that dilution primarily affected particle concentration rather than the overall size-distribution pattern.

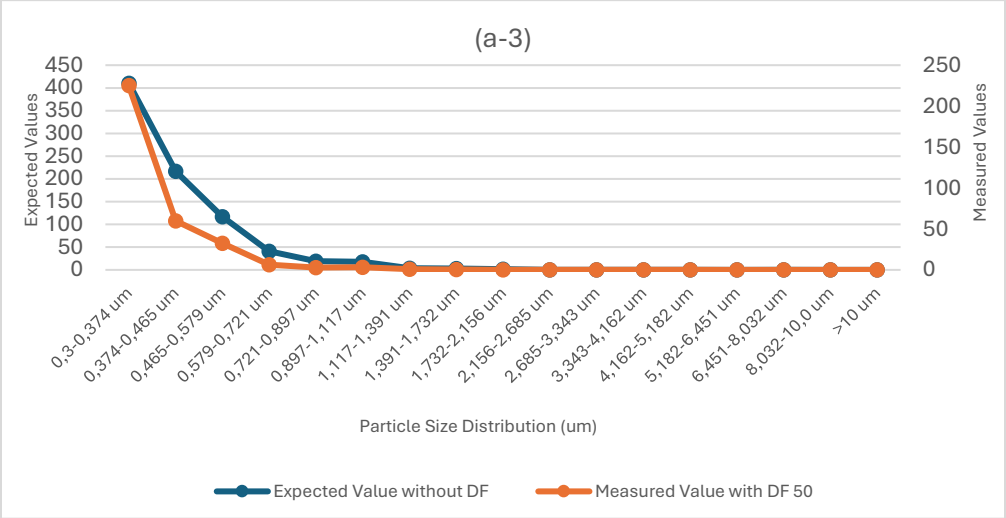

Figure 4.10: *Effect of Dilution Factor (50) on PSD of NaCl Particles by OPS*

Graph (a-4):

DF = 25 (Figure 4.11a4). The measured NaCl PSD showed a distribution pattern similar to that observed at DF = 50, with the overall shape of the expected distribution remaining preserved after dilution. Differences between expected and measured concentrations were observed primarily within the dominant particle-size fractions, while the remaining size bins exhibited comparable trends. The similarity between the DF = 25 and DF = 50 distributions suggests that dilution performance remained relatively consistent across

these lower dilution factors, although some concentration underestimation was still evident.

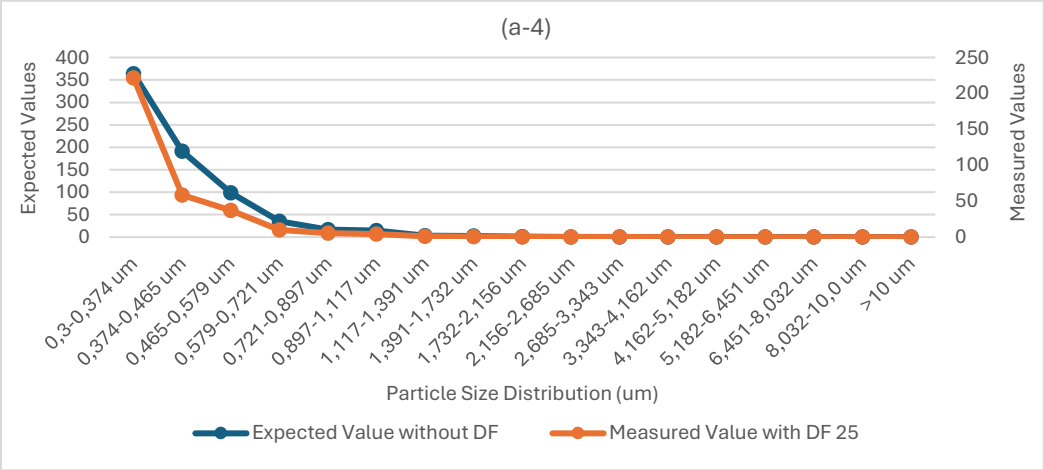

Figure 4.11: *Effect of Dilution Factor (25) on PSD of NaCl Particles by OPS*

Graph (b):

Figure 4.12 summarizes the relationship between expected and measured NaCl particle concentrations obtained at different dilution factors. As expected, particle concentrations decreased with increasing dilution factor. Measured concentrations remained consistently lower than the corresponding expected values, indicating concentration underestimation across the investigated dilution range. The difference between expected and measured concentrations was more pronounced at lower dilution factors, whereas both datasets converged as particle concentrations decreased. However, the apparent reduction in the absolute difference at higher dilution factors does not necessarily imply improved dilution performance, since concentration recovery should be evaluated on a relative basis. Overall, the results indicate a systematic underestimation of NaCl particle concentrations while preserving the expected concentration trend across all dilution factors.

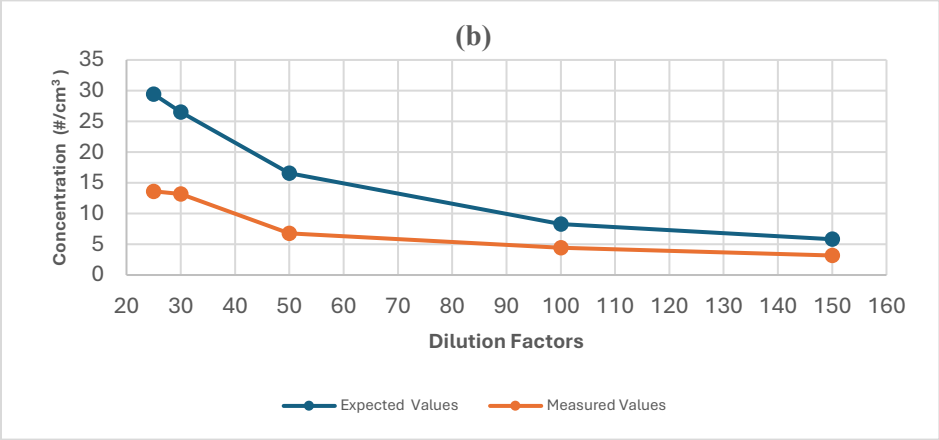

Figure 4.12: *Effect of Dilution Factors(150, 100, 50 & 25) on NaCl Particles Concentration by OPS*

Graph (c):

Figure 4.13 presents the relationship between expected and measured NaCl particle concentrations obtained at different dilution factors. A strong linear relationship was observed between the two datasets, as indicated by the high coefficient of determination ($R^2 = 0.9951$). The regression slope of 0.472 indicates that the measured concentrations were, on average, approximately 47% of the expected values, reflecting a systematic underestimation across the investigated dilution range. Despite this bias, the high R^2 value demonstrates that the dilution process preserved a consistent proportional relationship between expected and measured concentrations. These results suggest that the eDiluter Pro maintained reproducible dilution behaviour for NaCl aerosols over the tested concentration range.

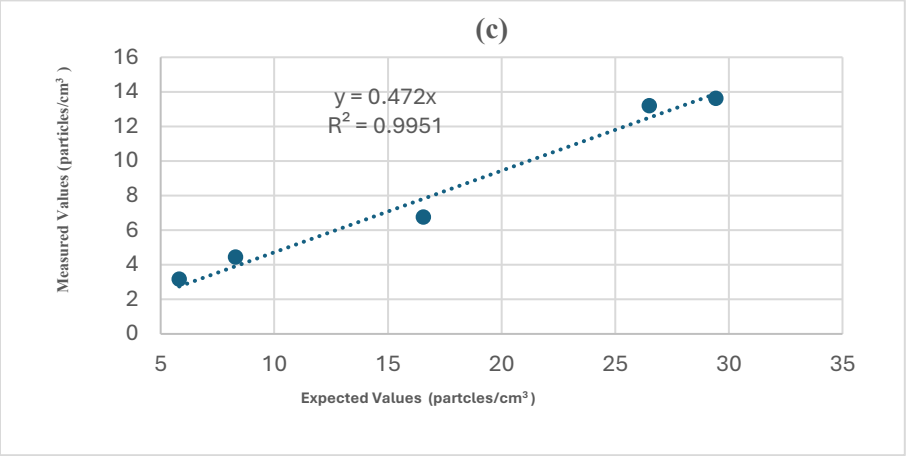

Figure 4.13: *Correlation Between Expected and Measured Values of NaCl Particles by OPS*

4.2.3: Effect of Dilution Factors on PSD (Particle Size Distribution) and Concentration of Ammonium Sulfate Particles by Using OPS

Graphs (a1 – a4):

Figures 4.14–4.17 compare the expected and measured particle size distributions (PSD) of ammonium sulfate aerosols obtained using OPS at four dilution factors (DF 150, DF 100, DF 50, and DF 25). The expected distribution corresponds to the reference concentration before dilution, whereas the measured distribution represents the concentration after dilution. The objective is to evaluate how dilution affects particle concentration and whether the original PSD shape is preserved across different dilution factors.

Graph (a-1):

The expected and measured PSDs show a similar overall distribution, with the highest concentrations observed in the smaller particle size bins. At DF 150, the measured values generally follow the expected trend, indicating that the original PSD shape is largely preserved after dilution. Some deviations are observed in the 0.465–0.579 µm size range, where the measured concentrations are lower than the expected values. For larger particle sizes, both distributions decrease rapidly and approach near-zero concentrations.

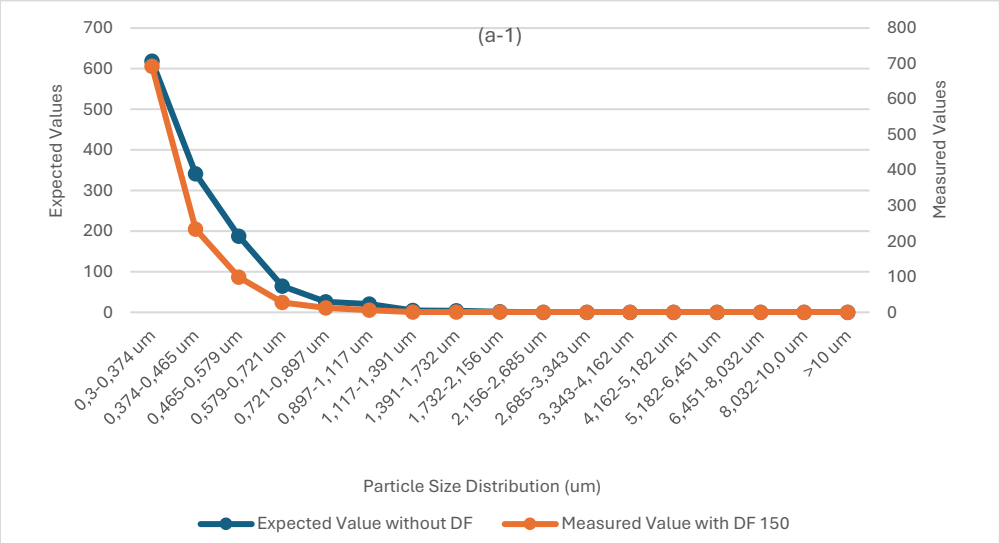

Figure 4.14: *Effect of Dilution Factor (150) on PSD of Ammonium Sulfate Particles by OPS*

Graph (a-2):

The expected and measured PSDs exhibit a similar overall distribution, with the highest concentrations observed in the smaller particle size bins. At DF 100, the measured values generally follow the expected trend, indicating that the PSD shape is largely maintained after dilution. Compared with DF 150, slightly larger deviations are observed in the size range below 0.579 µm, where measured concentrations are lower than the expected values. For larger particle sizes, both distributions decrease rapidly and remain close to zero.

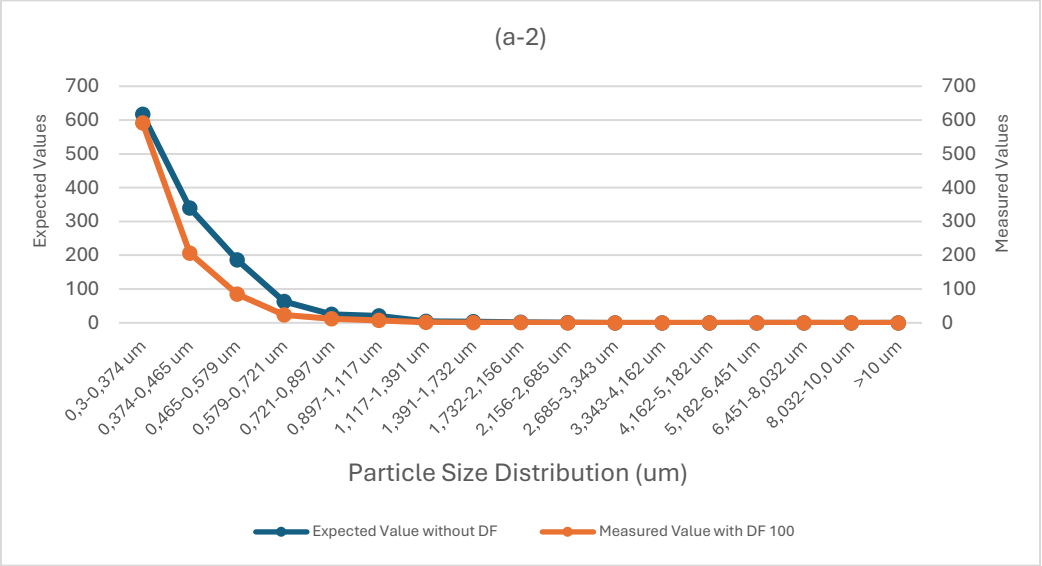

Figure 4.15: *Effect of Dilution Factor (100) on PSD of Ammonium Sulfate Particles by OPS*

Graph (a-3):

The expected and measured PSDs maintain a similar overall shape, with the highest concentrations observed in the smaller particle size bins. At DF 50, the measured concentrations are generally lower than the expected values, particularly below 0.579 µm. The difference between the two distributions becomes more evident than in DF 100 and DF 150, although the overall PSD pattern remains preserved. For particle sizes above approximately 0.72 µm, both distributions decrease rapidly and approach near-zero concentrations.

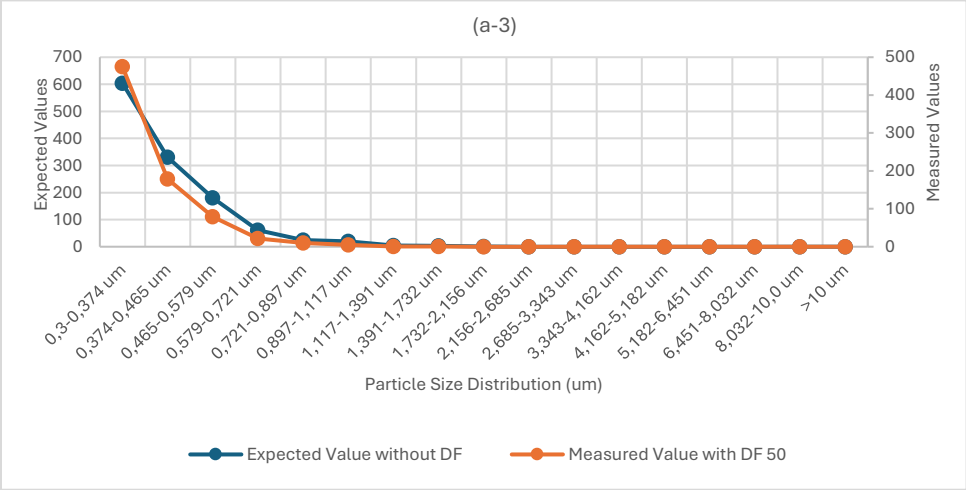

Figure 4.16: *Effect of Dilution Factor (50) on PSD of Ammonium Sulfate Particles by OPS*

Graph (a-4):

The expected and measured PSDs exhibit a similar overall distribution, with the highest concentrations observed in the smaller particle size bins. At DF 25, the measured concentrations are consistently lower than the expected values across most size ranges. The difference between expected and measured distributions is more pronounced than in the higher dilution factors, particularly below 0.579 µm. Despite these deviations, the overall PSD shape remains recognizable, and both distributions decrease rapidly with increasing particle size.

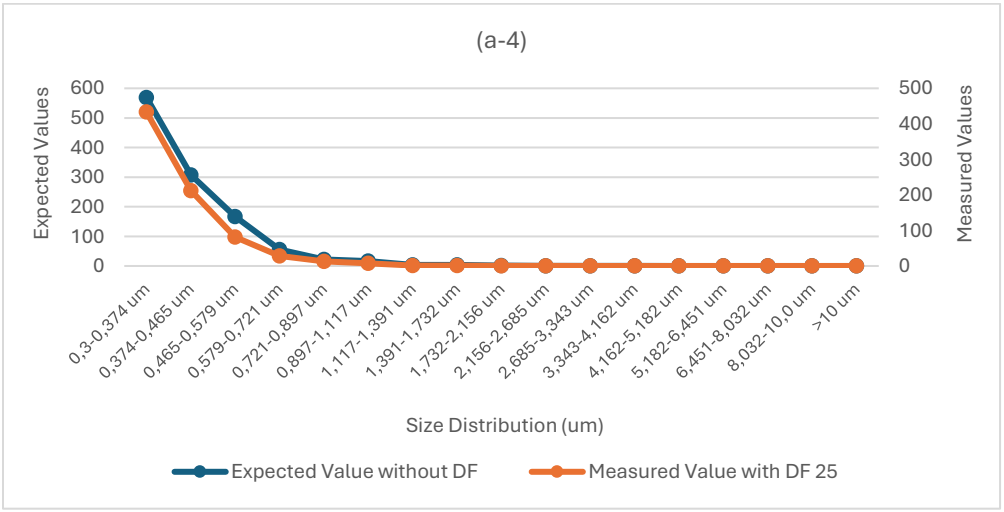

Figure 4.17: *Effect of Dilution Factor (25) on PSD of Ammonium Sulfate Particles by OPS*

Graph (b):

Figure 4.18 compares the expected and measured ammonium sulfate particle concentrations at different dilution factors. Both concentrations decrease with increasing dilution factors. Measured values remain lower than the corresponding expected values across the entire dilution range, while following the same overall trend. The difference between expected and measured concentrations is larger at lower dilution factors and becomes smaller as the dilution factor increases, indicating a more consistent agreement between the two datasets at higher dilution factors.

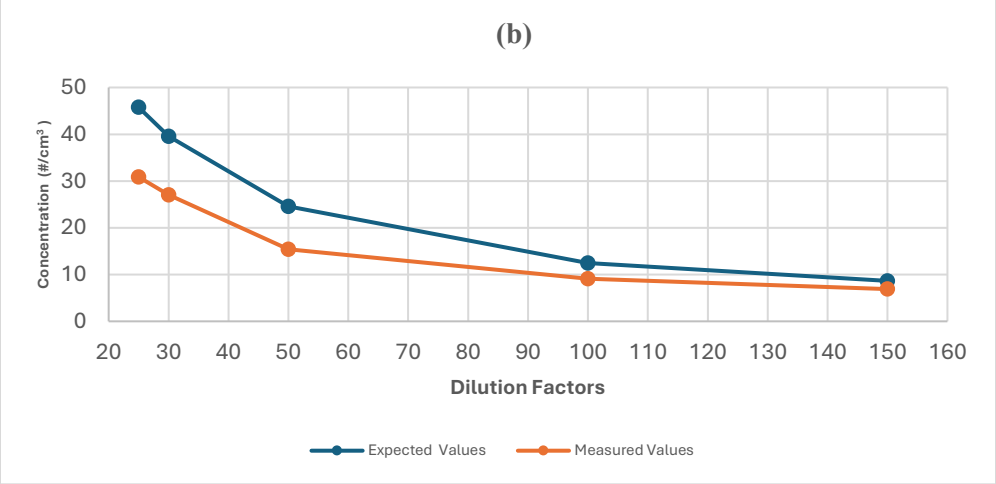

Figure 4.18: *Effect of Dilution Factors on Concentration of Ammonium Sulfate Particles by OPS*

Graph (c):

Figure 4.19 presents the correlation between expected and measured ammonium sulfate particle concentrations obtained at different dilution factors. A strong linear relationship was observed between the two datasets, as indicated by the high coefficient of determination ($R^2 = 0.9985$). The regression slope of 0.6749 indicates that the measured concentrations were, on average, approximately 67% of the expected values over the entire dataset. Although measured concentrations are systematically lower than the

expected values, the high R^2 demonstrates that the relationship between the two datasets remains highly consistent across the investigated concentration range. These results indicate that the dilution process preserves a stable proportional relationship between expected and measured concentrations.

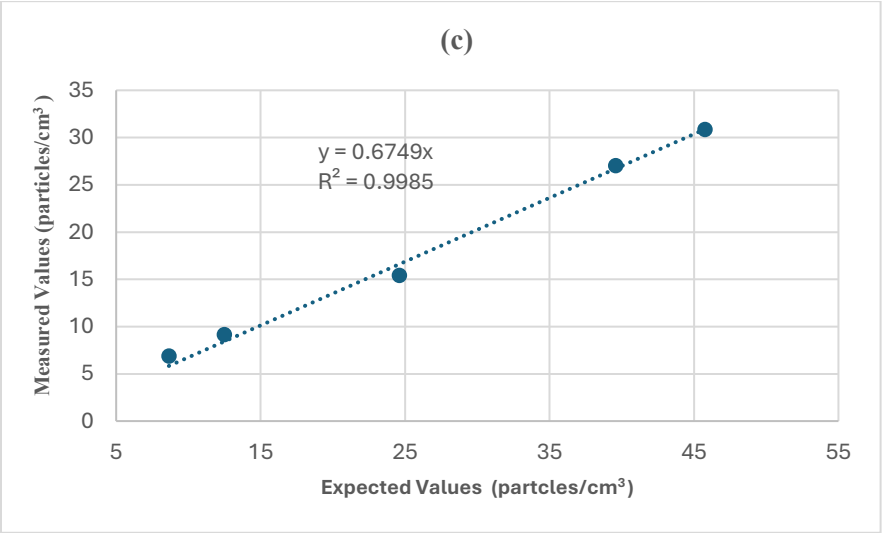

Figure 4.19: *Correlation Between Expected and Measured Values of Ammonium Sulfate Particles*

4.2.4: Effect of Dilution Factors on PSD of Soot Particles (Ethylene) by Using SMPS

This section evaluates the effect of dilution factors (DF 25, DF 50, and DF 100) on the particle size distribution (PSD) of ethylene soot measured using the SMPS. The PSD comparison plots (a-series) show the agreement between expected and measured distributions, while the correlation plots (b-series) summarize the relationship between expected and measured concentrations at each dilution factor.

Graph (a-1):

The measured PSD at DF 25 generally follows the shape of the expected distribution, with the main concentration mode observed between approximately 150 and 300 nm. The agreement between measured and expected concentrations is strongest around the peak region, while larger deviations are observed at the lowest concentration bins. The

measured concentrations remain slightly lower than the expected values across most particle sizes, indicating a systematic difference between the reference and measured distributions. Overall, the results show that the dilution system preserves the main features of the soot PSD while introducing moderate deviations in particle concentration.

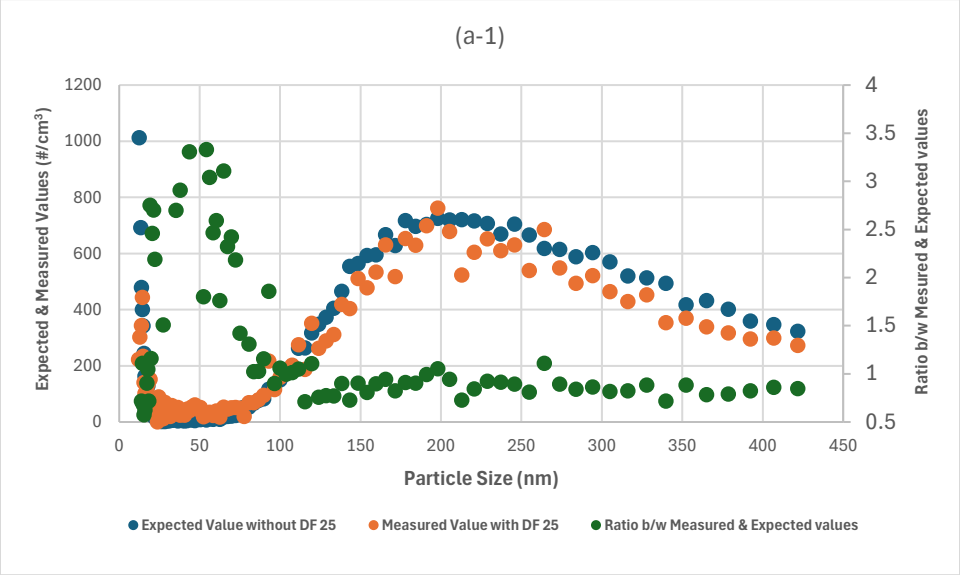

Figure 4.20: *Expected vs. Measured PSD at DF 25*

Graph (b-1):

Figure 4.21 presents the correlation between expected and measured particle concentrations at DF 25. A strong linear relationship is observed, with a regression slope of 0.8791 and an R^2 value of 0.9787. The high coefficient of determination indicates that the measured concentrations closely follow the variation of the expected values over the investigated concentration range. Although the measured concentrations are generally lower than the expected values, the strong correlation demonstrates that the dilution system preserves the overall concentration trend and provides consistent measurements across the particle size distribution.

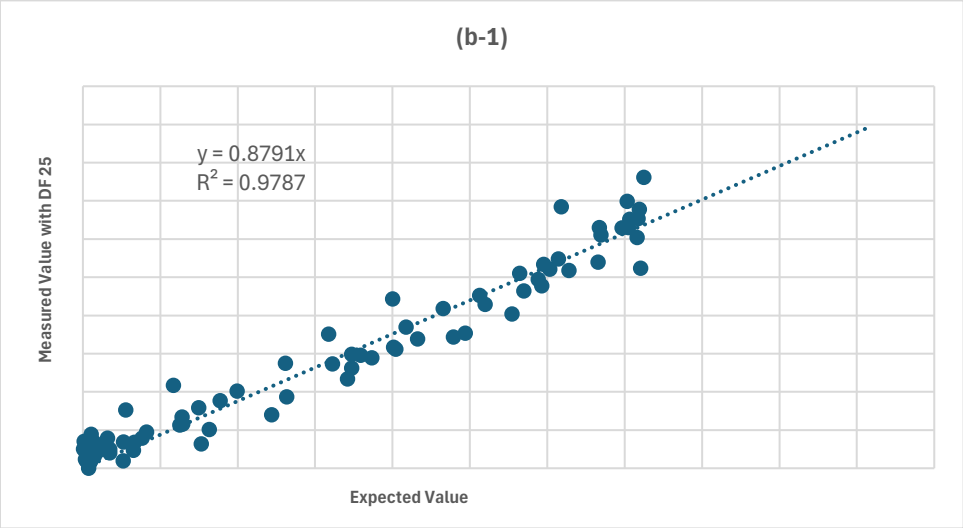

Figure 4.21: *Correlation Between Expected and Measured Values at DF 25*

Graph (a-2):

Figure 4.22 compares the expected and measured PSDs at DF 50. The measured distribution follows the overall shape of the expected PSD, with the main concentration mode observed between approximately 150 and 250 nm. Agreement between measured and expected concentrations is generally good across the dominant size range, although some differences are visible at individual particle sizes. The ratio values vary across the distribution, indicating that the degree of agreement is not uniform for all particle sizes. Overall, the results show that the main characteristics of the soot PSD are preserved after dilution at DF 50.

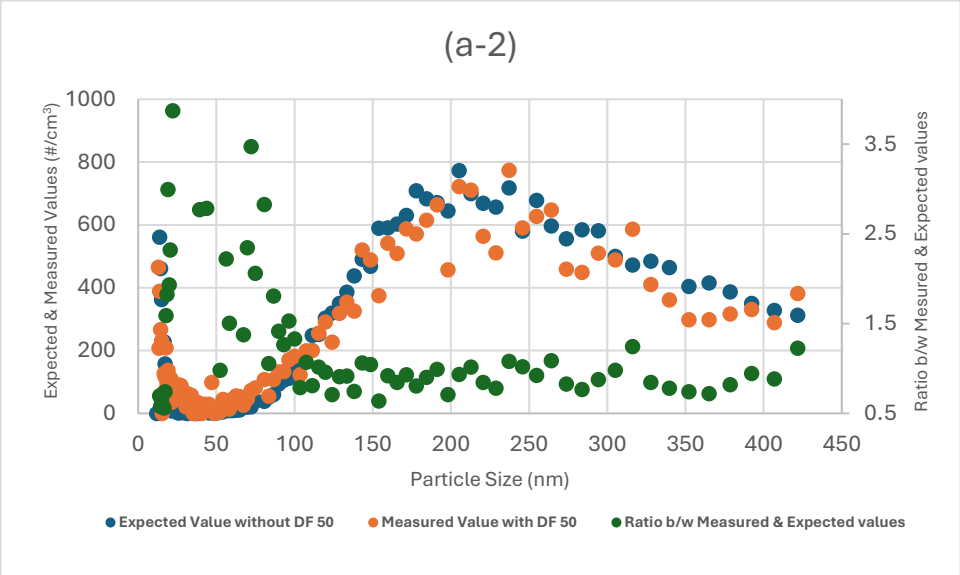

Figure 4.22: *Effect of DF (50) on PSD of Soot Particles by SMPS*

Graph (b-2):

Figure 4.23 presents the correlation between expected and measured particle concentrations at DF 50. A strong linear relationship is observed, with a regression slope of 0.8881 and an R^2 value of 0.9617. The slope indicates that the measured concentrations are generally lower than the expected values, while the high coefficient of determination demonstrates that the measured data closely follows the variation of the reference dataset. Overall, the results confirm a consistent agreement between expected and measured concentrations across the concentration range investigated at DF 50.

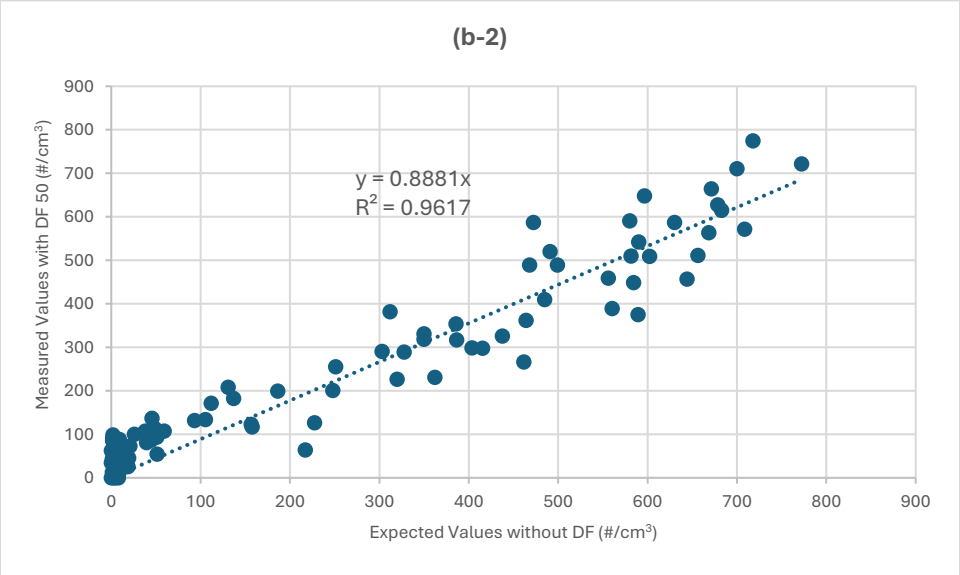

Figure 4.23: *Correlation Between Expected and Measured Values at DF 50*

Graph (a-3):

Figure 4.24 compares the expected and measured PSDs at DF 100. The measured distribution follows the overall shape of the expected PSD, with the main concentration mode observed between approximately 150 and 250 nm. Agreement between measured and expected concentrations is generally good across the dominant size range, although differences are observed at individual particle sizes. The ratio values vary across the distribution, indicating that the level of agreement is not constant for all particle sizes. Overall, the results show that the principal features of the soot PSD are preserved after dilution at DF 100.

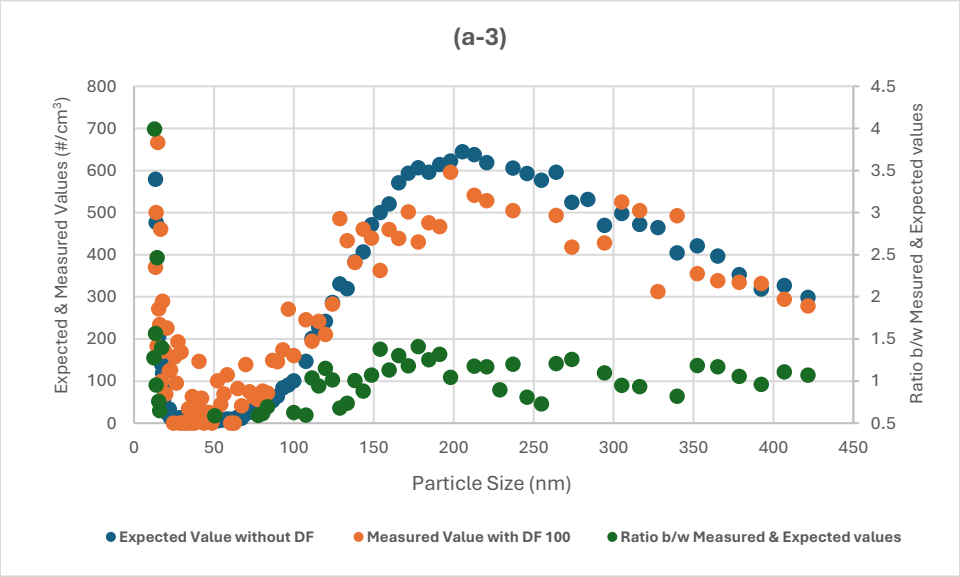

Figure 4.24: *Effect of DF (100) on PSD of Soot Particles by SMPS*

Graph (b-3):

Figure 4.25 presents the correlation between expected and measured particle concentrations at DF 100. A strong linear relationship is observed, with a regression slope of 0.9011 and an R^2 value of 0.9175. The slope indicates that measured concentrations are generally lower than the expected values, while the high coefficient of determination confirms that the measured data closely follow the variation of the reference dataset. Similar to the other dilution factors, the results demonstrate a consistent agreement between expected and measured concentrations across the investigated concentration range.

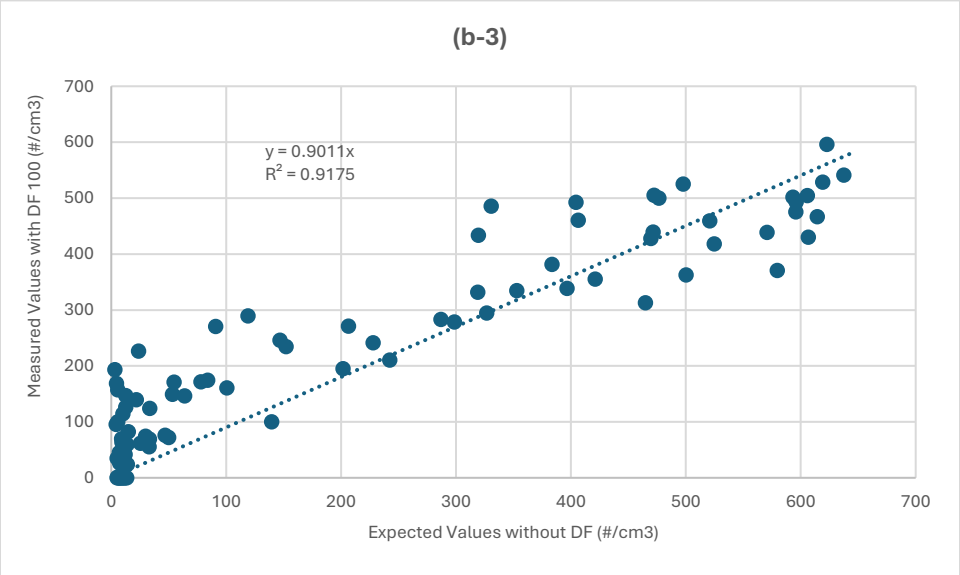

Figure 4.25: *Correlation Between Expected and Measured Values at DF 100*

4.3: ChAMBRe Experiments

The ChAMBRe experiments were conducted to investigate aerosol optical properties under controlled conditions. Unlike field measurements, these experiments allow better control over aerosol sources and environmental parameters, making it possible to study specific processes such as aging and source effects.

Aerosols were generated using well-defined sources, including diesel fuel and hydrotreated vegetable oil (HVO). These sources were selected to represent different combustion conditions and emission characteristics.

After generation, aerosols were injected into the chamber and allowed to mix until a stable and homogeneous concentration was achieved. Different environmental conditions were applied, including exposure to solar radiation and ozone (O_3), in order to simulate atmospheric aging processes.

Real-time optical measurements were performed using AE33 aethalometer for absorption and nephelometer for scattering. These measurements provide continuous information on aerosol optical properties during the evolution of the experiment.

4.3.1 Effect of Aging on Aerosol Absorption (Diesel Case)

The effect of atmospheric aging on aerosol optical properties was first investigated for diesel-generated particles under controlled conditions in the ChAMBRe.

Figure 4.26 shows the spectral absorption behavior for three conditions: fresh diesel, diesel exposed to solar radiation, and diesel aged in the presence of ozone (O_3). A clear increase in absorption is observed as the particles undergo aging.

Fresh diesel emissions exhibit the lowest absorption values, which is typical for freshly emitted soot particles. These particles are mainly composed of black carbon with limited coating or secondary material, resulting in relatively lower absorption and weak wavelength dependence.

After exposure to solar radiation, a moderate increase in absorption is observed. This indicates the formation of secondary material through photochemical processes. These processes lead to condensation of organic compounds on particle surfaces, slightly enhancing light absorption.

The highest absorption is observed for ozone-aged diesel aerosols. In this case, a strong increase in absorption is particularly evident at shorter wavelengths. This behavior suggests significant oxidative aging, leading to the formation of additional light-absorbing species.

Aging also results in an increase in the spectral slope, reflected in higher AAE values. This indicates that the aerosol composition is no longer dominated by pure black carbon, but includes secondary absorbing organic material, such as brown carbon.

Overall, the results demonstrate that atmospheric aging, especially under ozone exposure, significantly enhances aerosol absorption and modifies its spectral characteristics.

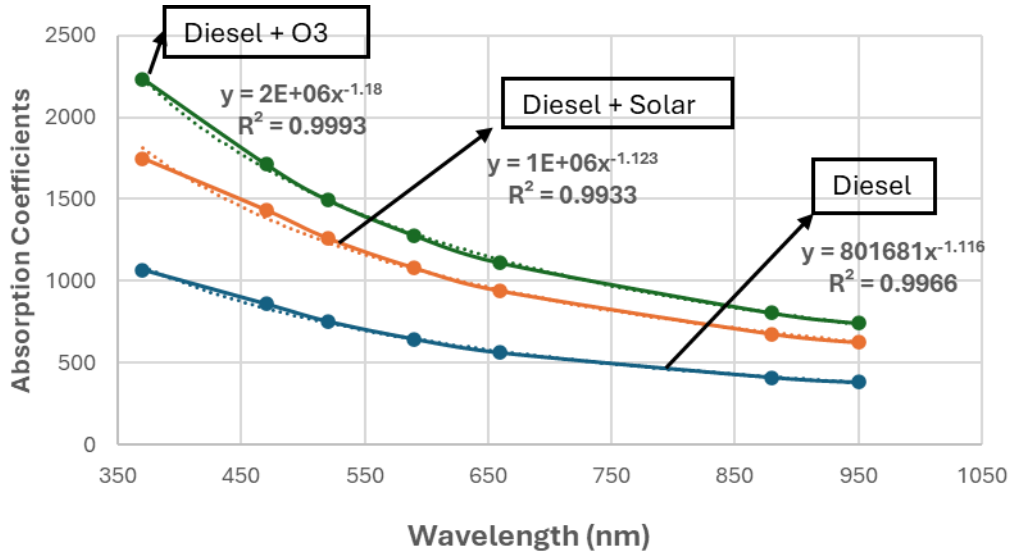

Figure 4.26: *The spectral absorption behavior for Diesel at ChAMBRe for all three conditions.*

4.3.2 Effect of Aging on Aerosol Absorption (HVO Case)

The optical properties of aerosols generated from HVO fuel were analyzed under the same experimental conditions to evaluate the influence of fuel type and aging processes.

Figure 4.27 shows the spectral absorption for fresh HVO, HVO exposed to solar radiation, and HVO aged with ozone. Compared to diesel, fresh HVO emissions exhibit lower absorption, indicating cleaner combustion and reduced formation of soot particles.

Under solar irradiation, a moderate increase in absorption is observed. This suggests that photochemical aging leads to the formation of additional absorbing material, although the effect remains less pronounced compared to diesel.

When exposed to ozone, a stronger increase in absorption is observed, along with a noticeable change in the spectral slope. The enhancement is more significant at shorter wavelengths, indicating the formation of wavelength-dependent absorbing compounds.

The increase in AAE values under aged conditions confirms that secondary organic material contributes to aerosol absorption. This indicates that even fuels with lower initial emissions, such as HVO, can produce absorbing aerosols after atmospheric processing.

Overall, the HVO results highlight that although fresh emissions are cleaner, aging processes can significantly modify aerosol optical properties and increase their radiative impact.

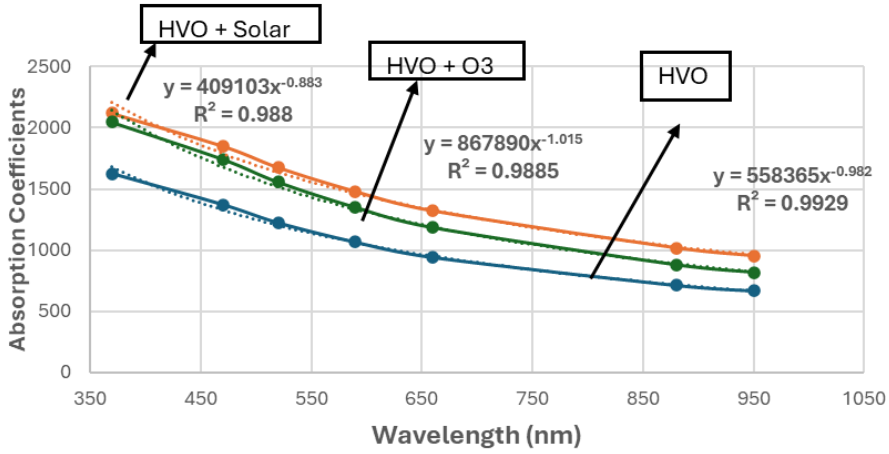

Figure 4.27: *The spectral absorption behavior for HVO at ChAMBRe for all three conditions.*

4.3.3 Aerosol Scattering Properties

The scattering properties of aerosols generated in the ChAMBRe chamber were measured using a nephelometer at different angles (10°, 45°, and 90°) and wavelengths. These measurements provide important information about particle size, composition, and radiative behavior.

Figure 4.28 shows the variation of scattering coefficients under different conditions for diesel and HVO fuels. A clear angular dependence is observed in all cases. The scattering coefficient is highest at **10°**, decreases at **45°**, and reaches the lowest value at **90°**. This behavior is consistent with typical forward scattering of atmospheric aerosol particles.

Diesel-generated aerosols show significantly higher scattering coefficients compared to HVO under all conditions. This indicates that diesel combustion produces particles with higher concentrations and/or more efficient light-scattering properties.

The effect of aging is also clearly visible. Both solar irradiation and ozone exposure lead to an increase in scattering, particularly for diesel aerosols. This suggests that atmospheric aging processes enhance particle size through condensation and secondary material formation, which increases scattering efficiency.

For HVO, scattering values are generally lower, but aging still results in a noticeable increase. However, the magnitude of change is smaller compared to diesel, indicating differences in particle formation and aging mechanisms between the two fuels.

Overall, these results show that both fuel type and atmospheric aging strongly influence aerosol scattering properties. Diesel produces more optically active particles, while aging enhances scattering through secondary processes, contributing to changes in aerosol radiative effects.

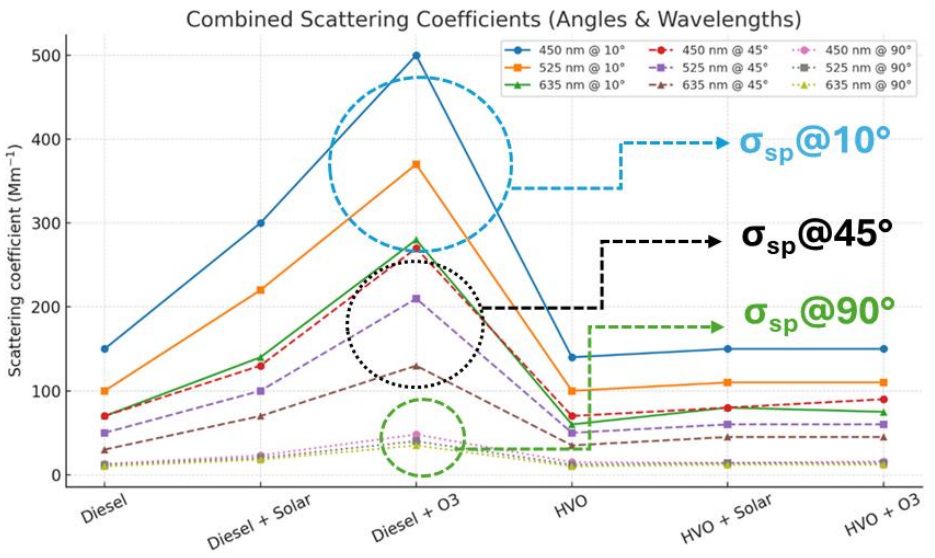

Figure 4.28: *Scattering coefficients of aerosols measured at different angles (10°, 45°, and 90°) for diesel and HVO under fresh and aged conditions in the ChAMBRe.*

4.3.4 Single Scattering Albedo (SSA) Analysis

The single scattering albedo (SSA) was calculated to evaluate the relative contribution of scattering and absorption for aerosols generated under different conditions. SSA is a key

parameter for understanding the radiative effect of aerosols, as it indicates whether particles are more scattering or absorbing.

Figure 4.29 shows the SSA values at 520/525 nm for both diesel and HVO under fresh and aged conditions. Clear differences are observed between the two fuel types and aging processes.

Diesel aerosols exhibit higher SSA values compared to HVO under both fresh and aged conditions. This indicates that diesel particles have a relatively stronger scattering contribution, especially after aging.

The effect of aging is clearly visible. Both solar irradiation and ozone exposure increase SSA, with the strongest enhancement observed under ozone conditions. This increase is more pronounced for diesel, suggesting that oxidative aging leads to significant formation of secondary material, which enhances scattering.

In contrast, HVO aerosols show consistently lower SSA values. This indicates that HVO particles remain more absorption-dominated even after aging. Although some increase in SSA is observed under solar and ozone exposure, the overall change is smaller compared to diesel.

The increase in SSA with aging reflects the growth of particles and the formation of secondary coatings, which enhance scattering relative to absorption. This behavior is consistent with the nephelometer results showing increased scattering under aged conditions.

Overall, the SSA analysis confirms that fuel type and atmospheric aging strongly influence aerosol radiative properties. Diesel aerosols tend to become more scattering-dominated after aging, while HVO aerosols remain relatively more absorbing.

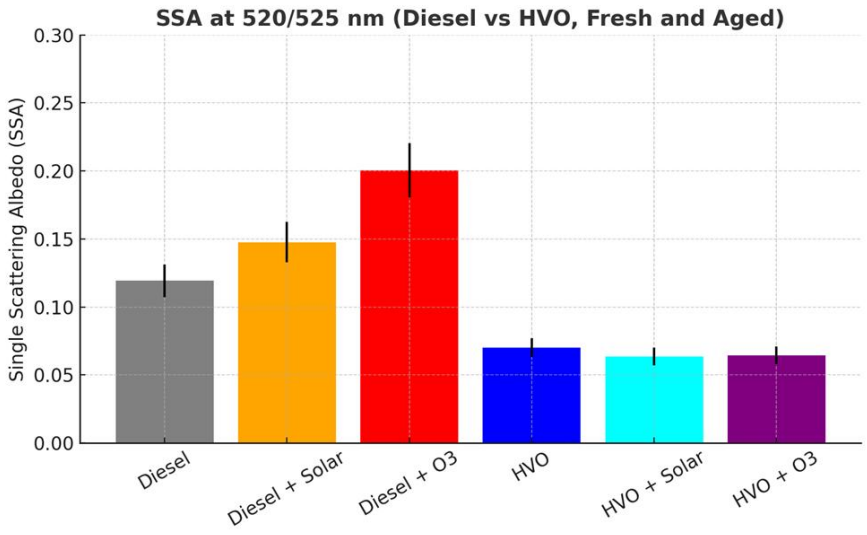

Figure 4.29: *Single scattering albedo (SSA) of aerosols at 520/525 nm for diesel and HVO under fresh and aged conditions in the ChAMBRe.*

4.4: Field Measurements Conducted at the Multedo Site (Genoa, Italy)

4.4.1: $PM_{2.5}$ Mass Concentration (Gravimetric Analysis)

The $PM_{2.5}$ mass concentration during the Multedo field campaign was measured using the gravimetric method. This gives a basic idea of how much particulate matter is present in the air and helps in understanding the optical and chemical results discussed later.

Figure 4.30 shows the variation of $PM_{2.5}$ mass concentration over the sampling period. The values range from about 3 to 20 µg m^{-3}, which indicates moderate pollution levels at the Multedo site. Most of the values are between 5 and 15 µg m^{-3}, showing that the aerosol concentration is generally stable with some variations. Some peaks can be seen in the data, with the highest value around 20 µg m^{-3} and the lowest around 3 µg m^{-3}. These changes are likely to be due to local sources such as traffic and nearby industrial activities, as well as changes in weather conditions. The presence of these peaks suggests occasional pollution events.

This shows that the site is influenced by a mix of local sources and transported background aerosol, which is typical for a coastal urban area. Even though the concentrations are moderate, the data still shows clear variability, which is useful for studying aerosol optical properties. Lower $PM_{2.5}$ levels are also helpful because they allow better analysis without strong interference from very high concentrations. These measurements provide a starting point for the following sections, where the relationship between $PM_{2.5}$ mass, optical properties, and chemical composition is discussed.

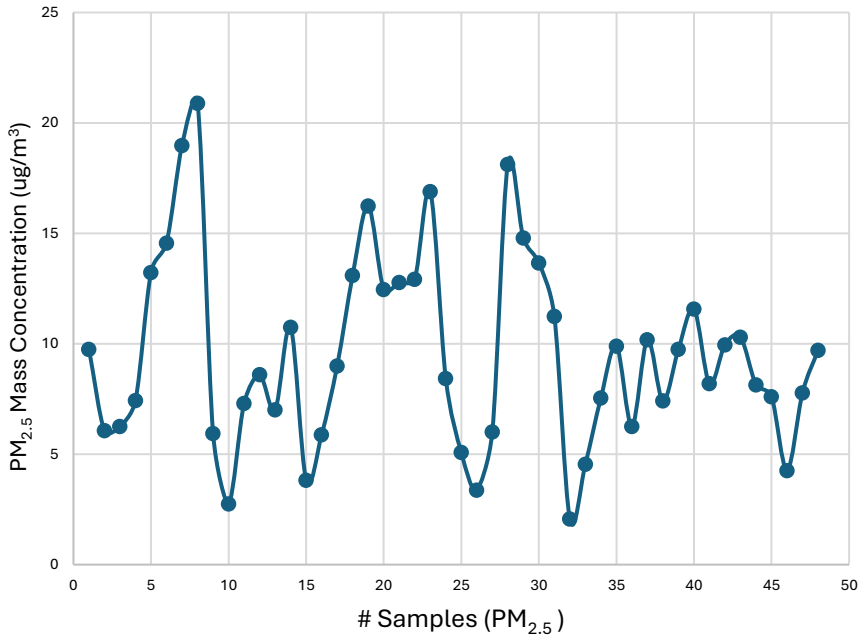

Figure 4.30: *$PM_{2.5}$ mass concentration measured by gravimetric method during the Multedo (Genoa) field campaign.*

4.4.2: Carbonaceous Aerosol Variability (OC and eBC – Real-Time Measurements)

The variability of carbonaceous aerosols during the Multedo field campaign was analyzed using real-time measurements of organic carbon (OC) and equivalent black carbon (eBC) obtained from the CASS/TCA08 system. These measurements provide important information about emission sources and their temporal behavior.

Figure 4.31 shows both the weekly averages and diurnal variation of OC and equivalent eBC concentrations over the entire campaign. A clear difference between OC and eBC behavior can be observed. From the weekly pattern, EC concentrations are consistently higher than OC throughout the week. This indicates a strong influence of combustion-related sources, particularly traffic emissions. Higher eBC values are observed during weekdays, while slightly lower concentrations appear on weekends, suggesting reduced human activity and emissions.

The diurnal variation further supports this observation. eBC shows clear peaks during the morning and evening hours, which correspond to typical rush-hour traffic periods. This pattern confirms that eBC is mainly associated with primary emissions, especially from vehicles. In contrast, OC shows a more stable and smoother variation throughout the day. Unlike eBC, OC does not exhibit sharp peaks, indicating that it is influenced not only by primary emissions but also by secondary formation processes and atmospheric transport. The difference in temporal behavior between OC and eBC is useful for understanding aerosol sources. While eBC mainly represents direct combustion emissions, OC reflects a combination of primary and secondary processes. This distinction is important for interpreting aerosol optical properties in the following sections.

Overall, the real-time OC and eBC measurements provide valuable insight into the source characteristics and temporal dynamics of carbonaceous aerosols at the Multedo site.

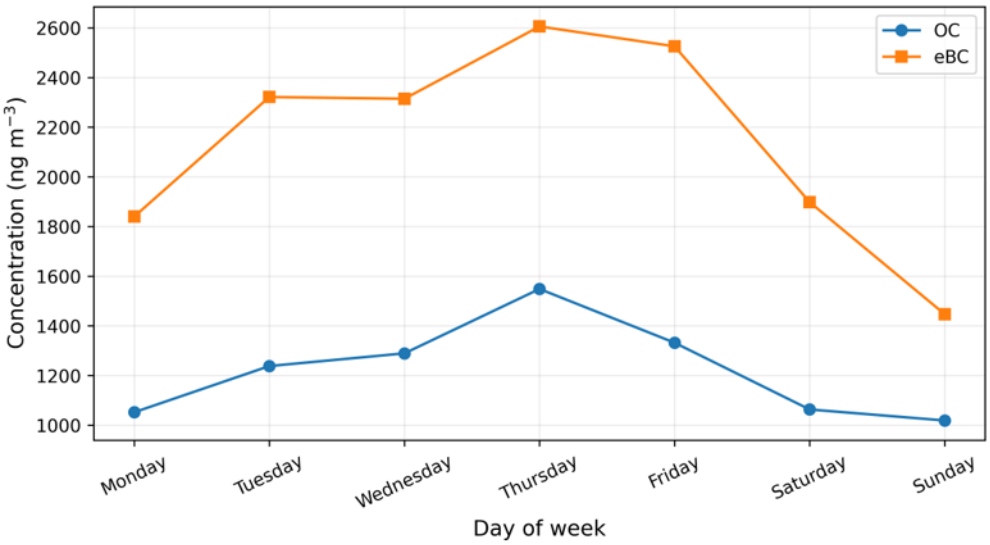

Figure 4.31: *(a) Weekday campaign-average variation of OC and eBC concentrations.*

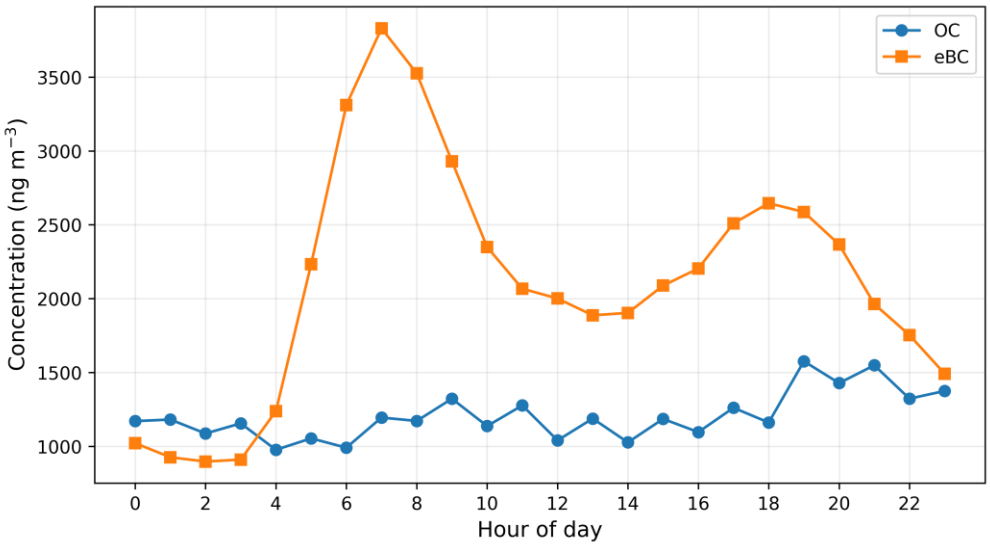

Figure 4.31: *(b) Diurnal campaign-average variation of OC and eBC concentrations.*

4.4.3 Aerosol Absorption Properties and Instrument Comparison

The aerosol absorption properties during the Multedo field campaign were analyzed using both real-time measurements from the AE33 Aethalometer and offline filter-based techniques (MWAA and BLAnCA). This comparison is important to evaluate the consistency between different measurement approaches.

Figure 4.32: shows the absorption coefficient measured at similar ultraviolet wavelengths (around 370–375 nm) for all three techniques. Overall, a good agreement can be observed between AE33, MWAA, and BLAnCA across the entire sampling period.

The values of the absorption coefficient vary between approximately 10 and 30 Mm^{-1}, indicating moderate absorption levels at the Multedo site. All three methods follow a similar trend, with peaks and decreases occurring at the same sampling points. This suggests that the measurements are consistent and reliable.

Some small differences between the instruments can be observed. These variations may be due to differences in measurement principles. The AE33 provides real-time measurements, while MWAA and BLAnCA are based on filter samples, which may be affected by factors such as filter loading, extraction, and wavelength differences.

Despite these differences, the overall agreement between the three methods confirms that the offline optical techniques (MWAA and BLAnCA) are able to reproduce the absorption behavior measured by the AE33. This is important for further analysis, especially for studying spectral absorption and brown carbon (BrC) using filter-based methods.

The consistency between real-time and offline measurements increases confidence in the dataset and supports the use of multiple techniques for a more detailed characterization of aerosol optical properties.

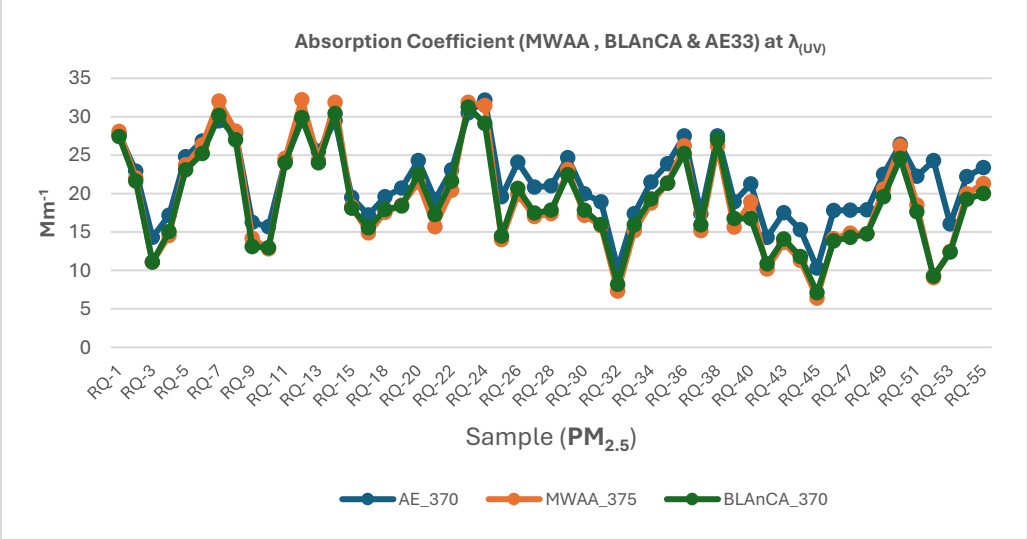

Figure 4.32: *Comparison of aerosol absorption coefficient measured by AE33, MWAA, and BLAnCA at UV wavelengths during the Multedo field campaign.*

4.4.4 Aerosol Absorption at Visible Wavelengths

In addition to the ultraviolet region, aerosol absorption was also analyzed at **visible wavelengths (520–532 nm)** using AE33, MWAA, and BLAnCA. This comparison helps to understand how absorption changes with wavelength and provides further validation of the measurement techniques.

Figure 4.33: shows the absorption coefficient at green wavelengths for all samples. The values generally range between 5 and 25 Mm^{-1}, which are lower than those observed at shorter wavelengths. This decrease in absorption with increasing wavelength is expected and reflects the typical behavior of atmospheric aerosols.

Similar to the UV comparison, a good agreement is observed between AE33, MWAA, and BLAnCA. All three methods follow the same variation pattern across the samples, indicating consistent measurements. The peaks and lower values appear at similar points, which confirms the reliability of both real-time and offline techniques.

Small differences between the instruments are still present. These differences can be related to the measurement approach (real-time vs filter-based) and slight variations in wavelength. However, these variations are relatively small and do not affect the overall trend.

The comparison between UV and visible wavelengths also shows that absorption is stronger at shorter wavelengths. This behavior suggests the presence of wavelength-dependent absorbing components, such as brown carbon (BrC), in addition to black carbon. This aspect will be discussed in more detail in the next section.

Overall, the results confirm that both AE33 and offline techniques (MWAA and BLAnCA) provide consistent absorption measurements across different wavelengths, supporting their use for further spectral analysis.

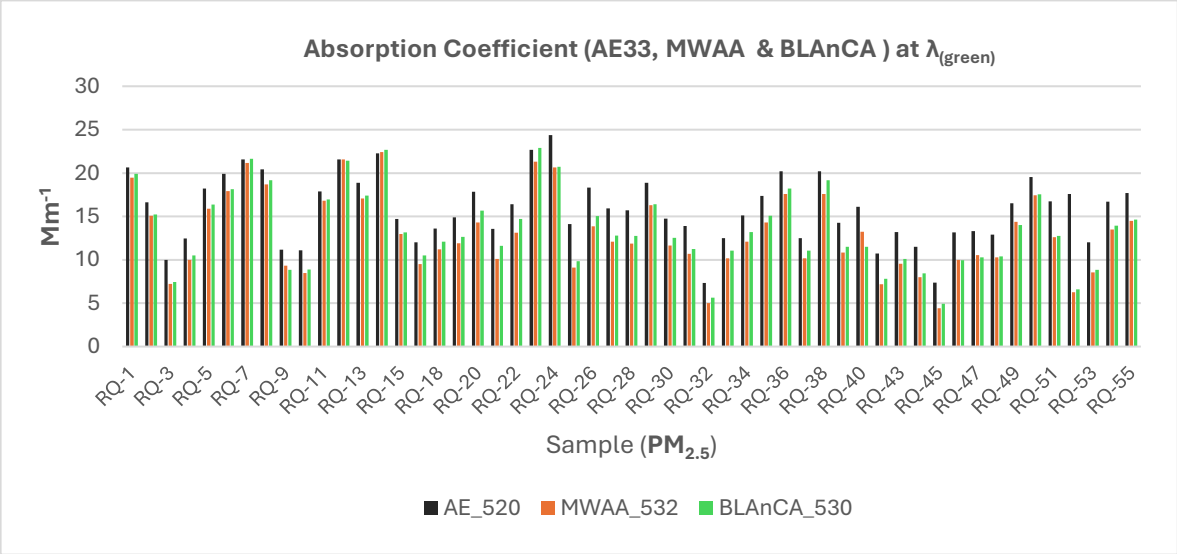

Figure 4.33: *Comparison of aerosol absorption coefficient measured by AE33, MWAA, and BLAnCA at visible (green) wavelengths during the Multedo field campaign.*

4.4.5 Aerosol Absorption at Infrared Wavelengths

Aerosol absorption was also analyzed at infrared wavelengths (850–880 nm) using AE33, MWAA, and BLAnCA. This wavelength range is mainly sensitive to black carbon (BC) and is less affected by other absorbing components such as brown carbon.

Figure 4.34: shows the absorption coefficient at infrared wavelengths for all samples. The values are generally lower compared to UV and visible regions, ranging approximately between 4 and 15 Mm^{-1}. This decrease in absorption with increasing wavelength follows the expected behavior of atmospheric aerosols.

A good agreement is again observed between the three measurement techniques. AE33, MWAA, and BLAnCA show similar trends across all samples, with peaks and low values occurring at the same points. This confirms the consistency of both real-time and filter-based measurements.

Compared to the UV region, the variation between samples is smaller in the infrared range. This suggests that absorption at these wavelengths is dominated by black carbon, which has a more stable and wavelength-independent absorption behavior. In contrast,

the stronger variation observed at shorter wavelengths is likely due to additional contributions from brown carbon and other organic compounds.

The comparison across UV, visible, and infrared wavelengths highlights the spectral dependence of aerosol absorption. While BC dominates absorption in the infrared region, the higher absorption at shorter wavelengths indicates the presence of other absorbing species.

Overall, the results confirm that the three techniques provide consistent measurements across all wavelengths and support their use for further analysis of spectral absorption properties and source contributions.

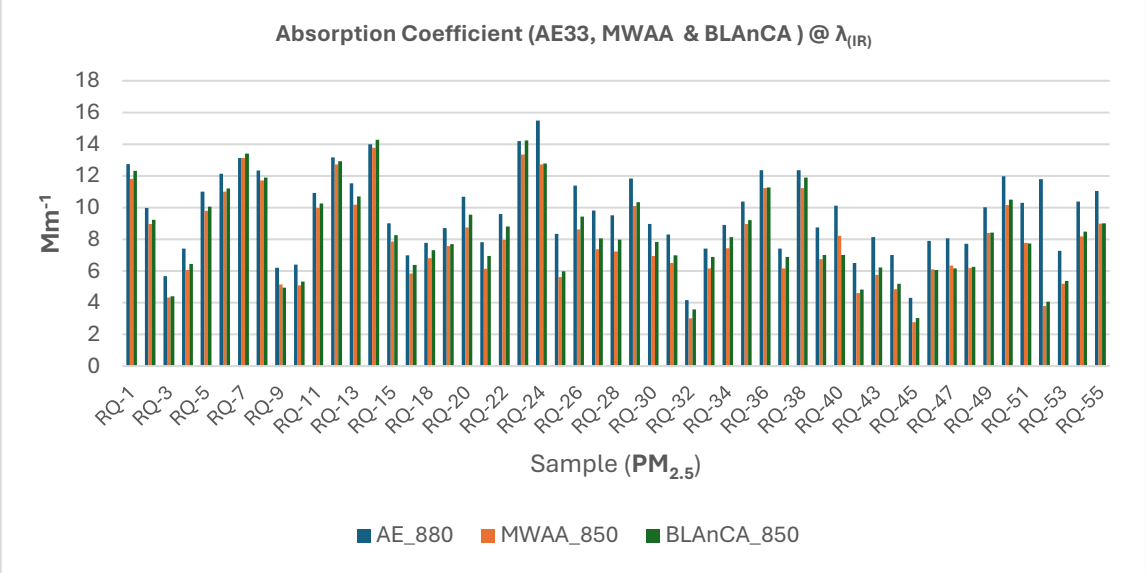

Figure 4.34: *Comparison of aerosol absorption coefficient measured by AE33, MWAA, and BLAnCA at infrared wavelengths during the Multedo field campaign.*

4.4.6 Spectral Absorption and Brown Carbon Contribution

The spectral dependence of aerosol absorption was analyzed using measurements from **AE33, MWAA, and BLAnCA** across multiple wavelengths. This analysis helps to understand how absorption changes with wavelength and provides information about aerosol composition.

Figure 4.35: shows that the absorption coefficient decreases with increasing wavelength for all three instruments. This behavior follows a power-law trend, which is typical for atmospheric aerosols, especially those containing carbonaceous components.

A good agreement is observed between MWAA, BLAnCA, and AE33 over the full wavelength range. The overall trend is similar for all instruments, confirming the consistency of the measurements. However, AE33 shows slightly higher absorption values, especially at shorter wavelengths. This difference may be related to the real-time measurement approach and instrumental characteristics.

The decrease in absorption from UV to infrared wavelengths indicates the presence of wavelength-dependent absorbing components, particularly brown carbon (BrC). While black carbon (BC) absorbs radiation almost equally across wavelengths, BrC shows stronger absorption at shorter wavelengths. Therefore, the higher absorption observed in the UV region suggests a contribution from organic aerosols.

The spectral behavior was further analyzed using the absorption Ångström exponent (AAE). The calculated AAE values are close to 1.0–1.1 for all instruments, indicating that absorption is mainly dominated by black carbon, with a smaller contribution from brown carbon.

The high coefficient of determination ($R^2 > 0.99$) for the spectral fitting confirms that the power-law relationship provides a good description of the absorption behavior.

Overall, the results show that:

- absorption decreases with increasing wavelength,
- the three instruments provide consistent spectral measurements,
- black carbon is the dominant absorber,
- and brown carbon contributes mainly at shorter wavelengths.

This spectral analysis is important for understanding the **composition and radiative effects of aerosols**, and it provides a basis for further discussion of aerosol sources and optical properties.

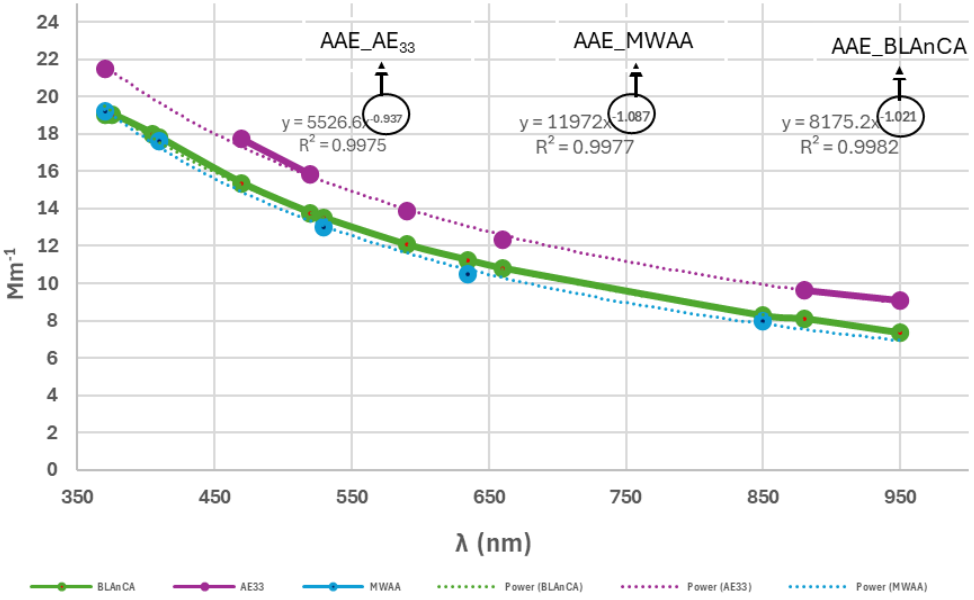

Figure 4.35: *Spectral variation of aerosol absorption coefficient measured by AE33, MWAA, and BLAnCA, including power-law fitting and AAE estimation during the Multedo field campaign.*

4.5: Aerosol Properties in Lahore Field Campaign

4.5.1 $PM_{2.5}$ Mass Concentration and Pollution Episodes (Lahore)

The $PM_{2.5}$ mass concentration during the Lahore field campaign was analyzed using the gravimetric method to understand the level of air pollution and its variability. Compared to the Multedo site, the Lahore dataset shows significantly higher concentrations, indicating a more polluted environment. Figure 4.36: shows the variation of $PM_{2.5}$ mass concentration over the sampling period. The values vary widely, ranging from moderate levels to very high concentrations. In several cases, $PM_{2.5}$ exceeds 350–400 µg m^{-3}, indicating severe pollution conditions. Two strong pollution episodes can be clearly observed in the dataset. These episodes are marked by sharp increases in $PM_{2.5}$ concentration, followed by rapid decreases. Such behavior suggests the influence of intense local emissions combined with unfavorable meteorological conditions, such as low wind speed and stable atmospheric layers.

The overall variability in Lahore is much higher than that observed at the Multedo site. This reflects the combined impact of traffic emissions, industrial activities, biomass burning, and dust resuspension, which are common sources of particulate matter in urban areas of South Asia (Begum et al., 2011; Pant et al., 2015; Hopke et al., 2020)

High $PM_{2.5}$ levels are often associated with increased concentrations of carbonaceous aerosols, particularly black carbon and organic carbon. These components play a significant role in aerosol optical properties, especially absorption. Therefore, the Lahore dataset provides a valuable opportunity to study aerosol behavior under high pollution conditions.

In addition, the presence of strong pollution episodes makes this dataset suitable for comparison with controlled chamber experiments, as it allows investigation of aerosol optical properties over a wide range of concentrations.

Overall, the Lahore field campaign highlights the impact of intense anthropogenic emissions on air quality and provides an important contrast to the relatively moderate conditions observed at the Multedo site.

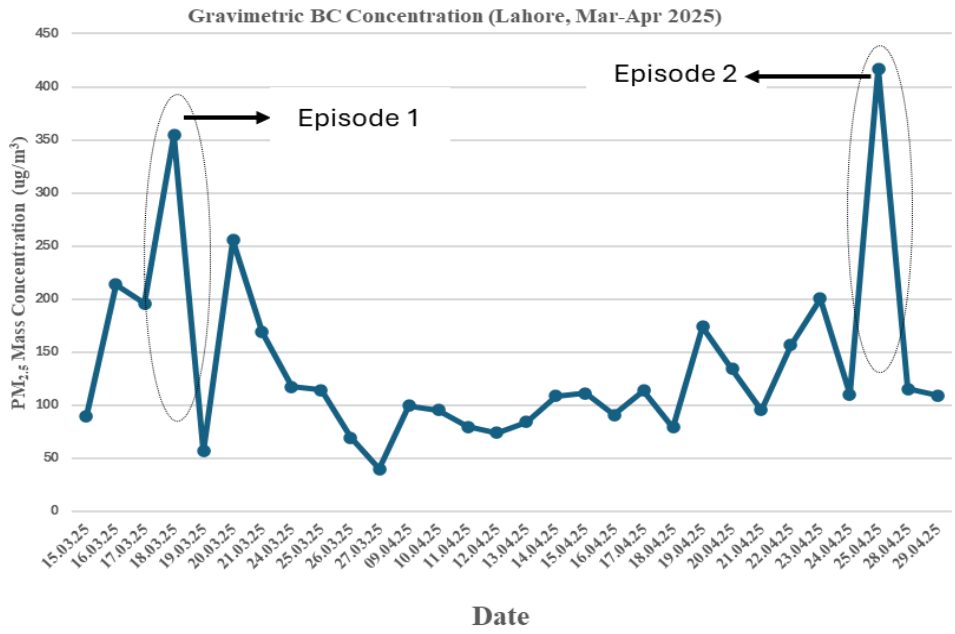

Figure 4.36: *$PM_{2.5}$ mass concentration and pollution episodes observed during the Lahore field campaign (March–April 2025).*

4.5.2: Aerosol Absorption Properties in Lahore (MWAA & BLAnCA)

The aerosol light absorption properties during the Lahore field campaign were analyzed using filter-based techniques, namely MWAA and BLAnCA. These instruments provide wavelength-dependent absorption measurements and are particularly useful for studying carbonaceous aerosols under high pollution conditions.

Figure 4.37: shows the absorption coefficient at 850 nm for all collected $PM_{2.5}$ samples. The results indicate a strong variability in absorption across different samples, reflecting changes in aerosol concentration and composition during the campaign.

In general, the absorption coefficient ranges from relatively low values (40–60 Mm^{-1}) to very high values exceeding 300 Mm^{-1}. The highest peak is observed around sample PK24, where absorption increases sharply. This peak corresponds to a pollution episode identified earlier in the $PM_{2.5}$ mass concentration data, confirming that high particle loading is associated with enhanced light absorption.

Both MWAA and BLAnCA show very similar trends across all samples, indicating good agreement between the two offline techniques. The differences between the two measurements are small, suggesting that both methods are reliable for quantifying aerosol absorption at near-infrared wavelengths.

The high absorption values observed in Lahore are mainly attributed to the presence of carbonaceous aerosols, particularly black carbon. At 850 nm, absorption is dominated by black carbon, with minimal contribution from brown carbon. Therefore, these results indicate a strong influence of combustion-related emissions such as traffic, biomass burning, and industrial activities.

Compared to the Multedo field campaign, the absorption levels in Lahore are significantly higher. This highlights the impact of intense anthropogenic emissions and confirms that Lahore represents a high-pollution environment with strong aerosol components.

Overall, the absorption measurements demonstrate that Lahore aerosols have a strong light-absorbing capacity, which can contribute to atmospheric warming and reduced visibility. These findings are consistent with the high $PM_{2.5}$ concentrations observed during the campaign and emphasize the importance of carbonaceous aerosols in urban air pollution.

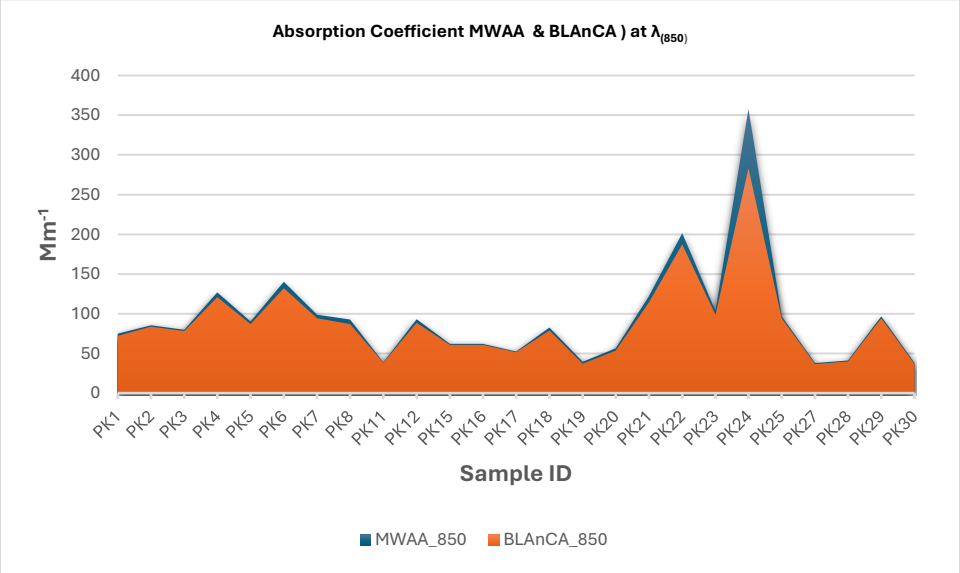

Figure 4.37: *Absorption coefficient of $PM_{2.5}$ at 850 nm measured using MWAA and BLAnCA during the Lahore field campaign.*

4.5.3 Spectral Absorption Characteristics (Lahore)

The spectral behavior of aerosol absorption was analyzed by calculating the average absorption coefficients at different wavelengths using MWAA and BLAnCA measurements. Figure 4.38: presents the mean absorption values for all $PM_{2.5}$ samples as a function of wavelength.

A clear decreasing trend in absorption with increasing wavelength is observed for both instruments. This behavior follows the typical power-law dependence of carbonaceous aerosols and confirms the presence of wavelength-dependent absorption in the dataset.

At shorter wavelengths (UV–blue region), a noticeable disagreement between MWAA and BLAnCA is observed. MWAA shows higher absorption values compared to

BLAnCA, especially below ~450 nm. However, as the wavelength increases, this difference gradually decreases, and both instruments show very good agreement in the near-infrared region.

This difference at lower wavelengths may be attributed to several factors. First, the contribution of brown carbon (BrC) is more significant at shorter wavelengths, and its quantification is more sensitive to measurement techniques. Second, filter loading effects may also play an important role. Since the Lahore samples are heavily loaded due to high $PM_{2.5}$ concentrations, the optical response of the filters can be affected, particularly at shorter wavelengths where absorption is stronger. This can lead to differences in how MWAA and BLAnCA capture absorption in the UV region.

In addition, variations in instrumental calibration, light scattering correction, and filter-based measurement principles may further contribute to the observed discrepancy at lower wavelengths.

At higher wavelengths (e.g., 850 nm), absorption is mainly dominated by black carbon, which exhibits relatively wavelength-independent behavior. As a result, both MWAA and BLAnCA converge and provide consistent measurements.

Overall, the spectral analysis confirms that Lahore aerosols contain both black carbon and brown carbon components. The stronger absorption in the UV region indicates the presence of light-absorbing organic compounds, while the agreement at longer wavelengths confirms the dominant role of black carbon.

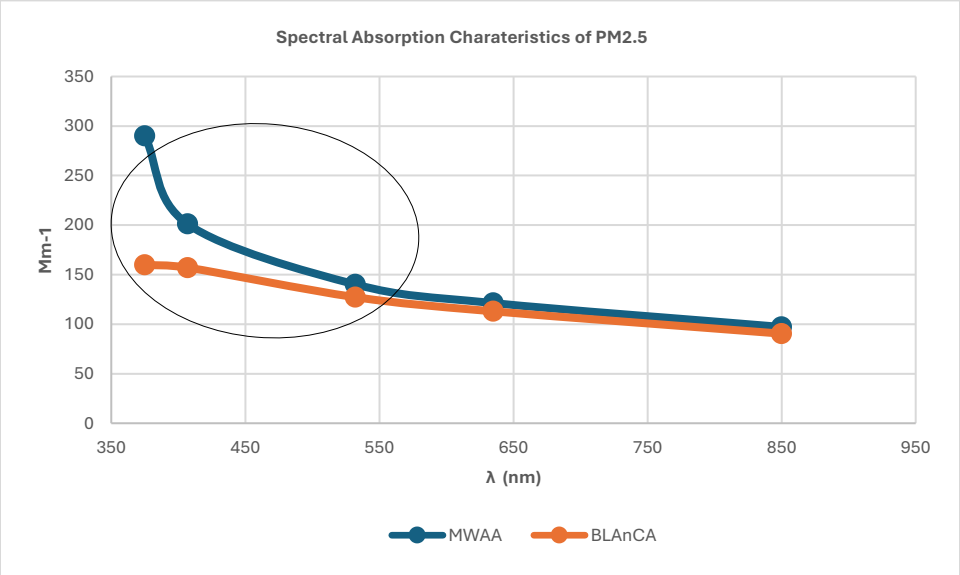

Figure 4.38: *Average spectral absorption of $PM_{2.5}$ measured using MWAA and BLAnCA during the Lahore field campaign.*

4.5.4: Absorption Ångström Exponent (AAE) – Lahore

The wavelength dependence of aerosol absorption was further analyzed using the absorption Ångström exponent (AAE), which provides important information about aerosol composition and dominant sources. The AAE was obtained by fitting the spectral absorption data with a power-law relationship.

Figure 4.39 shows the spectral absorption curves along with the fitted power-law functions for both MWAA and BLAnCA. A clear monotonic decrease in absorption with increasing wavelength is observed, consistent with typical behavior of carbonaceous aerosols.

The calculated AAE values are approximately 1.05–1.11 for both instruments. These values indicate that aerosol absorption in Lahore is mainly dominated by black carbon, which typically exhibits AAE values close to unity. This suggests a strong influence of combustion-related sources such as traffic emissions, fossil fuel burning, and industrial activities. The high coefficient of determination ($R^2 > 0.99$) confirms that the power-law

fitting provides a very good representation of the spectral data, indicating reliable measurements and consistent spectral behavior.

Both MWAA and BLAnCA show very similar spectral slopes, although a small offset is observed between the two datasets. This offset is likely related to differences in instrument response and filter-based measurement effects, particularly at shorter wavelengths where absorption is stronger. Despite these minor differences, the close agreement between the AAE values obtained from both instruments demonstrates good consistency and confirms the reliability of the measurements.

Overall, the AAE analysis indicates that black carbon is the dominant absorbing component in Lahore aerosols. This is consistent with the high pollution levels observed and reflects the strong impact of combustion sources in the study area.

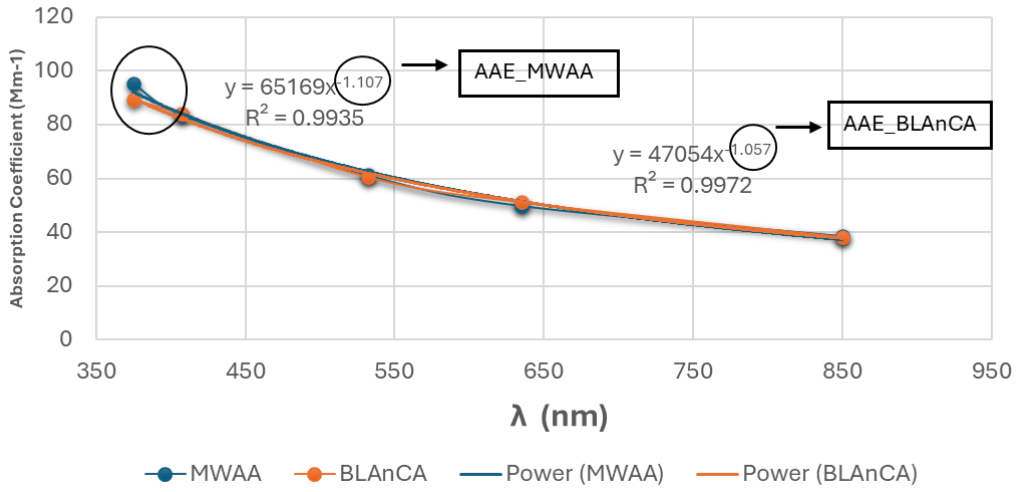

Figure 4.39: *Spectral absorption and AAE determination of $PM_{2.5}$ using MWAA and BLAnCA during the Lahore field campaign.*

4.6: Final Comparison: Multedo vs Lahore vs ChAMBRe

This section provides a comparison between aerosol properties observed under moderate pollution conditions (Multedo, Genoa), high pollution conditions (Lahore), and controlled laboratory experiments (ChAMBRe). The objective is to link real atmospheric

observations with controlled experimental results in order to better understand the processes governing aerosol optical behavior.

The combined analysis of field campaigns and chamber experiments provides a consistent understanding of aerosol optical behavior:

- **Multedo** represents low to moderate pollution conditions with relatively weak absorption and limited spectral dependence
- **Lahore** represents high pollution conditions with strong absorption and clear evidence of carbonaceous aerosols
- **ChAMBRe** experiments provide mechanistic insight into how emission sources and aging processes control aerosol properties

Overall, the combined field and laboratory results indicate that aerosol optical properties are governed by a complex interaction of source emissions, particle composition, size distribution, and atmospheric aging. While field observations captured the variability associated with real atmospheric conditions, chamber experiments provided a controlled framework for investigating the processes responsible for these changes. Together, these results improve the interpretation of aerosol absorption and scattering behavior under different environmental conditions.

CHAPTER 5: Conclusions and Future Work

5.1: Conclusions

This thesis presents a comprehensive investigation of the optical properties of atmospheric aerosols, with a particular focus on carbonaceous components, including black carbon (BC) and brown carbon (BrC). The study combines field measurements under different pollution conditions with controlled laboratory experiments in the ChAMBRe chamber, providing both observational and mechanistic insights into aerosol behavior.

The field campaign conducted in Multedo (Genoa) represents relatively clean to moderately polluted conditions. $PM_{2.5}$ concentrations were generally low, with limited variability. Aerosol absorption was also moderate, and the spectral behavior showed weak wavelength dependence, indicating a dominant contribution from black carbon with minimal influence of brown carbon.

In contrast, the Lahore field campaign exhibited significantly higher $PM_{2.5}$ concentrations, with strong pollution episodes exceeding 350–400 μg m^{-3}. Correspondingly, aerosol absorption coefficients were much higher, reflecting the presence of large amounts of carbonaceous material. Spectral analysis revealed stronger wavelength dependence, particularly at shorter wavelengths, suggesting a noticeable contribution from brown carbon. The results indicate that aerosols in Lahore are strongly influenced by combustion sources and atmospheric processing.

The comparison between different measurement techniques demonstrated good agreement between real-time and filter-based optical methods. MWAA and BLAnCA showed consistent spectral behavior, while AE33 provided reliable real-time absorption measurements. Minor discrepancies at shorter wavelengths were attributed to filter loading effects and methodological differences.

The ChAMBRe experiments provided controlled insight into the influence of fuel type and atmospheric aging. Fresh emissions from diesel and HVO showed different optical properties, with HVO producing lower absorption, consistent with cleaner combustion.

However, aging processes significantly modified aerosol behavior. Both solar irradiation and ozone exposure increased absorption and scattering, with the strongest effects observed under ozone aging.

A key finding of the chamber experiments is the increase in wavelength dependence of absorption after aging, reflected in higher AAE values. This indicates the formation of secondary absorbing material, likely associated with brown carbon. These results help explain the spectral behavior observed in polluted environments such as Lahore.

Scattering measurements showed strong angular dependence and increased with aging, leading to higher single scattering albedo (SSA). Diesel aerosols exhibited higher SSA compared to HVO, particularly after aging, indicating a stronger contribution of scattering processes.

Overall, the combined analysis of field campaigns and chamber experiments demonstrates that aerosol optical properties are controlled by a combination of emission sources, chemical composition, and atmospheric aging processes. The formation of secondary material during aging plays a crucial role in modifying both the magnitude and spectral dependence of aerosol absorption.

5.2: Future Work

Future research can build upon this work to further improve the understanding of aerosol optical properties and their climatic effects.

First, extended field campaigns covering different seasons and locations would help to better capture the variability of aerosol properties under diverse environmental conditions. In particular, long-term measurements in highly polluted regions such as South Asia would provide valuable insights into seasonal trends and source contributions.

Second, further investigation of brown carbon is needed, especially its formation mechanisms and optical properties. Advanced chemical analysis techniques could be combined with optical measurements to better characterize the composition and evolution of light-absorbing organic aerosols.

Finally, the experimental results obtained in this study can be used to improve aerosol representation in climate models. Incorporating more realistic explanations of aerosol aging and optical properties will help reduce uncertainties in estimates of aerosol radiative forcing.

Bibliography

Adachi, K., Chung, S. H., & Buseck, P. R. (2010). Shapes of soot aerosol particles and implications for their effects on climate. *Journal of Geophysical Research: Atmospheres*, *115*(D15).

Adachi, K., Zaizen, Y., Kajino, M., and Igarashi, Y., 2020. Mixing state of soot particles and their morphologies in the urban atmosphere. Atmospheric Chemistry and Physics, 20, pp.11461–11475.

Anderson, T. L., & Ogren, J. A. (1998). Determining aerosol radiative properties using the TSI 3563 integrating nephelometer. *Aerosol Science and Technology*, *29*(1), 57-69.

Andreae, M. O., & Gelencsér, A. (2006). Black carbon or brown carbon? The nature of light-absorbing carbonaceous aerosols. *Atmospheric Chemistry and Physics*, *6*(10), 3131-3148.

Andreae, M. O., & Rosenfeld, D. J. E. S. R. (2008). Aerosol–cloud–precipitation interactions. Part 1. The nature and sources of cloud-active aerosols. *Earth-Science Reviews*, *89*(1-2), 13-41.

Ångström, A. (1964). The parameters of atmospheric turbidity. *Tellus*, *16*(1), 64-75.

Arnott, W. P., Moosmüller, H., & Walker, J. W. (2000). Nitrogen dioxide and kerosene-flame soot calibration of photoacoustic instruments for measurement of light absorption by aerosols. *Review of Scientific Instruments*, *71*(12), 4545-4552.

Begum, B.A., Biswas, S.K., Hopke, P.K., 2011. Key issues in controlling air pollutants in Dhaka, Bangladesh. Atmospheric Environment, 45, 7705–7713.

Bianchi, F., Kurtén, T., Riva, M., et al., 2019. Highly oxygenated organic molecules (HOM) from gas-phase autoxidation involving peroxy radicals. Chemical Reviews, 119, pp.3472–3509.

Birch, M. E. (2002). Occupational monitoring of particulate diesel exhaust by NIOSH method 5040. *Applied occupational and environmental hygiene*, *17*(6), 400-405.

Birch, M. E., and Cary, R. A., 1996. Elemental carbon-based method for monitoring occupational exposures to particulate diesel exhaust. Aerosol Science and Technology, 25, pp.221–241.

Birch, M.E., Cary, R.A., 1996. Elemental carbon-based method for monitoring occupational exposures to particulate diesel exhaust. Aerosol Science and Technology, 25, 221–241.

Bohren, C. F., & Huffman, D. R. (2008). *Absorption and scattering of light by small particles*. John Wiley & Sons.

Bond, T. C., Doherty, S. J., Fahey, D. W., Forster, P. M., Berntsen, T., DeAngelo, B. J., ... & Zender, C. S. (2013). Bounding the role of black carbon in the climate system: A scientific assessment. *Journal of geophysical research: Atmospheres*, *118*(11), 5380-5552.

Burnett, R. T., Pope III, C. A., Ezzati, M., Olives, C., Lim, S. S., Mehta, S., ... & Cohen, A. (2014). An integrated risk function for estimating the global burden of disease attributable to ambient fine particulate matter exposure. *Environmental health perspectives*, *122*(4), 397.

Buseck, P. R., & Adachi, K. (2008). Nanoparticles in the atmosphere. *Elements*, *4*(6), 389-394.

Cavalli, Fabrizia, Mar Viana, Karl Espen Yttri, Johan Genberg, and J-P. Putaud. "Toward a standardised thermal-optical protocol for measuring atmospheric organic and elemental carbon: the EUSAAR protocol." *Atmospheric Measurement Techniques Discussions* 2, no. 5 (2009): 2321-2345.

Chow, J.C., Watson, J.G., Chen, L.W.A., et al., 2007. The IMPROVE_A temperature protocol for thermal/optical carbon analysis: maintaining consistency with a long-term database. Journal of the Air & Waste Management Association, 57, 1014–1023.

Chow, J.C., Watson, J.G., Pritchett, L.C., Pierson, W.R., Frazier, C.A., Purcell, R.G., 1993. The DRI thermal/optical reflectance carbon analysis system: description, evaluation and applications in U.S. air quality studies. Atmospheric Environment, 27A, 1185–1201.

Cohen, A. J., Brauer, M., Burnett, R., et al., 2017. Estimates and 25-year trends of the global burden of disease are attributable to ambient air pollution. The Lancet, 389, pp.1907–1918.

Danelli, S.G., Parodi, F., Massabò, D., et al., 2021. Characterization of aerosol optical properties and atmospheric processes using the ChAMBRe simulation chamber. Atmospheric Measurement Techniques, 14, 165–185.

De Martino, M., Gagliardi, S., Gargano, G., Petracca Altieri, R. M., & Cornacchia, C. (2026). Open innovation in research infrastructures: the case of the Aerosol, Clouds and Trace Gases Research Infrastructure (ACTRIS). *European Journal of Innovation Management*, *29*(11), 401-426.

Dekati Ltd., 2020. Dekati® eDiluter™ Pro User Manual, Version 1.5. Dekati Ltd., Kangasala, Finland.

Di Biagio, C., Formenti, P., Cazaunau, M., Pangui, E., Marchand, N., & Doussin, J. F. (2017). Aethalometer multiple scattering correction C ref for mineral dust aerosols. *Atmospheric Measurement Techniques*, *10*(8), 2923-2939.

Dockery, D. W., Pope, C. A., Xu, X., Spengler, J. D., Ware, J. H., Fay, M. E., ... & Speizer, F. E. (1993). An association between air pollution and mortality in six US cities. *New England journal of medicine*, *329*(24), 1753-1759.

Drinovec, L., Močnik, G., Zotter, P., et al., 2015. The dual-spot Aethalometer: an improved measurement of aerosol black carbon with real-time loading compensation. Atmospheric Measurement Techniques, 8, pp.1965–1979.

Drinovec, L., Močnik, G., Zotter, P., Prévôt, A. S. H., Ruckstuhl, C., Coz, E., ... & Hansen, A. D. A. (2015). The "dual-spot" Aethalometer: an improved measurement of aerosol black carbon with real-time loading compensation. *Atmospheric measurement techniques*, *8*(5), 1965-1979.

Ecotech Pty Ltd., 2013. Aurora 4000 Integrating Nephelometer User Manual, Rev 1.0.

European Union. (2016). Regulation (EU) 2016/1628 of the European Parliament and of the Council of 14 September 2016 on requirements relating to gaseous and particulate pollutant emission limits and type approval for internal combustion engines for non-road mobile machinery, amending Regulations (EU) No 1024/2012 and (EU) No. 167/2013, and amending and repealing Directive 97/68/EC. *Official Journal of the European Union*, *252*.

Fabrizia, C. A. V. A. L. L. I., Jean-Philippe, P. U. T. A. U. D., Mar, V. I. A. N. A., Espen, Y. K., & Johan, G. E. N. B. E. R. G. (2010). Toward a Standardised Thermal-Optical Protocol for Measuring Atmospheric Organic and Elemental Carbon: The EUSAAR Protocol.

Hallquist, M., Wenger, J. C., Baltensperger, U., Rudich, Y., Simpson, D., Claeys, M., ... & Wildt, J. (2009). The formation, properties and impact of secondary organic aerosol: current and emerging issues. *Atmospheric chemistry and physics*, *9*(14), 5155-5236.

Hänel, G., 1987. Radiation budget of atmospheric aerosol layers. Journal of Aerosol Science, 18, 501–515.

Hänel, G., 1994. Optical properties of atmospheric aerosol particles. Applied Optics, 33, 7187–7196.

Hansen, A. D., Rosen, H., & Novakov, T. (1984). The aethalometer—an instrument for the real-time measurement of optical absorption by aerosol particles. *Science of the Total Environment*, *36*, 191-196.

Haywood, J., and Boucher, O., 2000. Estimates of the direct and indirect radiative forcing due to tropospheric aerosols: A review. Reviews of Geophysics, 38, pp.513–543.

Heintzenberg, J., Charlson, R.J., 1996. Design and applications of the integrating nephelometer: A review. Journal of Atmospheric and Oceanic Technology, 13, 987–1000.

Hobbs, P. V. (2000). *Introduction to atmospheric chemistry*. Cambridge University Press.

Hopke, P.K., et al., 2020. Urban air quality and particulate matter sources in South Asia. Atmospheric Pollution Research, 11, 200–214.

Huntzicker, J.J., Johnson, R.L., Shah, J.J., Cary, R.A., 1982. Analysis of organic and elemental carbon in ambient aerosols by a thermal-optical method. Particulate Carbon: Atmospheric Life Cycle, 79–88.

IPCC, 2021. Climate Change 2021: The Physical Science Basis. Cambridge University Press.

IPCC, 2021. Climate Change 2021: The Physical Science Basis. Contribution of Working Group I to the Sixth Assessment Report of the Intergovernmental Panel on Climate Change. Cambridge University Press.

Isolabella, T., Brunoldi, M., Mazzei, F., et al., 2025. The Broadband Light Analyzer of Complex Aerosol: characterization and first applications. Atmospheric Environment, 358, 121341.

Jimenez, J. L., Canagaratna, M. R., Donahue, N. M., et al., 2009. Evolution of organic aerosols in the atmosphere. Science, 326, pp.1525–1529.

Kazemimanesh, M., et al., 2019. Characterization of soot particles generated by a mini inverted soot generator for laboratory studies. Aerosol Science and Technology, 53, 134–147.

Kelly, F. J., and Fussell, J. C., 2012. Size, source and chemical composition as determinants of toxicity attributable to ambient particulate matter. Atmospheric Environment, 60, pp.504–526.

Kirchstetter, T. W., Novakov, T., and Hobbs, P. V., 2004. Evidence that the spectral dependence of light absorption by aerosols is affected by organic carbon. Journal of Geophysical Research: Atmospheres, 109, D21208.

Kirchstetter, T.W., Novakov, T., 2007. Controlled generation of black carbon particles from a diffusion flame and applications in aerosol research. Aerosol Science and Technology, 41, 835–846.

Kulkarni, P., Baron, P. A., & Willeke, K. (Eds.). (2011). *Aerosol measurement: principles, techniques, and applications*. John Wiley & Sons.

Kulmala, M., Luoma, K., Petäjä, T., et al., 2016. Direct observations of atmospheric aerosol nucleation. Science, 351, pp.278–281.

Kuronen, M., Mikkonen, S., Aakko, P., & Murtonen, T. (2007, October). Hydrotreated vegetable oil as fuel for heavy duty diesel engines. In *SAE 2007 Commercial Vehicle Engineering Congress & Exhibition*. SAE Technical Paper.

Lack, D. A., & Cappa, C. D. (2010). Impact of brown and clear carbon on light absorption enhancement, single scatter albedo and absorption wavelength dependence of black carbon. *Atmospheric Chemistry and Physics*, *10*(9), 4207-4220.

Lack, D. A., & Cappa, C. D. (2010). Impact of brown and clear carbon on light absorption enhancement, single scatter albedo and absorption wavelength dependence of black carbon. *Atmospheric Chemistry and Physics*, *10*(9), 4207-4220.

Laskin, A., Laskin, J., and Nizkorodov, S. A., 2015. Chemistry of atmospheric brown carbon. Chemical Reviews, 115, pp.4335–4382.

Lelieveld, J., Evans, J. S., Fnais, M., Giannadaki, D., and Pozzer, A., 2015. The contribution of outdoor air pollution sources to premature mortality on a global scale. Nature, 525, pp.367–371.

Liu, S., Aiken, A. C., Gorkowski, K., Dubey, M. K., Cappa, C. D., Williams, L. R., ... & Prévôt, A. S. (2015). Enhanced light absorption by mixed source black and brown carbon particles in UK winter. *Nature communications*, *6*(1), 8435.

Massabo, D., Bernardoni, V., Bove, M. C., Brunengo, A., Cuccia, E., Piazzalunga, A., ... & Vecchi, R. (2013). A multi-wavelength optical set-up for the characterization of carbonaceous particulate matter. *Journal of Aerosol Science*, *60*, 34-46.

Massabo, D., Caponi, L., Bernardoni, V., Bove, M. C., Brotto, P., Calzolai, G., ... & Prati, P. (2015). Multi-wavelength optical determination of black and brown carbon in atmospheric aerosols. *Atmospheric Environment*, *108*, 1-12.

Massabò, D., Danelli, S. G., Brotto, P., Comite, A., Costa, C., Di Cesare, A., ... & Prati, P. (2018). ChAMBRe: a new atmospheric simulation chamber for aerosol modelling and bio-aerosol research. *Atmospheric Measurement Techniques*, *11*(10), 5885-5900.

Moosmüller, H., Arnott, W. P., and Walker, J., 2009. Photoacoustic and filter-based ambient aerosol light absorption measurements. Atmospheric Measurement Techniques, 2, pp.417–429.

Moosmüller, H., Chakrabarty, R. K., & Arnott, W. P. (2009). Aerosol light absorption and its measurement: A review. *Journal of Quantitative Spectroscopy and Radiative Transfer*, *110*(11), 844-878.

Moosmüller, H., Chakrabarty, R. K., & Arnott, W. P. (2009). Aerosol light absorption and its measurement: A review. *Journal of Quantitative Spectroscopy and Radiative Transfer*, *110*(11), 844-878.

Müller, T., Nowak, A., Wiedensohler, A., Sheridan, P., Laborde, M., Covert, D. S., ... & de Leeuw, G. (2009). Angular illumination and truncation of three different integrating nephelometers: Implications for empirical, size-based corrections. *Aerosol Science and Technology*, *43*(6), 581-586.

Nel, A., Xia, T., Madler, L., & Li, N. (2006). Toxic potential of materials at the nanolevel. *science*, *311*(5761), 622-627.

Oberdörster, G., Oberdörster, E., & Oberdörster, J. (2005). Nanotoxicology: an emerging discipline evolving from studies of ultrafine particles. *Environmental health perspectives*, *113*(7), 823.

Peterson, M.R., Richards, M.H., 2002. Thermal-optical transmittance analysis for organic and elemental carbon: calibration and application. Aerosol Science and Technology, 36, 325–338.

Petzold, A., & Schönlinner, M. (2004). Multi-angle absorption photometry—a new method for the measurement of aerosol light absorption and atmospheric black carbon. *Journal of Aerosol Science*, *35*(4), 421-441.

Petzold, A., Ogren, J. A., Fiebig, M., Laj, P., Li, S. M., Baltensperger, U., ... & Zhang, X. Y. (2013). Recommendations for reporting" black carbon" measurements. *Atmospheric Chemistry and Physics*, *13*(16), 8365-8379.

Petzold, A., Ogren, J. A., Fiebig, M., Laj, P., Li, S. M., Baltensperger, U., ... & Zhang, X. Y. (2013). Recommendations for reporting" black carbon" measurements. *Atmospheric Chemistry and Physics*, *13*(16), 8365-8379.

Petzold, A., Ogren, J. A., Fiebig, M., Laj, P., Li, S. M., Baltensperger, U., ... & Zhang, X. Y. (2013). Recommendations for reporting" black carbon" measurements. *Atmospheric Chemistry and Physics*, *13*(16), 8365-8379.

Pöschl, U. (2005). Atmospheric aerosols: composition, transformation, climate and health effects. *Angewandte Chemie International Edition*, *44*(46), 7520-7540.

Putaud, J. P., Raes, F., Van Dingenen, R., Brüggemann, E., Facchini, M. C., Decesari, S., ... & Wiedensohler, A. (2004). A European aerosol phenomenology—2: chemical characteristics of particulate matter at kerbside, urban, rural and background sites in Europe. *Atmospheric environment*, *38*(16), 2579-2595.

Putaud, J. P., Van Dingenen, R., Alastuey, A., Bauer, H., Birmili, W., Cyrys, J., ... & Raes, F. (2010). A European aerosol phenomenology–3: Physical and chemical characteristics

of particulate matter from 60 rural, urban, and kerbside sites across Europe. *Atmospheric Environment*, *44*(10), 1308-1320.

Querol, X., Viana, M., Alastuey, A., Amato, F., Moreno, T., Castillo, S., ... & Zabalza, J. (2007). Source origin of trace elements in PM from regional background, urban and industrial sites of Spain. *Atmospheric environment*, *41*(34), 7219-7231.

Sandradewi, J., Prévôt, A. S., Szidat, S., Perron, N., Alfarra, M. R., Lanz, V. A., ... & Baltensperger, U. R. S. (2008). Using aerosol light absorption measurements for the quantitative determination of wood burning and traffic emission contributions to particulate matter. *Environmental science & technology*, *42*(9), 3316-3323.

Schnaiter, M., Horvath, H., Möhler, O., Naumann, K. H., Saathoff, H., & Schöck, O. W. (2003). UV-VIS-NIR spectral optical properties of soot and soot-containing aerosols. *Journal of Aerosol Science*, *34*(10), 1421-1444.Schraufnagel, D. E., Balmes, J. R., De Matteis, S., et al., 2019. Health benefits of air pollution reduction. Annals of the American Thoracic Society, 16, pp.1478–1487.

Seinfeld, J. H., and Pandis, S. N., 2016. Atmospheric Chemistry and Physics: From Air Pollution to Climate Change. 3rd ed. Wiley.

Shrivastava, M., Cappa, C. D., Fan, J., Goldstein, A. H., Guenther, A. B., Jimenez, J. L., ... & Zhang, Q. (2017). Recent advances in understanding secondary organic aerosol: Implications for global climate forcing. *Reviews of Geophysics*, *55*(2), 509-559.

Sorensen, C. M. (2001). Light scattering by fractal aggregates: a review. *Aerosol Science & Technology*, *35*(2), 648-687.

Stipe, C.B., Higgins, B.S., Lucas, D., Koshland, C.P., Sawyer, R.F., 2005. Soot particle production characteristics of inverted diffusion flames. Combustion and Flame, 142, 172–179.

TSI, F. S. U. (2013). TSI's Scanning Mobility Particle SizerTM (SMPSTM) Spectrometer Model 3938. *Application Note SMPS-006*.

TSI, M. 3330 optical particle sizer spectrometer operation and service manual.

Turpin, B. J., Huntzicker, J. J., & Hering, S. V. (1994). Investigation of organic aerosol sampling artifacts in the Los Angeles Basin. *Atmospheric Environment*, *28*(19), 3061-3071.

Vernocchi, V. (2022). Assessment of toxicity of particulate matter in the sub-micrometric range by an Atmospheric Simulation Chamber.

Vernocchi, V., Brunoldi, M., Danelli, S. G., Parodi, F., Prati, P., & Massabò, D. (2022). Characterization of soot produced by the mini inverted soot generator with an atmospheric simulation chamber. *Atmospheric Measurement Techniques*, *15*(7), 2159-2175.

Viana, M., Kuhlbusch, T. A., Querol, X., Alastuey, A., Harrison, R. M., Hopke, P. K., ... & Hitzenberger, R. (2008). Source apportionment of particulate matter in Europe: a review of methods and results. *Journal of aerosol science*, *39*(10), 827-849.

Weingartner, E., Saathoff, H., Schnaiter, M., Streit, N., Bitnar, B., & Baltensperger, U. (2003). Absorption of light by soot particles: determination of the absorption coefficient by means of aethalometers. *Journal of Aerosol Science*, *34*(10), 1445-1463.

Zhang, Q., Jimenez, J. L., Canagaratna, M. R., Allan, J. D., Coe, H., Ulbrich, I., ... & Worsnop, D. R. (2007). Ubiquity and dominance of oxygenated species in organic aerosols in anthropogenically-influenced Northern Hemisphere midlatitudes. *Geophysical research letters*, *34*(13).

Zhang, R., Khalizov, A., Wang, L., Hu, M., & Xu, W. (2012). Nucleation and growth of nanoparticles in the atmosphere. *Chemical reviews*, *112*(3), 1957-2011.